# STRESS AND MICROSTRUCTURAL EVOLUTION DURING SHAPE-PRESERVING SILICA MAGNESIOTHERMIC REDUCTION

**A Dissertation**
**Presented to**
**The Academic Faculty**

**By**

**Stanley Casey Davis, Jr.**

**In Partial Fulfillment**
**Of the Requirements for the Degree**
**Doctor of Philosophy in Materials Science and Engineering**

**Georgia Institute of Technology**

**May, 2013**

**STRESS AND MICROSTRUCTURAL EVOLUTION DURING SHAPE-PRESERVING SILICA MAGNESIOTHERMIC REDUCTION**

Approved by:


Dr. Kenneth H. Sandhage, Advisor
School of Materials Science and Engineering
*Georgia Institute of Technology*

Dr. Hamid Garmestani
School of Materials Science and Engineering
*Georgia Institute of Technology*

Dr. William Brent Carter
School of Materials Science and Engineering
*Georgia Institute of Technology*

Dr. Min Zhou
School of Mechanical Engineering
*Georgia Institute of Technology*

Dr. Meilin Liu
School of Materials Science and Engineering
*Georgia Institute of Technology*


Date Approved: 2-28-2013

To my father, Stanley Casey Davis, Sr.,

And my mother, Alane Davis

## ACKNOWLEDGEMENTS

I would like to express my gratitude to a number of people I have been gifted to work with during my time at Georgia Tech. I would like to thank my advisor, Professor Kenneth Sandhage, whose knowledge and hard work have set an example for our group. I would like to thank Dr. Yunshu Zhang, Dr. Yunnan Fang, Dr. Samuel Shian, and Dr. Vonda Sheppard for their helpful and knowledgeable advice, which I have constantly found valuable. I would also like to thank Dr. Murtaza Askari, Dr. Gousia Begum, Zhixuan Xia, Dr. Min Kyu Song, Dr. Benjamin Hatton, Dr. Joanna Aizenberg, Dr. Ali Adibi, Dr. Meilin Liu, and Dr. Nils Kroeger, collaborators whose practicality and expertise have been invaluable in building this work. In addition, I would like to thank my committee, Dr. Meilin Liu, Dr. Brent Carter, Dr. Hamid Garmestani, and Dr. Min Zhou for their direction and helpful discussions. Finally, I would like to thank the members of the Sandhage group for their help and support.

My deepest thanks go to my family, my mother and father, Stan and Alane, and my sisters, Ashley and Cassidy, for their enduring support and encouragement.

## TABLE OF CONTENTS

## LIST OF TABLES

## LIST OF FIGURES

## LIST OF ABBREVIATIONS

| | |
|---|---|
| XRD | x-ray diffraction |
| SE(M) | scanning electron (microscopy) |
| TE(M) | transmission electron (microscopy) |
| AFM | atomic force microscopy |
| FTIR | Fourier transform infrared analysis |
| hr | hour |
| min | minute |
| s | second |
| DE | silica diatomaceous earth |
| SiDE | silicon diatomaceous earth replicas |
| CDE | carbon diatomaceous earth replicas |
| AgDE | CDE-templated silver-bearing diatomaceous earth replicas |
| AuDE | CDE-templated gold-bearing diatomaceous earth replicas |
| VC | XC-72R Vulcan carbon black |
| AuNP | gold nanoparticles |

## SUMMARY

Shape-preserving silica magnesiothermic reduction is a gas-solid reaction used to convert complex, 3-dimensional $SiO_2$ structures into replicas composed of a two-phase product of MgO and Si. The most widely-cited application of this reaction concerns the formation of porous Si structures by the selective removal of MgO from the product. A number of basic mechanisms of this process are still poorly understood. In this work, basic reaction mechanisms critical to the process of shape preservation that occurs when converting $SiO_2$ to MgO/Si are examined and clarified.

The MgO/Si components of this reaction are found to form an interwoven aggregate product structure. This product structure is sufficiently robust that the MgO component, which accounts for ~65% of the product volume, can be selectively removed from the structure to generate a highly porous skeleton of Si. The aggregate product structure was deduced to result because stacked layers of MgO/Si product phases with planar interfaces are geometrically unstable, owing to the product growth kinetics. The interwoven nature of the aggregate may be explained by the presence of an amorphous magnesium silicate phase ahead of the MgO/Si product during reaction. Complex composition gradients in the magnesium silicate may lead to tortuous and branching growth of MgO and Si phases as the magnesium silicate is consumed by reaction.

A large residual stress (> 5 GPa) was measured in the MgO/Si product layer formed during reaction of planar quartz. Despite the presence of such a large stress, no distortion or cracking of reacted structures was found to occur after reaction in the temperature range 650-900 °C. XRD-based residual stress measurements and

morphological observations of product films on reacted quartz substrates were used to evaluate possible mechanisms of stress relief in the structure. It was found that the migration of MgO to the external surface of the product could be correlated to the rate of stress relaxation that occurred in annealed product films. Of a number of possible mechanisms, stress-induced migration of MgO was the only mechanism that could be confirmed to occur, the rate of which could be linked to the rate of stress relaxation that was found to occur during annealing.

To enhance the hierarchical porosity of magnesiothermically-generated Si replicas of intricately-shaped diatomaceous earth particles, an additional reaction process was employed to convert Si structures into high specific surface area C replicas. These C replicas were studied for use in chemical catalysis, with catalysts such as Pt and a biologically-derived enzyme. In both cases, the C diatom-based samples were shown to have a significant performance advantage over commercially available C controls. In addition, it was shown that, through the use of aqueous electroless displacement reactions, the C diatom structure can be converted into a high surface area Au-bearing replica, which can also be attractive for applications in catalysis.

Finally, porous Si fabrication through gas-solid magnesiothermic reduction was applied to optical and photonic devices. MgO/Si and porous Si replicas were created from silica inverse opal structures produced by a novel co-assembly method. MgO/Si replicas were found to have a high refractive index and are expected to have low absorbance in the IR spectrum. Porous Si replicas were found to well retain the shape of the inverse opal structure, despite the high volume of porosity in the Si walls. In the future, such porous Si replicas may find use in optical chemical sensing. Silica

magnesiothermic reduction was also applied to generate a porous Si cladding on integrated Si microcavity resonators. It was shown that this porous Si cladding was able to significantly enhance the resonance-based response in these devices to the adsorption of an analyte species. Devices enhanced in this way have promise as portable, low cost, compact chemical sensors.

# CHAPTER 1:

# INTRODUCTION

Recent research in regards to shape-preserving gas-silica displacement reactions has resulted in a number of techniques by which to convert intricately-shaped and hierarchically-ordered silica structures into a number of functional materials including titania, zirconia, and barium titanate[1]. Silica offers a wide variety of starting synthetic and biogenic templates, because of the well understood chemistry of silica precursors and its commonness in biomineralized structures. Of especial interest in this work is the conversion of silica templates into porous silicon replicas by magnesiothermic reduction.

Porous silicon has received wide attention for the many desirable properties that it has been found to possess. An explosion of activity occurred in this field after the discovery of photoluminescence in anodically etched porous Si by Canham[2] in the early 1990's. Immediate interest was found worldwide over the potential development of silicon based opto-electronic microdevices. In addition to integrated optoelectronics, porous silicon has found a number of applications due to its high surface area and unique properties, which differ from those of bulk silicon. Canham has reported that porous Si, in contrast to bulk Si, is biocompatible, opening up the potential for porous Si to be important at the interface between the body and implantable microelectronic devices[3]. Porous Si has the potential to become an important support for catalyst microreactors. Llorca, et al. report the use of macroporous silicon microreactors loaded with $Co_3O_4$-ZnO catalyst for steam reforming applications, exploiting silicon's relative stability in the presence of steam up to 1073 °C[4]. Silicon also displays the highest theoretical capacity

as an anodic material in lithium ion cells, making high surface area silicon a major focus in the further development of lithium ion battery technology[5].

Thus far, the most commonly-reported porous Si fabrication method was pioneered by Uhlir[6a] and Turner[6b] in the 1950's. These authors developed the foundation for electrochemically etching the surface of silicon wafers in a hydrofluoric acid solution. However, the need for electrical contact and the harsh etchant environment employed limits the use of this technique. A major alternative to anodic etching is the metal-assisted chemical etching (MACE) process, which does not require electrical contact[7]. In this method, a noble metal (such as Au or Pt) is patterned onto an Si substrate. The noble metal loaded Si is then submerged in a $HF/H_2O_2$ solution, where the noble metal facilitates the reduction of $H_2O_2$ by hole injection into Si. Etch pits in Si underneath the noble metal pattern grow when the reduced Si interacts with HF. In this way, a noble metal pattern can be transformed into a porous Si structure. This technique is, of course, reliant on the ability to pattern noble metal onto a Si substrate. If the Si substrate is of a complicated 3-D geometry, this may not be easily possible.

The gas-solid silica magnesiothermic reduction process (hereon referred to as $Mg(g)/SiO_2$ reduction) offers a route by which to create porous Si structures with intricate geometries derived from the wide array of possible silica templates[8]. Such silica magnesiothermic reduction entails the reaction of silica structures with magnesium vapor, which results in a composite structure of magnesia and silicon by the following reaction:

$$2Mg(g) + SiO_2(s) \rightarrow 2MgO(s) + Si(s) \quad (1.1)$$

This reaction has been shown to successfully produce magnesia-silicon composite replicas of numerous silica templates, including diatom frustules and periodic

mesoporous structures[8,9]. Features as small as 15 nm have been preserved in the final replica by this process[9]. MgO and Si phases are found to be co-continuous ("interwoven") and subsequent etching of the MgO or Si phase can be carried out without damaging the replica. For the production of porous Si, HCl is used to selectively remove MgO. This results in a final porous Si replica, with a significantly higher surface area than the starting template[8,10].

A major advantage of this technique is the leveraging of the high diversity of silica chemistry, which makes it possible to create a wide range of structures possessing complex, three-dimensional geometries. Standard semiconductor processing techniques (e.g., photolithography) can be used to create a variety of integrated silica structures. Organosilicas can now be sculpted into a wide range of structures using light[11a] or self-assembly[11b]. In addition, a number of hierarchically-ordered, three-dimensional silica structures exist in nature (e.g., diatomaceous earth). The shape-preserving magnesiothermic reduction process offers the ability to convert these silica structures into porous silicon, while retaining the complex three-dimensional geometry and fine features of the starting structure. For example, diatom frustules of the species *Aulacoseira* have been converted to porous silicon while maintaining their three-dimensional shape and well-ordered pore structure[8].

Although porous Si generation by silica magnesiothermic reduction has been applied by many authors[4,8,9,12], the development of the MgO-Si system is still poorly understood. A number of authors have made detailed studies of the reaction between Mg and $SiO_2$ in solid-state reaction couples, but the high activity of Mg in these systems results in the formation of $Mg_2Si$ at the expense of Si (i.e., an MgO/$Mg_2Si$ product occurs

instead of MgO/Si)[13]. As a consequence of $Mg_2Si$ formation, the product microstructure is radically different from that seen during the shape-preserving gas-solid reaction that is used to generate porous Si replicas. As opposed to an interwoven composite of MgO/Si, periodic layers of $Mg_2Si$/MgO are found to occur. In this dissertation, the gas-solid reaction between Mg and $SiO_2$ has been studied in greater detail. The goal is to gain a better understanding of the kinetics and microstructural evolution that facilitates an interwoven, shape-preserving MgO/Si product structure during Mg(g)/$SiO_2$ reduction. In addition, new applications of such silica magnesiothermic reduction are explored in the areas of catalysis and chemical sensing.

# CHAPTER 2:

# MICROSTRUCTURAL EVOLUTION AND KINETICS ANALYSIS OF SHAPE-PRESERVING SILICA MAGNESIOTHERMIC REDUCTION

## 2.1 Introduction

As previously discussed, the Mg(g)/$SiO_2$ reduction reaction is becoming a widely-studied process for the fabrication of porous Si replicas of complex $SiO_2$ templates. Even so, the kinetics and processes of morphological evolution that occur during this reaction are poorly understood. While a wide range of data exists on the reaction between MgO and $SiO_2$[14], comparatively little exists for the reaction between Mg and $SiO_2$. Early work on silica magnesiothermic reduction by Wynnyckyj and Rao[15] provides a detailed study of the kinetics and morphological evolution of silica powder compacts during the reaction between Mg gas and $SiO_2$, but only at a high temperature (1150 °C) where there exists a significant formation of SiO gas during the reaction, and, consequently, the silica starting material undergoes a radical geometric transformation (i.e., the reaction process was not shape preserving).

More recently, work has been conducted on solid-state reaction couples of Mg and $SiO_2$[16]. Unfortunately, during the reaction between solid Mg and $SiO_2$, the prevailing reaction is:

$$4Mg + SiO_2 \rightarrow Mg_2Si + 2MgO \quad (2.1)$$

and, consequently, the morphology of the reacted zone is radically different than what one would expect for a product of MgO and Si. The primary morphologies of the reacted

zone found in those works were periodic layers of $Mg_2Si$ and MgO oriented parallel to the reaction front. This type of reaction morphology is commonly seen in solid state displacement reactions of the general form:

$$(\delta+\delta')A + BC \rightarrow A_\delta C + A_{\delta'}B \quad (2.2)$$

and is the result of the buildup of diffusing species at the interface between $A_\delta C$ and $A_{\delta'}B$ layers[16]. In this work, the final product of shape preserving $Mg(g)/SiO_2$ reduction takes on an aggregate product morphology of MgO and Si phases. $Mg_2Si$ formation is avoided as a result of either strict control of reaction time or through control of the magnesium vapor partial pressure ($p_{Mg}$) present during reaction.

When the solid-state displacement reaction takes the general form:

$$xA + B_yC \rightarrow A_xC + yB \quad (2.3)$$

three product morphologies have been identified by Rapp, et al.[17]. The first is composed of dual layers of $A_xC$ and B forming parallel to the reaction front, with the $A_xC$ product forming adjacent to reactant A, and the B product forming adjacent to reactant $B_yC$ (Figure 2.1). Dual layers are the product of a geometrically-stable planar interface between the product phases $A_xC$ and B. Rapp, et al. identified the condition for the geometric stability of a planar interface as occurring when the flux of the rate-limiting species occurs in the same direction as the velocity of the reaction fronts[17]. Therefore, this morphology is favored, for example, when the flux of A across $A_xC$ is smaller than the flux of C across B (assuming the reaction front moves from A toward $B_yC$).

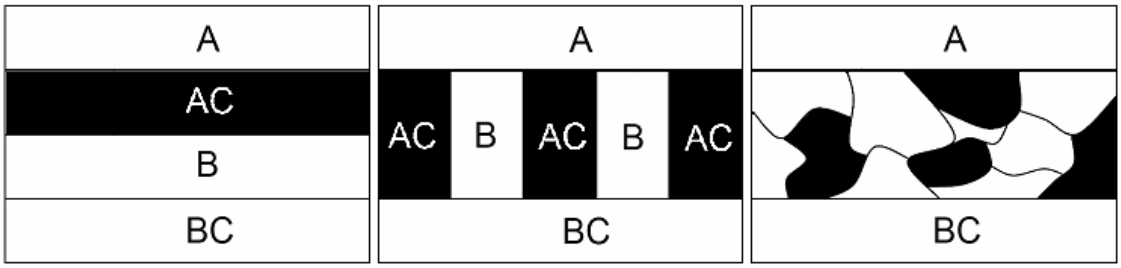


Figure 2.1: Product morphologies of solid-state displacement reactions: *(Left)* Dual layer morphology, *(Middle)* lamellar aggregate morphology, *(Right)* interwoven aggregate morphology.

If, on the other hand, the flux of C across B is rate limiting, then the planar interface between the $A_xC$ and B products will be unstable and an aggregate morphology will result. Rapp, et al. identified two aggregate morphologies which may form. The first is a lamellar aggregate morphology, in which lamella of AC and B products form roughly perpendicular to the reaction front. Yurek, et al. later claimed based off of experimental observations that the lamellar aggregate morphology will form when there exists no appreciable range of mutual solid solubility between $A_xC$ and $B_yC$, as well as between A and B[18]. The second aggregate morphology is an interwoven morphology, in which the two product phases form as a co-continuous composite. In the same study, Yurek, et al. claimed based on experimental observations that this type of morphology occurred in systems in which $A_xC$ and $B_yC$, as well as A and B, possess broad ranges of mutual solid solubility. The Mg(g)/$SiO_2$ reduction reaction in which the products are MgO and Si has been experimentally observed to result in an interwoven aggregate product morphology (Figure 2.2). However, this result is in conflict with the criterion of Yurek, et al., since the only phases present in the MgO-$SiO_2$ system are the line compounds $Mg_2SiO_4$ and $MgSiO_3$, and the only multicomponent phase present in the

Mg-Si system is the line compound $Mg_2Si$[19]. As there exists no appreciable range of mutual solid solubility in these systems, it is expected (based on the long-standing hypothesis of Yurek, et al.) that the resultant product morphology would be a lamellar aggregate morphology, which is at odds with experimental observations from Mg(g)/$SiO_2$ reduction. The interwoven morphology of the MgO/Si product is a critical feature of this reaction, as it enables the selective removal of the MgO phase (which is expected to constitute ~65% of the product volume) to produce a highly-porous, mechanically-stable skeleton of Si. A lamellar or layered morphology would likely lead to structural disintegration upon MgO removal.

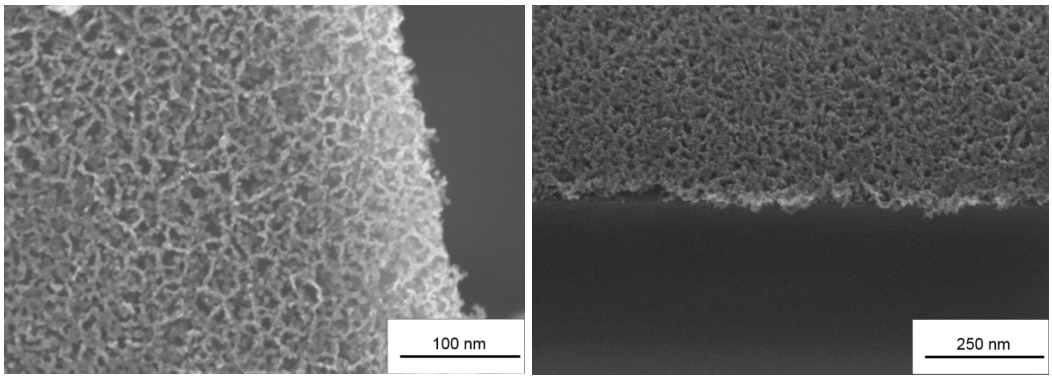


Figure 2.2: SEM images of cleaved porous Si films after selective removal of MgO following Mg(g)/$SiO_2$ reduction of $SiO_2$ films conducted at 750 ˚C.

The goal of the following work is to more closely study the kinetics and mechanisms of Mg(g)/$SiO_2$ reduction in its shape-preserving form. This means that it has been studied in the temperature range of 650-900 °C, and an $Mg_2Si$ gas source has been used to supply the Mg gas reactant. As will be discussed, the $p_{Mg}$ over $Mg_2Si$ is not sufficient to strongly favor the formation of an $Mg_2Si$ product, and, thus, only the target

MgO and Si product phases will form. Instead of complex-shaped $SiO_2$ templates, planar quartz wafers have been reacted with Mg gas, so that precise, detailed observations from reacted cross-sections can be readily obtained of the kinetics and morphology of the product films. The ultimate goal is to obtain a better understanding of the chemical and physical processes of shape-preserving Mg(g)/$SiO_2$ reduction.

The following discussion is divided into three sections. In the first section, existing theory will be applied to the Mg(g)-$SiO_2$ system to predict the kinetics and morphology of the reaction of Mg vapor with quartz $SiO_2$ wafers. The second section will describe the experimental methods used here to study this reaction. The third section will describe the results of these experiments and provide reconciliation of these results with theory.

## 2.2 Theory

### 2.2.1 Fundamentals of Gas-Solid Silica Magnesiothermic Reduction Chemistry

The net reaction between $SiO_2$ and Mg can be characterized with the following four progressive independent reactions:

$$2Mg(g) + 3SiO_2 \rightarrow 2MgSiO_3 + Si \quad (2.4)$$

$$2Mg(g) + 4MgSiO_3 \rightarrow 3Mg_2SiO_4 + Si \quad (2.5)$$

$$2Mg(g) + Mg_2SiO_4 \rightarrow 4MgO + Si \quad (2.6)$$

$$2Mg(g) + Si \rightarrow Mg_2Si \quad (2.7)$$

Reactions (2.4) and (2.5) can be considered as the partial reduction of $SiO_2$ by Mg, the result of which is the formation of a magnesium silicate and reduced Si. Magnesium metasilicate ($MgSiO_3$) and magnesium orthosilicate ($Mg_2SiO_4$) are line compounds in the

$MgO\text{-}SiO_2$ system[19]. As these are the only compounds that form at equilibrium between MgO and $SiO_2$ at ambient pressure, there is no product with an appreciable range of solid solubility between Mg-Si-O at equilibrium[19]. Reaction (2.6) represents the last reaction in the complete reduction of $SiO_2$ by Mg. Reaction (2.7) represents the reaction between excess Mg reactant and the Si product of reactions (2.4), (2.5), and (2.6), which yields magnesium silicide, $Mg_2Si$. Because the reaction between $Mg_2Si$ and $SiO_2$, described by:

$$Mg_2Si + SiO_2 \rightarrow 2MgO + 3Si \qquad (2.8)$$

is highly favored ($\Delta G°$=-188.890 and - 181.903 kJ $mol^{-1}$ at 650 ˚C and 900 ˚C respectively[20]), then reaction (2.7) should not proceed (from a thermodynamic perspective) until all $SiO_2$ has been consumed. If the goal is to generate porous Si, then reaction (2.7) can be considered to be an overreaction of the template material.

If all solid species involved in the above reactions are considered to be in a pure, stoichiometric state, and using pure, Raoultian reference frames, and assuming ideal gas behavior in the absence of an equation of state for magnesium gas, the reaction quotient can then be approximated as a function of the $p_{Mg}$ in the system. Typically, two Mg gas sources have been used in previous work: Mg metal which has a high equilibrium $p_{Mg}$ and relatively fast reaction kinetics, and $Mg_2Si$ which has a significantly lower $p_{Mg}$ and relatively slow reaction kinetics. Using tabulated $\Delta G_f°$ values[20], $\Delta G$ values for each reaction are calculated for $p_{Mg}$ in equilibrium with Mg metal and $Mg_2Si$, assuming ideal gas behavior of Mg gas, in the following table:

Table 2.1: ΔG values at the magnesium partial pressures in equilibrium with Mg and $Mg_2Si$[20].

| Rxn | Magnesium | | Magnesium Silicide | |
|---|---|---|---|---|
| | 650 ºC | 900 ºC | 650 ºC | 900 ºC |
| (2.4) | -337.6 kJ $mol^{-1}$ | -324.8 kJ $mol^{-1}$ | -266.5 kJ $mol^{-1}$ | -261.3 kJ $mol^{-1}$ |
| (2.5) | -293.5 | -273.1 | -222.5 | -209.6 |
| (2.6) | -197.0 | -183.3 | -125.9 | -119.7 |
| (2.7) | -71.0 | -63.5 | 0 | 0 |

Here it can be seen that reaction (2.7) is not strongly favorable, if $Mg_2Si$ is used as an Mg gas source. For the case of a pure Mg metal gas source, $Mg_2Si$ formation is still favorable. However, as discussed above, the formation of $Mg_2Si$ is not found to occur until $SiO_2$ is completely consumed. Therefore, if the process is terminated sufficiently early, then $Mg_2Si$ formation can be avoided and the Si product can be preserved. Despite the possible formation of $Mg_2Si$ at the expense of Si during the reaction, the higher equilibrium $p_{Mg}$ of Mg metal provides for faster reaction kinetics, especially at lower temperatures (< 850 °C), making this Mg gas source desirable at low reaction temperatures.

The evolution of SiO gas during magnesiothermic reduction is also a possibility. In their original work on silica magnesiothermic reduction at temperatures > 1000 °C, Wynnyckj and Rao found evidence of SiO gas formation from the product structures[15]. SiO can form during silica magnesiothermic reduction according to the following reaction:

$$Mg(g) + SiO_2 \rightarrow MgO + SiO(g) \quad (2.9)$$

The equilibrium $p_{SiO}$ for this reaction is calculated in Table 2.2 for values of $p_{Mg}$ in equilibrium with Mg metal and $Mg_2Si$ at select reaction temperatures. It is seen that equilibrium SiO gas formation sharply increases with temperature. As detailed in the original work by Wynnyckj and Rao, SiO becomes a significant component of high temperature magnesiothermic reduction, such that the process is no longer shape preserving[15]. While equilibrium $p_{SiO}$ as a result of reaction (2.9) is calculated to become significant at 900 °C with an Mg metal gas source, experimentally no evidence of SiO solid phases have been found in the products produced under these conditions, which suggests that SiO gas formation must be kinetically unfavorable.

Table 2.2: Equilibrium $p_{SiO}$ values for reaction (2.8) at select temperatures and Mg gas sources.

| Temperature | $\Delta G^{\circ}_{rxn}$ (kJ $mol^{-1}$)[20] | $p_{SiO}$ (bar) | |
|---|---|---|---|
| | | Mg Source | $Mg_2Si$ Source |
| 650 ºC | 18.894 | $3.61x10^{-4}$ | $3.52x10^{-6}$ |
| 900 ºC | 8.163 | 0.121 | $2.70x10^{-3}$ |
| 1150 ºC | -2.088 | 1.95 | 0.161 |

### 2.2.2 Morphology Prediction of Silica Magnesiothermic Reduction

Rapp, et al. were the first to develop a predictive model for determining the product zone morphology of a solid-state displacement reaction from a reaction couple with a planar interface of the general form of reaction (2.3). This approach may be

applied to reaction (1.1). In the work of Rapp, et al.[17], three product morphologies were described (Figure 2.1): the dual layer morphology, the lamellar aggregate morphology, and the interwoven aggregate morphology. The model developed by Rapp can be used to determine if a reaction couple will form a dual layer morphology or an aggregate morphology. Later, Yurek, et al. provided criterion for discerning whether an interwoven aggregate or a lamellar aggregate will form, if the dual layer morphology is unstable[18]. The criterion developed by Yurek was initially based upon broad experimental observations, but Tangchitvittaya, et al. later provided a theoretical basis in support[21]. The criterion provided by Yurek, et al. states that for an interwoven aggregate product to form there must exist an appreciable range of mutual solid solubility between the reactant and product species. Otherwise, if reactant and product species are not soluble with one another, a lamellar aggregate product should develop.

The method as described by Rapp, et al. is a quantitative model in which the geometric stability of a planar interface between reaction products is used to predict whether the products will form a dual layer or aggregate morphology[17]. As illustrated in Figure 2.3 for the case of reaction (1.1), a dual layer configuration of products is initially considered. This method then determines if the initially roughly planar interface between these products is stable with respect to perturbations (illustrated by the wavy unevenness in Case I and II in Figure 2.3). The rule employed by Rapp, et al. states that if the flux of the rate-limiting species goes against the velocity of the reaction front, then the planar interface between products will not be stable with respect to perturbations. For the present case, the velocity of the MgO/Si product interface is assumed to move toward the $SiO_2$ reactant (as MgO grows at the MgO/Si interface and Si grows at the $Si/SiO_2$

interface). As demonstrated in Figure 2.3, for the case of $Mg^{2+}$ diffusion across the MgO product layer as the rate-limiting step for growth (Case I), the flux of $Mg^{2+}$ at point A on the interface is greater than at point B on the uneven interface. The MgO growth rate at point A will then be greater than at point B, and the interface will flatten. If, on the other hand the diffusion of O across the Si product is assumed to be rate-limiting (Case II), then the flux of O will be greater at point B then at point A on the uneven interface. Under this condition, the MgO growth rate at point B will be greater and the perturbation will permanently shift the system away from a planar interface. If Case II describes the system, then this model only predicts that an aggregate product morphology will form. This model cannot distinguish whether a lamellar or interwoven aggregate will be produced.

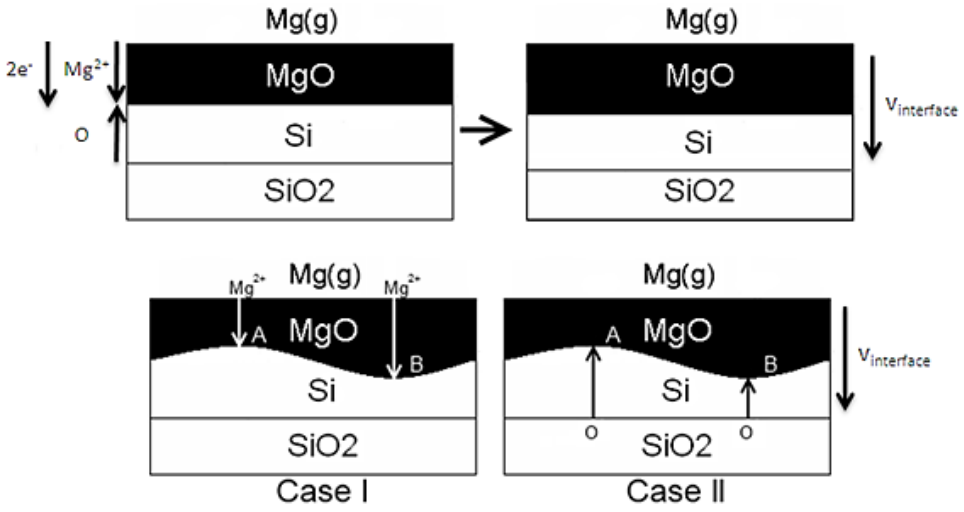


Figure 2.3: (Top) The initial condition in which a planar interface is assumed between MgO and Si products and MgO growth occurs at the MgO/Si product interface, which must then move toward the $SiO_2$ reactant, (Bottom) Case I in which $Mg^{2+}$ diffusion is rate-limiting and a perturbation in the interface geometry is unstable, and Case II in which O diffusion is rate-limiting and a perturbation in the interface geometry is consequently stable.

As diffusion across thickening, compact product layers is assumed to be rate-limiting, the rate of reaction should naturally follow a parabolic rate law:

$$\frac{d\Delta\xi}{dt} = \frac{k_p}{\Delta\xi} \tag{2.10}$$

where $\Delta\xi$ is the product layer thickness, $d(\Delta\xi)/dt$ is the rate of thickening of the product layer, and $k_p$ is a parabolic rate law constant. To determine whether $Mg^{2+}$ diffusion across MgO or O diffusion across Si is rate-limiting, the rational rate law constants $k_r(MgO)$ (the $k_r$ calculated assuming that $Mg^{2+}$ diffusion across MgO controls $\Delta\xi$ of the product layer) and $k_r(Si)$ (the $k_r$ calculated assuming that O diffusion across Si controls $\Delta\xi$ of the product layer) need to be compared.

Calculation of $k_r(MgO)$ can be made with knowledge of diffusion coefficients and assuming local equilibrium at the interfaces of the product and reactant layers following the method developed by Wagner [22]. The value of $k_r(MgO)$ will be dependent upon the predominant electric charge carrier in the MgO product scale. Sempolinski and Kingery found that MgO was a mixed conductor[23a]. For the current work, two values of $k_r(MgO)$ are calculated, the first assuming MgO is a predominant electronic conductor and the second assuming MgO is a predominant ionic conductor. Assuming MgO is a predominant electronic conductor, $k_r(MgO)$ can be calculated from:

$$k_r(MgO) = \frac{150RT}{F^2}\int_{p''_{O_2}}^{p'_{O_2}} t_{ionic}\sigma \mid Z_i \mid^{-1} d\ln p_{O_2} \tag{2.11}$$

where R is the ideal gas constant, T is temperature, F is Faraday's constant, $p'_{O_2}$ and $p''_{O_2}$ are the equilibrium oxygen activities at the $Si/SiO_2$ interface and the Mg(g)/MgO interface respectively, $t_{ionic}$ is the ionic transference number (the fraction of oxidation

current resulting from ion diffusion), $Z_i$ is the equivalent charge on the ion, and σ is the ionic conductivity[22]. From the Einstein-Nernst equation[22]:

$$t_{ionic}\sigma = \left(\frac{F^2}{300RT}\right)|Z_i|D_i ç_i \tag{2.12}$$

where $Z_i$ is the charge of a given species, $D_i$ is the diffusion coefficient, and $ç_i$ is the equivalent concentration. From (2.11) and (2.12), it is seen that:

$$k_r(MgO) = \frac{1}{2}\int_{p''_{O_2}}^{p'_{O_2}} D_i ç_i d \ln p_{O_2} \tag{2.13}$$

$D_{Mg}$ was considered to be independent of $p_{O2}$ by Sempolinski and Kingery[23]. For the case of $Mg^{2+}$ diffusion across MgO, $Z_{Mg}$=2 and $ç_{Mg}$=0.1776 equivalents $cm^{-3}$ [23a]. $D_{Mg}$ is highly dependent upon impurities[23a]. It may be assumed that there is likely a relatively high dopant concentration of $Si^{4+}$ accrued during Mg(g)/$SiO_2$ reduction. The $Mg^{2+}$ vacancy concentration in $Si^{4+}$-doped MgO can then be expressed as:

$$[V_{Mg}'']=[Si_{Mg}^{\cdot\cdot}] \tag{2.14}$$

For the self-diffusion of $Mg^{2+}$ via vacancies through MgO, $D_{Mg}$ can be express as a function of $D_{VMg}$:

$$D_{Mg} = [V''_{Mg}]D_{VMg} \tag{2.15}$$

By combining equations (2.13), (2.14), and (2.15):

$$k_r(MgO) = ç_{Mg}[Si^{\bullet\bullet\bullet\bullet}]D_{V_{Mg}}(\ln p'_{O_2} - \ln p''_{O_2}) \tag{2.16}$$

Sempolinski and Kingery found that $D_{VMg}$ varied with temperature according to the equation[23a]:

$$D_{V''_{Mg}} = (0.38)\exp\left[\frac{-220kJ/mol}{RT}\right]cm^2 s^{-1} \quad (2.17)$$

In Table 2.3, $k_r$(MgO) values are calculated in for 650 °C and 900 °C, for a series of $Si^{4+}$ dopant concentrations.

Table 2.3: $k_r$(MgO) as a function of temperature and Si dopant concentration for the case of predominant electronic conductivity in MgO.

| | | | $k_r$(MgO) as a Function of Si Dopant Concentration (equivalents $cm^{-1}$ $s^{-1}$) | | |
|---|---|---|---|---|---|
| T (°C) | $p''_{O2}$ (bar)$^{20}$ | $p'_{O2}$ (bar)$^{20}$ | 100 ppm | 1 ppm | 1 ppb |
| 650 | $2.40\text{x}10^{-61}$ | $8.23\text{x}10^{-43}$ | $5.12\text{x}10^{-17}$ | $5.12\text{x}10^{-19}$ | $5.12\text{x}10^{-22}$ |
| 900 | $7.41\text{x}10^{-46}$ | $6.63\text{x}10^{-32}$ | $1.73\text{x}10^{-14}$ | $1.73\text{x}10^{-16}$ | $1.73\text{x}10^{-19}$ |

If it is assumed, on the other hand, that MgO is a predominant ionic conductor, then $k_r$(MgO) can be calculated from the equation[22]:

$$k_r(MgO) = \frac{kT}{8e^2}\int_{p''_{O_2}}^{p'_{O_2}} n\mu_n \sigma d\ln p_{O_2} \quad (2.18)$$

where k is Boltzmann's constant, e is the magnitude of the charge on an electron, n is the concentration of free electrons, $\mu_n$ is the electron mobility, and σ is the electronic conductivity. Free electron holes in MgO are generated according to the equation:

$$0.5O_2(g) \rightarrow [V_{Mg}''] + O_O + 2h^{\bullet} \quad (2.19)$$

The equilibrium constant of this equation is:

$$K_{ox} = [V_{Mg}'']\,p^2\,p_{O_2}^{-1/2} \quad (2.20a)$$

Electron-hole equilibrium is given by:

$$\text{null} \rightarrow e' + h^{\bullet} \quad (2.21)$$

for which the equilibrium constant is given by:

$$K_{el} = pn \tag{2.22a}$$

where p is the concentration of free electron holes. From equations (2.14), (2.20a) and (2.22a), it can be seen that the free electron concentration is then given by:

$$n = K_{el} p_{O_2}^{-1/4} \left( \frac{[\mathrm{Si}_{\mathrm{Mg}}^{\bullet\bullet}]}{K_{ox}} \right)^{1/2} \tag{2.23}$$

From equation (2.23), equation (2.18) becomes:

$$k_r(MgO) = \frac{kT}{4F} \mu_n K_{el} \left( \frac{[\mathrm{Si}_{\mathrm{Mg}}^{\bullet\bullet}]}{K_{ox}} \right)^{1/2} \int_{p''_{O_2}}^{p'_{O_2}} p_{O_2}^{-1/4} d \ln p_{O_2} \tag{2.24}$$

Sempolinski, Kingery, and Tutler determined values of $\mu_n$, $K_{el}$, and $K_{ox}$, which are used presently[23b]. These authors determined these values to be:

$$K_{el} = (2.2 \times 10^{33}) T^3 \exp\left( \frac{-670 kJ / mol}{RT} \right) \tag{2.22b}$$

$$K_{ox} = (7.2 \times 10^{63}) \exp\left( \frac{-610 kJ / mol}{RT} \right) \tag{2.22c}$$

From equation (2.24), $k_r$(MgO) values are calculated for a range of $Si^{4+}$ dopant concentrations in Table 2.4, using a value of $\mu_n$ found by Sempolinski, Kingery, and Tuller at 1400 °C as an approximation (21 $cm^2\ V^{-1}\ s$)[23b].

For the case of O diffusion through Si, $k_r$(Si) can be calculated using the equation[17]:

$$k_r(Si) = D_O^{Si} k_S (p'_{O_2} - p''_{O_2}) \tag{2.25}$$

where $k_S$ is the Sievert's law constant for O in Si. Calculations of $k_r$(Si) are reported in Table 2.5.

Table 2.4: $k_r$(MgO) as a function of temperature and Si dopant concentration for the case of predominant ionic conductivity in MgO. Based on values of $K_{el}$, $K_{ox}$, and $\mu_n$ from Sempolinski, Kingery, and Tuller[23b].

| | | | $k_r$(MgO) as a Function of Si Dopant Concentration (equivalents $cm^{-1}$ $s^{-1}$) | | |
|---|---|---|---|---|---|
| T (°C) | $p''_{O2}$ (bar)[20] | $p'_{O2}$ (bar)[20] | 100 ppm | 1 ppm | 1 ppb |
| 650 | $2.40x10^{-61}$ | $8.23x10^{-43}$ | $1.11x10^{-2}$ | $1.11x10^{-3}$ | $3.52x10^{-5}$ |
| 900 | $7.41x10^{-46}$ | $6.63x10^{-32}$ | $9.84x10^{-2}$ | $9.84x10^{-3}$ | $3.11x10^{-4}$ |

Table 2.5: $k_r$(Si) as a function of temperature.

| T (°C) | $D^{Si}_O$ ($cm^2$ $s^{-1}$)[25a] | $k_S$ (mole $cm^{-3}$ $bar^{-1/2}$)[25b] | $k_r$(Si) (equivalents $cm^{-1}$ $s^{-1}$) |
|---|---|---|---|
| 650 | $1.993x10^{-15}$ | $7.496x10^{-10}$ | $1.36x10^{-45}$ |
| 900 | $1.753x10^{-12}$ | $4.403x10^{-8}$ | $1.99x10^{-35}$ |

From the above analysis, it is seen that $k_r$(Si) << $k_r$(MgO) for even small $Si^{4+}$ dopant concentrations, indicating that a planar MgO/Si product interface is not stable, and, therefore, an aggregate product morphology is expected to form.

However, the question posed earlier regarding the formation of an interwoven aggregate over a lamellar aggregate product morphology still remains. Within the Mg-Si-O system, only line compounds are found at equilibrium[19], which by the criteria of Yurek, et al. means that a lamellar aggregate product morphology should form during Mg(g)/$SiO_2$ reduction[18]. To explore this question further requires a better understanding of Mg(g)/$SiO_2$ reduction. Such an understanding will require a detailed study of the reaction mechanisms and kinetics involved in Mg(g)/$SiO_2$ reduction. Through the

following experimental work on these fundamental aspects of Mg(g)/$SiO_2$ reduction, an explanation for the anomalous formation of an interwoven aggregate during shape-preserving Mg(g)/$SiO_2$ reduction will be developed.

## 2.3 Experimental Design

### 2.3.1 Gas-Solid Silica Magnesiothermic Reduction Method

A standard method was developed to generate uniform product films of magnesiothermically-reduced silica. Z-cut single crystal quartz wafers (large area faces displaying the (0001) crystal plane) were chosen as a silica substrate based on the thermal expansion properties of this material. For a hexagonal crystal, CTE can be characterized based on 2 principal directions, the direction parallel to the principal symmetry axis (z) and the directions perpendicular to the principal symmetry axis. Z-cut quartz was chosen because the intrinsic stress in a product film as a result of thermal expansion mismatch would be equal in all directions parallel to the surface of the product film. In addition, the in-plane CTE of z-cut quartz (13.71 ppm $K^{-1}$, averaged from 298K to 1023K)[26a] is very closely matched to that which is expected in the MgO/Si product (10.2 ppm $K^{-1}$ from a rule of mixtures approximation)[26b,c]. Square wafers 10x10x0.5 mm in dimension with 1 side EPI polished to an $R_a$ roughness of < 10 Å were utilized (MTI Corporation, Richmond, CA).

For a magnesium gas source, $Mg_2Si$ powder (99.5% metals basis, Alfa Aesar, Ward Hill, MA) was selected. In this study, it is desirable to completely avoid the formation of final magnesiothermic reduction products other than MgO/Si, as this is the product mixture desirable for porous Si applications. As previously discussed, under

sufficiently high $p_{Mg}$, the MgO/Si product can further react with Mg gas to form an $MgO/Mg_2Si$ product. However, the $p_{Mg}$ in equilibrium with $Mg_2Si$ is such that formation of $Mg_2Si$ is not strongly favored (Table 2.1).

The experimental setup for this method is depicted in Figure 2.4. Initially, $Mg_2Si$ powder was crushed in a mortar and pestle to form a fine powder that could be spread to form a uniform powder bed. The crushed $Mg_2Si$ powder was then added to a 1 $in.^2$ low carbon steel boat. Two layers of pristine $Y_2O_3$-stabilized $ZrO_2$ (YSZ) cloth (Zicar Zirconia, Florida, NY) was placed upon the $Mg_2Si$ powder bed to form a porous separation layer with the quartz sample. This cloth prevented $Mg_2Si$ powder from diffusion bonding to the surface of the quartz samples. A quartz wafer sample was then placed, polished face down, upon the YSZ cloth partition. The loaded boats were then sealed in air in 6 in. long low carbon steel vessels (0.6 max wt.% Mn, 0.04 max wt.% P, 0.05 max wt.% S). To allow for reaction, the sample-loaded ampoules were thrust into a horizontal tube furnace, which had been preheated to the reaction temperature. Reactions were carried out at 700 and 750 °C, which is important to note occurs in the stability range of high-quartz (574-806 °C). The temperature profile of the furnace is provided in Appendix A. At the end of reaction, the sample-loaded ampoules were then removed from the hot furnace and allowed to cool down in air.

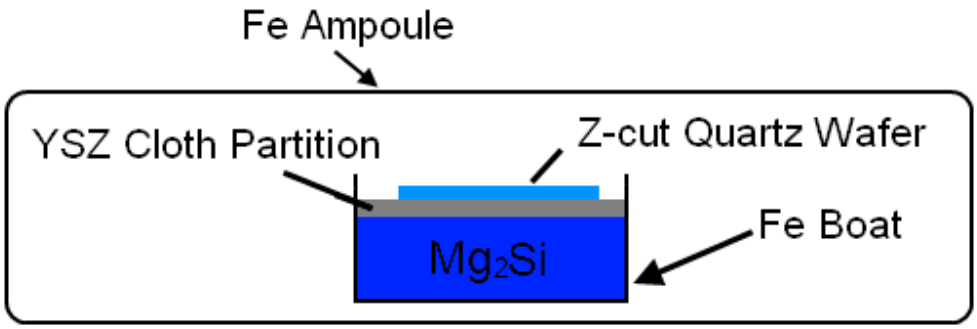


Figure 2.4: Schematic of reaction setup for generating magnesiothermically-reduced product films on monocrystalline quartz wafers.

For cross-sectional SEM analyses of product films on reacted quartz, samples were scribed along the unpolished (back) face of the reacted quartz samples and the samples were then fractured to yield two pieces with relatively smooth cross-sections. Fractured samples were then etched in 250 mM HCl for 30 s to better reveal interfaces between different layers in the product films. During etching, the HCl bath was stirred at 100 rpm. After HCl etching, the samples were washed with dI $H_2O$ and IPA.

For inert marker experiments, 20 nm thick Ag films were sputtered onto the polished surface of the unreacted quartz wafers using a Denton Explorer E-beam Evaporator (Denton Vacuum, Moorestown, NJ, sputtering conducted by Zhixuan Xia). Before reaction, the Ag-coated quartz wafers were annealed in air at 400 °C for 24 hrs.

### 2.3.2 Sample Characterization

SEM analyses were obtained with a LEO 1530 SEM (Carl Zeiss AG, Oberkochen, Germany) at a 15 kV accelerating voltage. For cross-sectional thickness measurements, 4 fracture-sectioned samples at each analyzed reaction time and

temperature were examined, and 10 images of each sample were taken. Twenty thickness measurements were taken per image. TEM analysis was obtained using a JEOL 4000EX (JEOL, Tokyo, Japan). To prepare samples for TEM characterization (performed by Dr. Ye Cai), two samples were glued together with epoxy so that the product films faced each other. The stack was then cured for two minutes. Afterwards, the stack was cut (diamond scribe) into 1.6 mm slices, which were then embedded in a Cu tube (3 mm OD, 2.2 mm ID) with epoxy. After curing, the tube was cut into 1 mm dia. disks. Each disk was then ground to a thickness of 100 µm, which was followed by dimpling and ion milling to perforation. AFM analysis was conducted with a Veeco Dimension 3000 system (Veeco, Plainview, NY) and a 10 nm Si probe (Mikromasch, Wetzlar, Germany).

## 2.4 Results and Discussion

### 2.4.1 Analysis of Gas-Solid Silica Magnesiothermic Reduction Products on Reacted Quartz

TEM/SAED analysis was performed on cross-sections of the magnesiothermically-reduced quartz to elucidate the structure of the product films (provided by Dr. Ye Cai). The results for a sample reacted at 700 °C for 1 hr are shown in Figure 2.5. Two product layers in the product film were found. In the most advanced layer of the product film adjacent to the quartz substrate, nanocrystalline Si was found embedded in an amorphous matrix. Through EDS analysis using a spot size of 10 nm (Figure 2.6), the composition of the amorphous matrix is similar to enstatite, $MgSiO_3$. The second layer, located adjacent to the external surface, was found to be composed of

nanocrystalline MgO and Si phases. No $Mg_2Si$-bearing layer was found in the product film, and the initially polished surface of the sample maintained minimal roughness. The quartz substrate maintained monocrystalline character near the interface with the innermost product layer.

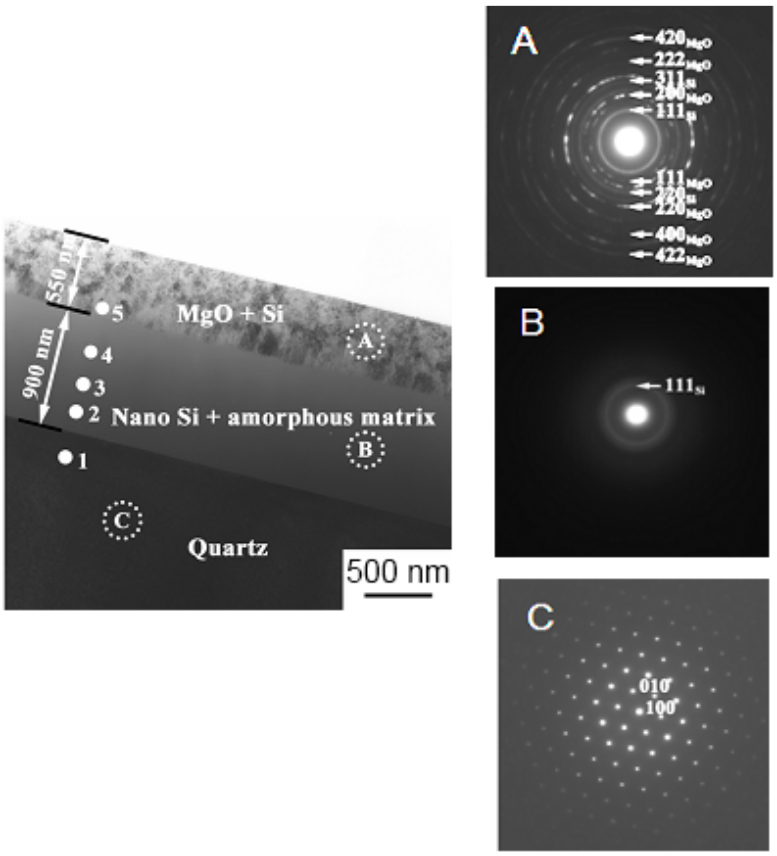


Figure 2.5: TEM/SAED cross-sectional analysis of product film formed on a Mg(g)/$SiO_2$ reduced quartz single crystal at 700 ˚C for 1 hour. (A) SAED pattern of nanocrystalline MgO/Si product layer, (B) SAED pattern of nanocrystalline Si in an amorphous matrix of the internal product layer, and (C) SAED pattern of the single crystal quartz substrate. (Provided by Dr. Ye Cai)

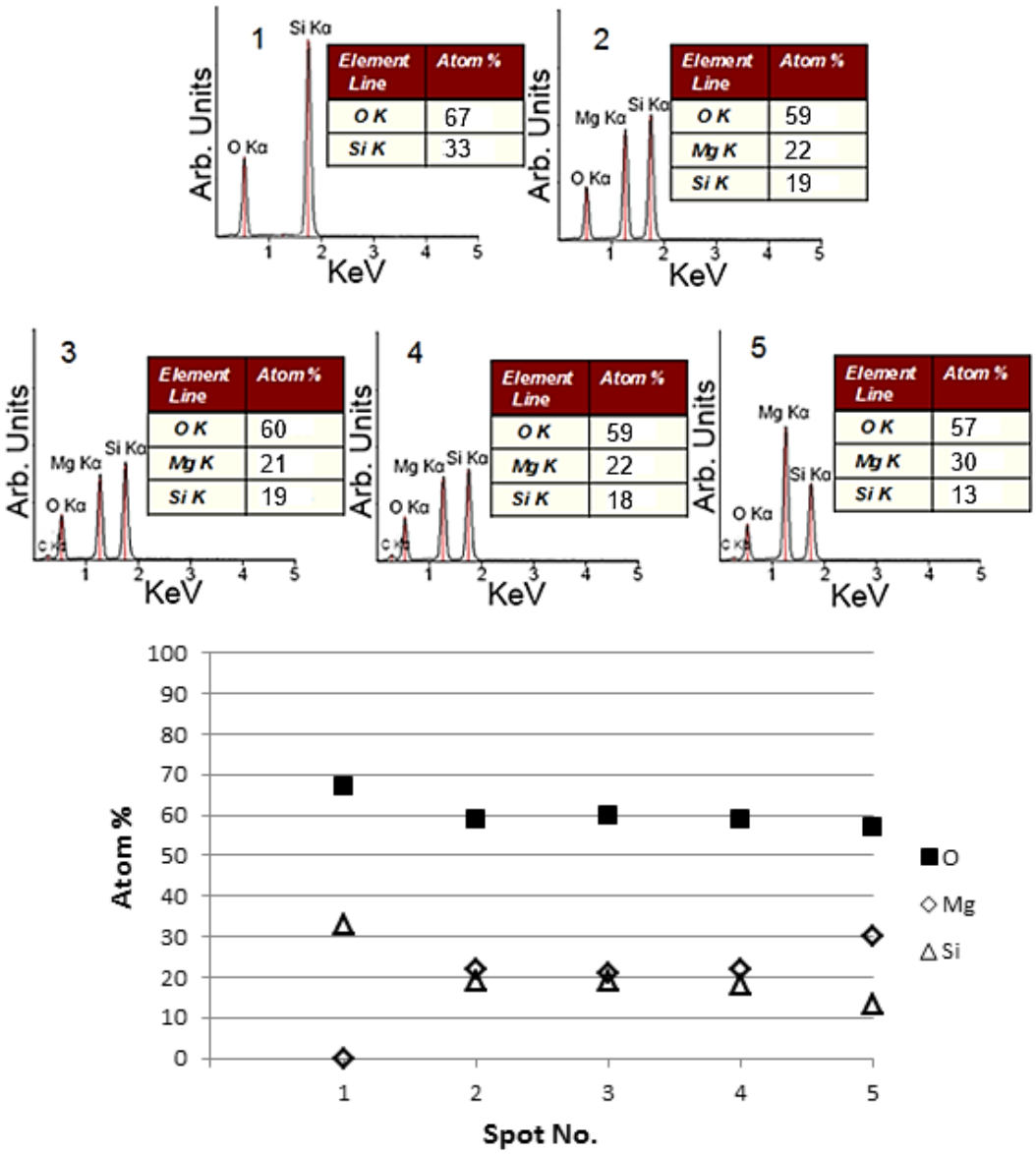


Figure 2.6: EDS analyses of the product film from Figure 2.5. Labels correspond to spots on Figure 2.5. EDS spot size was 10 nm. (Provided by Dr. Ye Cai)

Magnesium silicate formation could be expected from reactions (2.4) and (2.5), as well as from the Mg-Si-O phase diagram[19]. From the phase diagram, a layer bearing $MgSiO_3$ may be expected nearest the quartz substrate and a layer bearing $Mg_2SiO_4$ may be expected nearest the MgO/Si product[27]. For these samples, a single amorphous layer

of magnesium silicate was found instead. Unlike the crystalline line compounds forsterite ($Mg_2SiO_4$) and enstatite ($MgSiO_3$), amorphous magnesium silicate phases may possess a range of Mg:Si cation ratios[28].

To further investigate the composition of this amorphous silicate layer, annealing of the reacted samples was carried out under gettered Ar at 750 °C for 24 hrs (the method of which is described in Chapter 3) to induce crystallization of the amorphous matrix. The results of annealing are shown in Figure 2.7. The amorphous silicate is found to crystallize into forsterite uniformly across the thickness of the layer. No additional crystalline phases were found to form in the layer after annealing. As forsterite is a line compound, additional oxides (MgO or $SiO_2$) would need to form if the Mg:Si ratio of the amorphous silicate was not 2:1[28]. As no additional oxides were found in the layer after forsterite crystallization, the composition of the starting amorphous silicate must be very near $Mg_2SiO_4$.

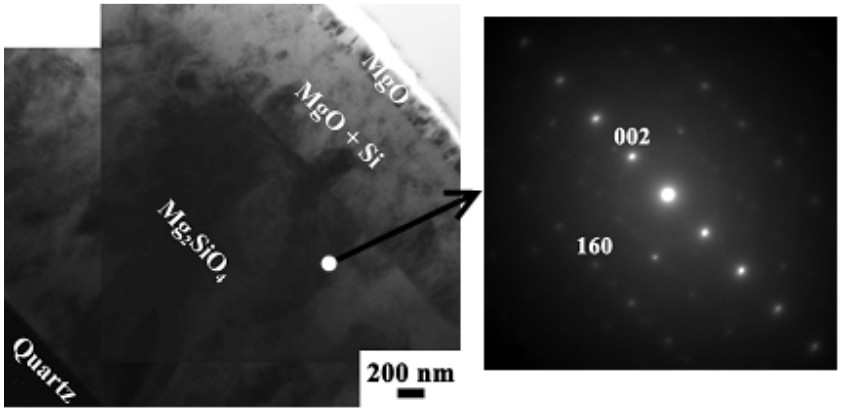


Figure 2.7: SAED analysis of magnesium silicate product layer after annealing in gettered Ar demonstrating the crystallization of amorphous magnesium silicate to forsterite. (Provided by Dr. Ye Cai)

The internal magnesium silicate bearing product layer may be the result of reaction (2.5), or may possibly be the result of the reaction of the MgO product with $SiO_2$ according to the reaction:

$$2MgO + SiO_2 \rightarrow Mg_2SiO_4 \quad (2.26)$$

If the magnesium silicate bearing layer is the result of reaction (2.5), then nanocrystalline Si should be found near the Mg silicate product/$SiO_2$ substrate interface. This is opposed to the phase distribution which should result from reaction (2.26), where it is expected that nanocrystalline Si would not be found in the magnesium silicate bearing layer well away from the interface made with the MgO/Si product layer. HRTEM imaging, presented in Figure 2.8, provided evidence of nanocrystalline Si near the Mg silicate product/$SiO_2$ substrate interface, demonstrating that the magnesium silicate product was a result of reaction (2.5).

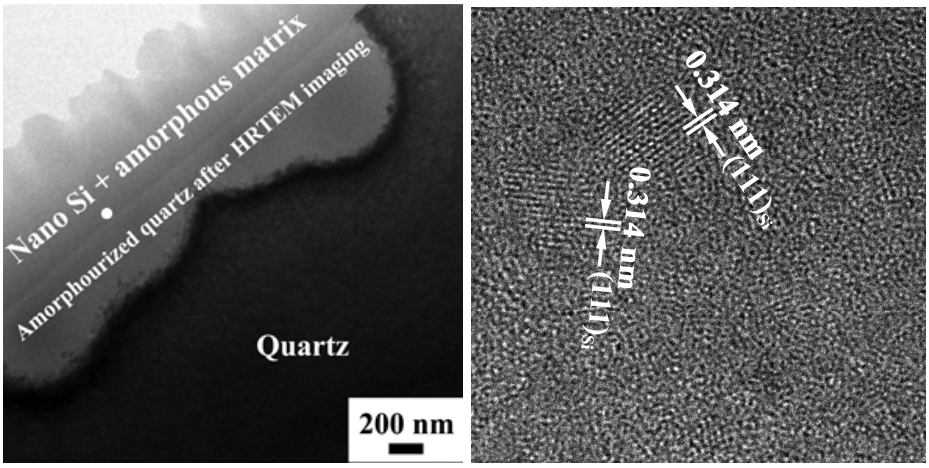


Figure 2.8: HRTEM imaging of nanocrystalline Si found near the interface of the Mg silicate product layer and the unreacted $SiO_2$ substrate: (Left) high magnification image of Mg silicate/quartz interface, and (Right) lattice-fringe image of nanocrystalline Si in spot indicated in the above. (Provided by Dr. Ye Cai)

The formation of an amorphous silicate from monocrystalline quartz is a point of interest. This reaction likely belongs to a class of reactions known as solid-state amorphization reactions (SSAR). A number of SSAR systems have been identified, including solid-state reaction couples involving late-transition metals (such as Co, Fe, and Ni) coupled with early-transition metals (such as Hf, Ti, Zr)[29] and gas-solid reactions between, for instance, $H_2$-$ZrRh_3$[30] and $N_2$-$SmCo_5$[31]. Within this class of reactions, an amorphous product is generated from the solid-state reaction of crystalline reactants. The general criteria identified by Johnson[29,30] for such a reaction to occur are: 1) the reaction must possess a high heat of mixing, and 2) diffusion of one reactant species must be significantly greater than the other species involved. Criterion (1) is required to drive the conversion of the initially crystalline phases to an amorphous product. The diffusional asymmetry as described by criterion (2) can be envisioned as the fast diffusing species breaking bonds and forming new compounds around the relatively slow-diffusing species. The result is that a new phase is formed around the slow-diffusing species, the immobility of which inhibits the formation of a new crystalline phase.

Criterion (1) cannot be strictly applied to the Mg-$SiO_2$ system, in which reaction occurs readily and a solid solution cannot be formed. While work in SSAR has largely centered on the formation of amorphous metal alloys, this phenomenon has also been observed to occur in oxide systems (such a $ZrO_2$-$TiO_2$)[32]. It can be noted, however, that the $\Delta G$ of the reaction:

$$2Mg(g) + 2SiO_2 \rightarrow Mg_2SiO_4(l) + Si \qquad (2.27)$$

(where liquid $Mg_2SiO_4$ is used as an approximation for amorphous $Mg_2SiO_4$) has a value of -96.0 kJ $mol^{-1}$ at 700 °C and a $p_{Mg}$ in equilibrium with $Mg_2Si$, which is not greatly

lower than that for the formation of crystalline $Mg_2SiO_4$ (-129.4 kJ $mol^{-1}$)[20]. With respect to criterion (2), the diffusion coefficients of $Mg^{2+}$, $Si^{4+}$, and $O^{2-}$ in quartz are summarized in Table 2.6. The diffusion of $Si^{4+}$ is several orders of magnitude slower than the diffusion of $O^{2-}$ or $Mg^{2+}$ (it should be noted that $Si^{4+}$ likely diffuses as part of an $SiO_x$ species). The amorphous structure of the magnesium silicate product is then likely the result of the relative immobility of $Si^{4+}$, which inhibits the formation of an orthorhombic olivine phase (forsterite) from the hexagonal quartz phase.

Table 2.6: Diffusion coefficients in quartz.

| Species | *D* in Quartz at 700°C ($cm^2$ $s^{-1}$) |
|---|---|
| $Si^{4+}$ | $6.31x10^{-34}$ [33a] |
| $O^{2-}$ | $1.26x10^{-14}$ [33b] |
| $Mg^{2+}$ | $2.51x10^{-16}$ [33c] |

### 2.4.2 Interfacial Reaction and Diffusional Pathway Analysis of Gas-Solid Silica Magnesiothermic Reduction on Quartz

After determining the product film structure and composition of quartz subjected to Mg(g)/$SiO_2$ reduction at 700-750 °C, possible reaction pathways were constructed and assessed. Possible diffusional steps and interfacial reactions involved in Mg(g)/$SiO_2$ reduction on quartz are summarized in Figure 2.9. It is assumed here that the conduction of electron and/or holes across the product layers is fast relative to both the diffusion of $Mg^{2+}$ and $O^{2-}$. The continuous Si phase in the MgO/Si layer should provide for fast electron/hole transport, while the $Mg_2SiO_4$ matrix is expected to be a predominantly electronic conductor[34]. For the sake of brevity, the interfaces in this reaction have been

labeled G (for the gas/solid external surface), A (for the external/internal product layer interface), and B (for the internal product layer/quartz substrate interface). The external MgO/Si layer is abbreviated as I, and the internal Mg silicate/Si layer is abbreviated as II. The growth of a magnesiothermically-reduced product film on quartz can, in principle, proceed either by the inward diffusion of Mg (Case I in Figure 2.9) or by the outward diffusion of O and Si (Case II in Figure 2.9).

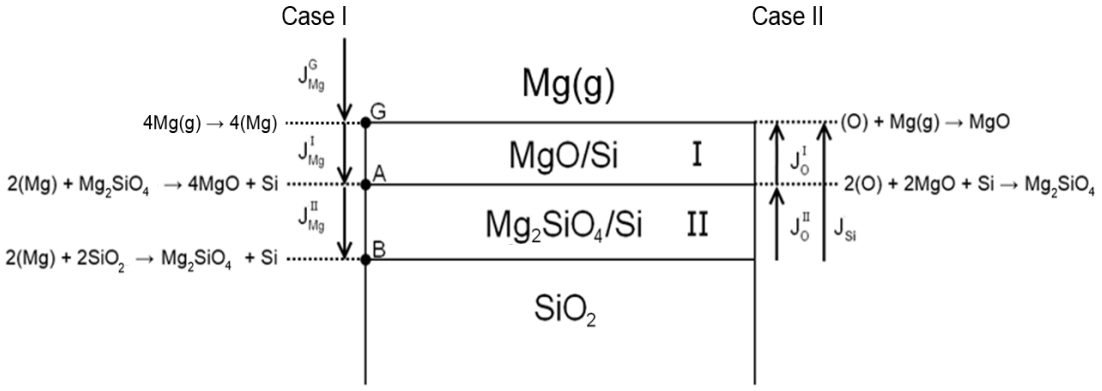


Figure 2.9: Proposed diffusional steps and interfacial reactions involved in magnesiothermic reduction of quartz: Case I: Inward diffusion of Mg, Case II: Outward diffusion of O and Si.

Marker experiments were used to determine whether Case I or Case II of Figure 2.9 occurs during reaction. Two means of marking the initial surface of the sample were used. First, an experiment involving 20 nm Ag inert markers, which were sputtered onto the polished surface of the quartz substrates before reaction, was carried out to determine if diffusion outward through the external product surface was predominantly occurring. After reaction at 750 °C for 1 hr, the inert markers were found to remain on the surface of the sample, implying that the reaction primarily proceeded through the inward diffusion

of Mg (Figure 2.10), since the smallest Ag particles (~20 nm) found on the surface were significantly smaller than the thickness of the MgO/Si product layer (~800 nm). Additionally, large ~200 nm Ag particles are found on the surface as well, which is still smaller than the 800 nm MgO/Si product layer. Second, the roughness of the initial quartz surface was used to determine if product growth occurred at interface G. Before reaction, AFM measurements (provided by Brandon Goodwin) determined the initial quartz surface to have an $R_a$ roughness of 0.6 nm. After reaction, only a slight roughening was found to occur, as the $R_a$ roughness was found to be 4.1 nm. The surface roughness after reaction is noticeably less than that of the MgO and Si grain sizes as determined by Scherrer analysis (36.3 nm and 17.6 nm respectively). The well-maintained surface polish suggests that a reaction producing new solid phases does not occur at this interface. The agreement of these marker experiment results suggests that the reaction proceeds by the inward diffusion of Mg (Case I of Figure 2.9).

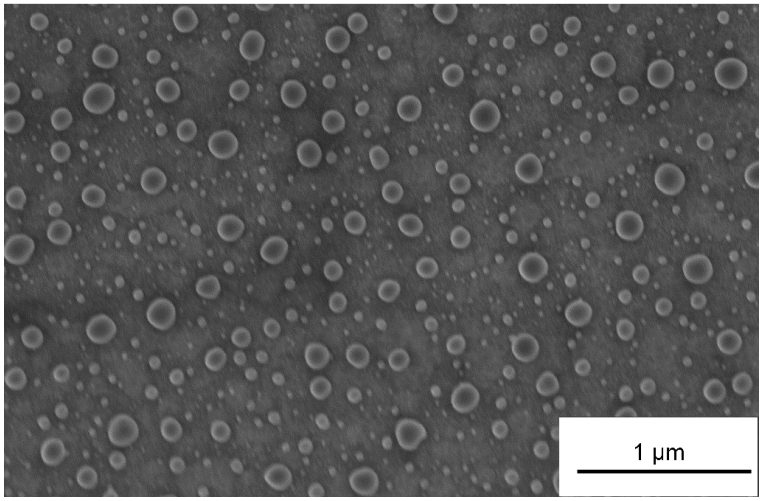


Figure 2.10: Ag inert marker nanoparticles on the surface of a quartz sample magnesiothermically-reduced at 750 °C for 1 hour.

Case I of Figure 2.9 was further expounded upon in Figure 2.11. The net reaction to produce layers I and II is:

$$4Mg(g) + 2SiO_2 \rightarrow 4MgO + 2Si \quad (2.28)$$

Defect-based reactions were constructed at each interface. At interface G, Mg gas dissociates into $Mg^{2+}$ and $2e^-$, according to the equation:

$$4Mg(g) \rightarrow 4Mg_{i(Si)}^{\bullet\bullet} + 8e' \quad (2.29)$$

where $Mg^{2+}$ is accepted into layer I as interstitials in the Si grains (denoted by $4Mg_{i(Si)}^{\bullet\bullet}$). The stoichiometry of this reaction (involving 4Mg(g)) is based on the stoichiometry of reaction (2.28). After the absorption of Mg(g), Mg diffuses inward toward the unreacted $SiO_2$ substrate. In principle, across layer I, the Mg flux can follow one of three diffusion pathways: 1) Mg can diffuse through MgO grains through a vacancy self-diffusion mechanism, 2) Mg can diffuse interstitially through Si grains, or 3) Mg can diffuse along Si/MgO interphase boundaries. Diffusion coefficients of $Mg^{2+}$ across MgO and Si are summarized in Table 2.7. As $Mg^{2+}$ vacancies are dependent upon the concentration of substitutional dopant cations, $D_{Mg2+}$ in MgO is shown as a function of potential Si dopant concentrations. No data could be found for the diffusion of $Mg^{2+}$ interstitials in Si. Instead, in Table 2.7, $Na^+$ interstitial diffusion data is used as an approximation, as $Mg^{2+}$ and $Na^+$ have similar solubilities in Si and both are shallow donors in Si[35]. Mg is known to be a shallow, divalent donor in Si, meaning that it is expected that $Mg^{2+}$ will diffuse separately from free electrons in Si[36]. To the current author's knowledge, no data exists on the diffusion of Mg along Si/MgO interphase boundaries. As seen in Table 2.7, the diffusion of $Mg^{2+}$ interstitials through Si is expected to be significantly greater than the self-diffusion of $Mg^{2+}$ in MgO. As there lacks data for Mg diffusion along Si/MgO

interphase boundaries, then for the sake of the current work, it is assumed that Mg diffuses as $Mg^{2+}$ interstitials across Si grains in parallel with free electrons.

Table 2.7: Comparison of diffusion coefficients for $Mg^{2+}$ in MgO and Si

| Temperature (°C) | $D_{Mg2+}$ ($cm^2$ $s^{-1}$) | | | |
|---|---|---|---|---|
| | Vacancy Self-Diffusion in MgO[23a] | | | Interstitial Diffusion in Si[35] |
| | 1 ppb Si | 1 ppm Si | 100 ppm Si | |
| 650 | $1.35x10^{-22}$ | $1.35x10^{-19}$ | $1.35x10^{-17}$ | $3.34x10^{-15}$ |
| 750 | $2.23x10^{-21}$ | $2.23x10^{-18}$ | $2.23x10^{-16}$ | $6.69x10^{-14}$ |
| 850 | $2.23x10^{-20}$ | $2.23x10^{-17}$ | $2.23x10^{-15}$ | $7.87x10^{-13}$ |
| 900 | $6.08x10^{-20}$ | $6.08x10^{-17}$ | $6.08x10^{-15}$ | $2.30x10^{-12}$ |

At interface A, a fraction of the $Mg^{2+}$ and free electron flux is consumed to drive the growth of the MgO/Si product layer according to the reaction:

$$2Mg_{i(Si)}^{\cdot\cdot} + 4e' + Mg_2SiO_4 \rightarrow 4MgO + Si \quad (2.30)$$

At interface A, a fraction of the $Mg^{2+}$ flux is consumed to drive the growth of I, while the remainder of the flux travels farther inward to react with $SiO_2$ and drive the growth of II. The transfer of $Mg^{2+}$ flux from I to II can be represented by the reaction:

$$4e' + 2Mg_{i(Si)}^{\cdot\cdot} + 2V_{Mg}''* \rightarrow 4e'* + 2Mg_{Mg}* + 2V_{Mg}'' \quad (2.31)$$

where defects with asterisks occur in a-$Mg_2SiO_4$ (amorphous $Mg_2SiO_4$) and those without occur in MgO (note: lattice defects do not technically occur in amorphous phases, but for the purposes of the current argument, $Mg^{2+}$ diffusion is treated as occurring by a vacancy transport mechanism in amorphous $Mg_2SiO_4$). At interface B, inwardly diffusing $Mg^{2+}$ and free electrons consume $SiO_2$ according to the reaction:

$$2Mg_{Mg}^{*} + 4e'^{*} + 2SiO_2 \rightarrow Mg_2SiO_4 + Si + 2V_{Mg}''^{*} \quad (2.32)$$

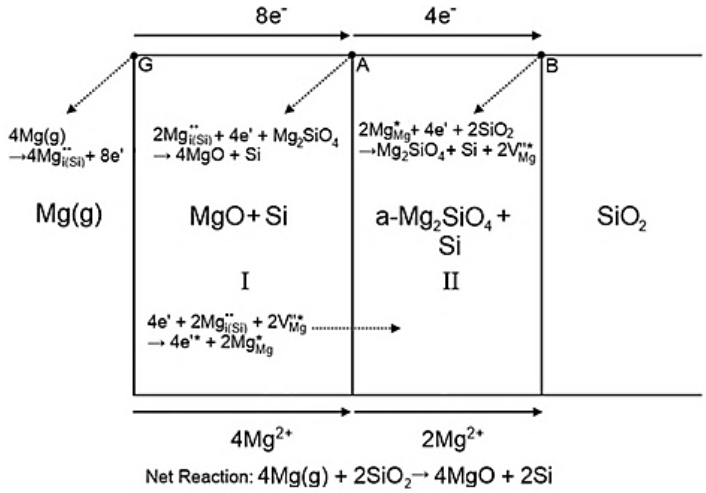


Figure 2.11: Diagram of interfacial reactions and diffusional mechanisms occurring for the case of Mg(g)/$SiO_2$ reduction as a result of the inward diffusion of Mg.

### 2.4.3 Kinetic Analysis of Magnesiothermic Reduction on Quartz – Rate-limiting Steps

Following the analysis of diffusional pathways and interfacial reactions in the previous section, cross-sectional imaging of reacted quartz samples was used to determine the rate of magnesiothermic reduction on these substrates. In addition to growth rate information, such measurements will allow for the determination of the rate-limiting steps involved in this reaction. At 700 °C, samples were reacted for up to 8 hrs. At 750 °C, samples were reacted for up to 4 hrs, as it was found that the underlying unreacted quartz fractured after longer reaction times. After reaction, samples were cleaved and subjected to a 250 mM aqueous HCl bath for 30 s to selectively etch the magnesium silicate layer so that the boundary between the MgO/Si and Mg silicate/Si

layers could be clearly identified. The results are depicted in Figure 2.12 and Figure 2.13. With such growth rate information, the procession of the reaction can be more clearly understood.

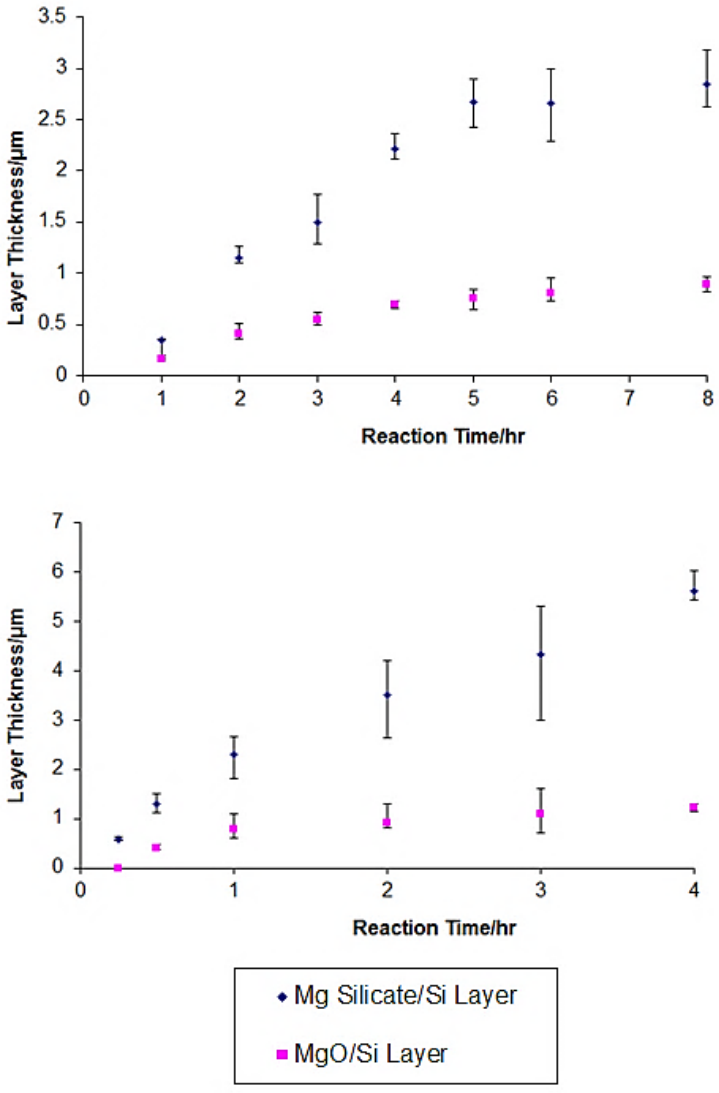


Figure 2.12: Cross-sectional thickness measurements as a function of time for z-cut quartz wafers magnesiothermically-reduced at (Top) 700 °C and (Bottom) 750 °C. Error bars indicate full range of measured data.

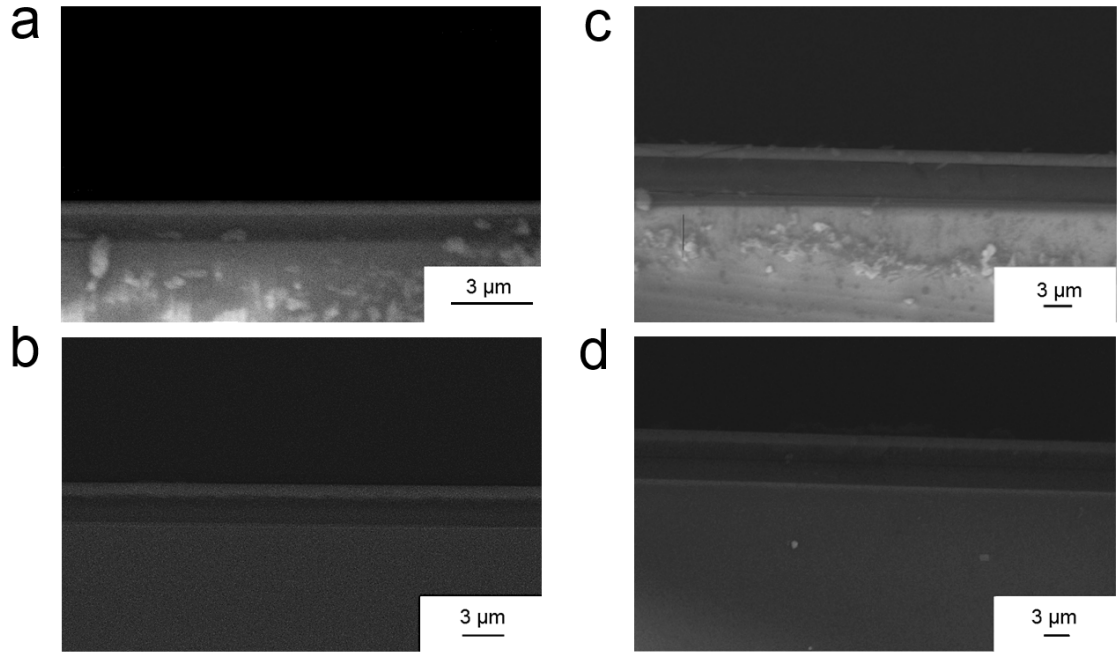

Figure 2.13: Cross-sectional SE images of product films on reacted quartz wafers treated at: a) 700 °C for 1 hr, b) 750 °C for 1 hr, c) 700 °C for 8 hrs, and d) 750 °C for 4 hrs.

To examine rate-limiting steps, first, the growth of I will be treated. As II is consumed by I during the overall reaction, the growth of II will be partially dependent on I. Following the analysis presented in section 2.4.2, the growth of I is considered to proceed at A according to reaction (2.30). Several steps of the prcoess may be rate-limiting for the growth of I. The rate-limiting step may be evaluated through the rate law found to describe product layer growth. One possible rate-limiting step is diffusion of $Mg^{2+}$ across the thickening layer I ($J_{Mg}^{I}$ in Figure 2.9). If $J_{Mg}^{I}$ were the rate-determining step, then a parabolic rate law could be followed for growth of I (assuming the diffusion pathway of $Mg^{2+}$ does not change with product layer thickness).

Alternatively a linear rate law may be found, which would be consistent with control by gas-phase diffusion across a constant stagnant gas thickness ($J_{Mg}^{G}$ in Figure

2.9) or the reaction rate at the interface, which means a linear rate law alone would be ambiguous as to the rate-determining step. To eliminate one of these possibilities, gas-phase diffusion control was tested by varying the number of YSZ cloth layers in the partition for samples reacted at 750 °C for 1 hr (i.e., manipulating $J_{Mg}^{G}$ through the diffusion distance of Mg gas). The results of product layer thickness measurements on samples reacted using different partition thicknesses are shown in Table 2.8. No consistent variation of either the internal (I) or external (II) product layer was found with variable partition thickness, which would rule out $J_{Mg}^{G}$ as rate-determining. Therefore, reaction rate control is then the only likely feature which would result in a linear rate law.

Table 2.8: Effect of YSZ cloth partition thickness on product film growth for quartz samples magnesiothermically-reduced at 750 °C for 1 hr.

| No. of YSZ Cloth Layers in Partition | Total Thickness of Cloth Partition (mm) | Thickness of Mg Silicate/Si Layer (μm) | Thickness of MgO/Si Layer (nm) |
|---|---|---|---|
| 1 | 0.26 | 2.09 ± 0.135 | 743 ± 121 |
| 2 | 0.51 | 2.57 ± 0.245 | 760 ± 119 |
| 4 | 1.02 | 2.01 ± 0.301 | 657 ± 198 |
| 6 | 1.53 | 1.62 ± 0.540 | 807 ± 104 |
| 8 | 2.04 | 2.42 ± 0.214 | 775 ± 156 |

Linear and parabolic fits to layer I thickness data are given in Table 2.9, and shown overlaid onto the measured thicknesses of layer I in Figure 2.14. A parabolic rate law produced a significantly better fit than a linear rate law for the measured data. A parabolic plot of the measured thickening data is given in Figure 2.15. The parabolic behavior of the measured data is reinforced by the power law fitting of the data given in Table 2.10 and Figure 2.16. From the fitted data and inert marker experiments, it may be

surmised that the growth of layer I is controlled by the inward diffusion of $Mg^{2+}$ across the MgO/Si product layer.

Table 2.9: Rate law fitting for growth of I (MgO/Si product layer) measured in Figure 2.12.

| | 700 ˚C | | 750 ˚C | |
|---|---|---|---|---|
| Fitted Rate Law | Fit | $R^2$ | Fit | $R^2$ |
| Linear: kt+C | 0.099t+0.198 | 0.888 | 0.280t+0.243 | 0.808 |
| Parabolic: $kt^{1/2}$+C | $0.401t^{1/2}$-0.171 | 0.962 | $0.756t^{1/2}$-0.170 | 0.904 |

Table 2.10: Power law fitting for growth of I (MgO/Si product layer) shown in Figure 2.16.

| | Linear Fit of Logarithmic Scale Thickness Data |
|---|---|
| 700 °C | **0.567**log(t)-0.531 |
| 750 °C | **0.494**log(t)-0.185 |

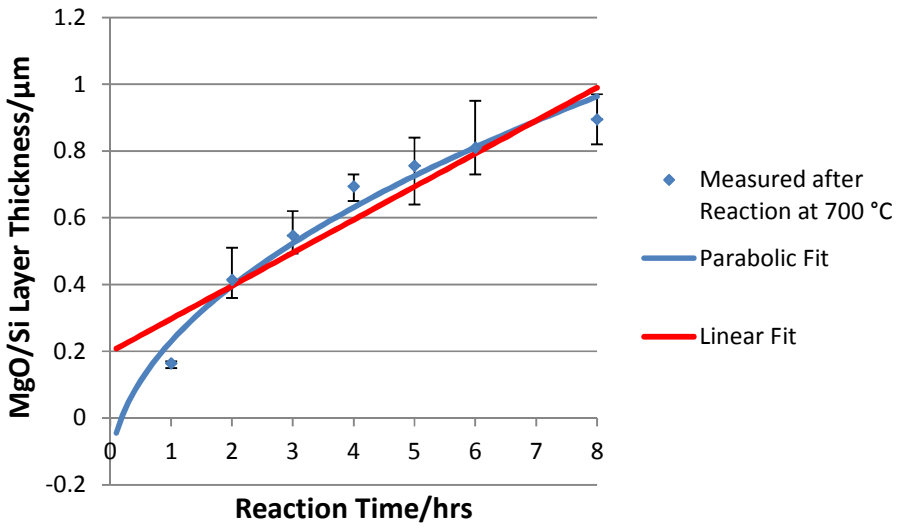


Figure 2.14: Fitted rate laws of Table 2.9 overlaid upon measured thicknesses of MgO/Si product layer after reaction at (top) 700 °C and (bottom) 750 °C.

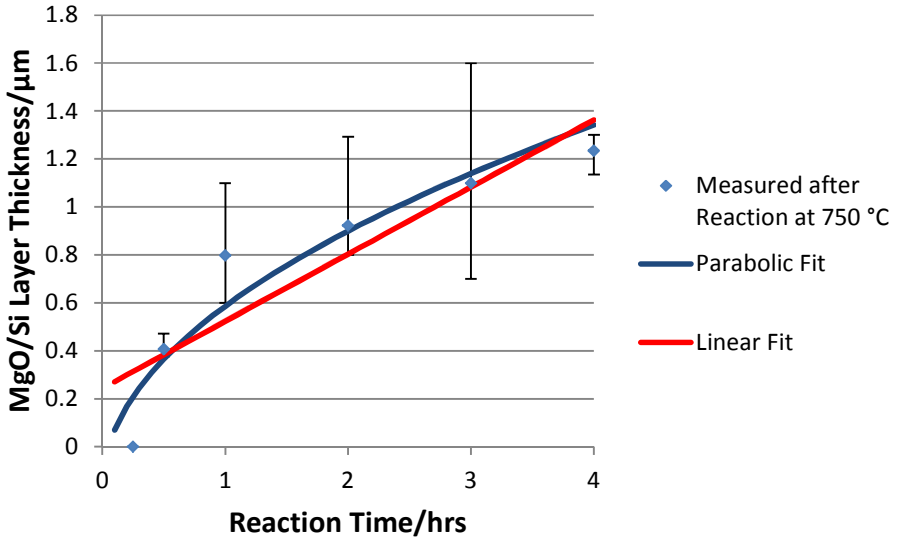


Figure 2.14 continued

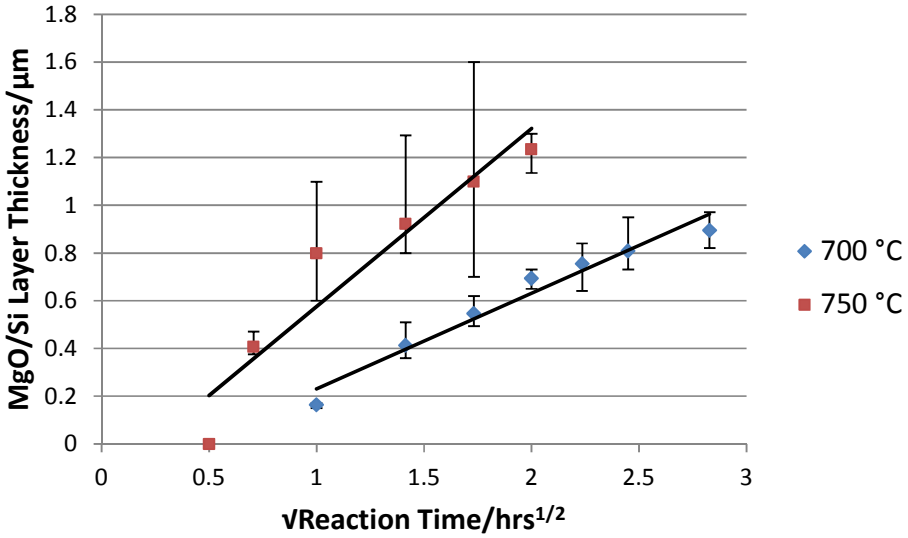


Figure 2.15: Parabolic plot of measured thicknesses of MgO/Si product layer after reaction at 700 °C and 750 °C.

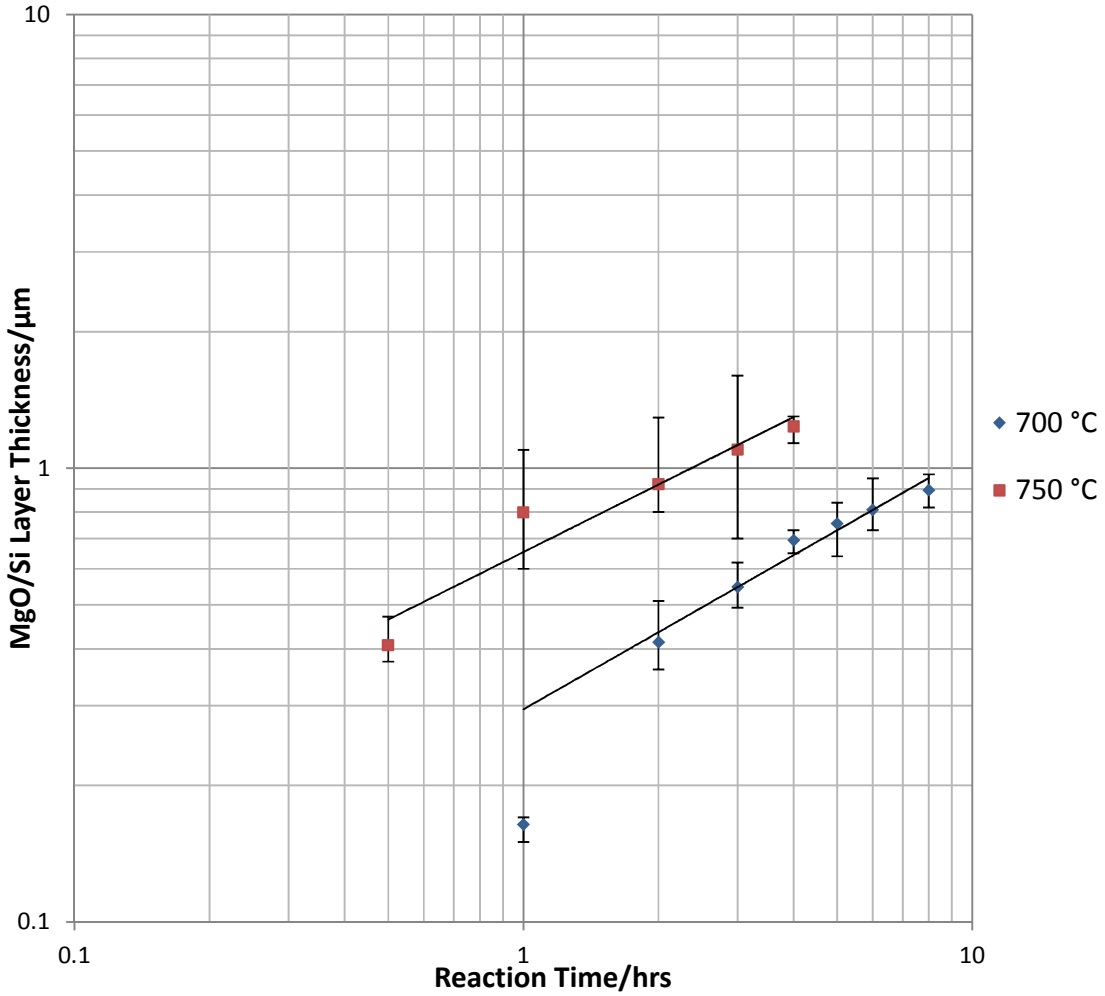

Figure 2.16: Logarithmic scale plot and power law fitting of measured thicknesses of MgO/Si product layer after reaction at 700 °C and 750 °C.

By identifying the growth of layer I as following a parabolic rate law, possibilities may be constructed for the growth of layer II. For layer II, following the analysis in section 2.4.2, growth is expected to occur at interface B. The rate laws governing the growth of layer II are more complex given that this layer is being consumed by layer I during reaction. Growth of layer II may be reaction rate limited or may be diffusion limited by $J_{Mg}^{I}$ or $J_{Mg}^{II}$. Rate laws for these two cases can be evaluated from:

$$\frac{\partial \Delta_{II}}{\partial t} = \frac{\partial \Delta^*_{II}}{\partial t} - S\frac{\partial \Delta_I}{\partial t} \tag{2.33}$$

where $\Delta^*_{II}(t)$ is the thickness of layer II if growth of layer I did not occur, $\Delta_I$ and $\Delta_{II}$ are the real thicknesses of layers I and II respectively, and S is a proportionality factor that accounts for possible expansion of layer II during conversion into layer I in the surface normal direction. For the following analysis, $\Delta_I(t)$ will be represented with the generic parabolic rate law:

$$\frac{\partial \Delta_I}{\partial t} = \frac{k_I}{\Delta_I} \tag{2.34}$$

where $k_I$ is a constant. For the case of reaction rate control, $\Delta^*_{II}$ is considered to follow the generic linear rate law:

$$\frac{\partial \Delta^*_{II}}{\partial t} = k_{II} \tag{2.35}$$

and substituting equations (2.38) and (2.39) into (2.37) produces:

$$\Delta_{II} = k_{II}t - S(2k_I)^{1/2}t^{1/2} + C \tag{2.36}$$

where C is an integration constant. This represents a "modified" linear rate law for the case in which growth of layer II is controlled by the reaction rate at interface B.

The case of diffusion controlled growth is more complicated. In principle, either $J_{Mg}^{I}$ or $J_{Mg}^{II}$ could be rate-limiting for growth of layer II, but $J_{Mg}^{II}$ is not independent of $J_{Mg}^{I}$, as detailed in section 2.4.2. It can be seen from (2.28), (2.30), and (2.31) that Mg arriving at A will be partitioned between Mg that drives reaction at A (to grow layer I) and Mg that diffuses forward to B (to react with $SiO_2$ and grow layer II). As a result,

Yurek, Hirth, and Rapp have shown that this situation reduces to a simple parabolic rate law[37]. Therefore for $J_{Mg}$ control, $\Delta_{II}$ will follow a parabolic rate law.

Data was fitted to the above rate laws in Table 2.11, and shown overlaid onto the measured thicknesses of layer II in Figure 2.17. For layers grown at 750 °C, the modified linear rate law and the parabolic rate law produce nearly identical fits. A parabolic plot of the thickening data is shown in Figure 2.18. Power law fittings of the thickening data are given in Figure 2.19 and Table 2.12. The best fit of the "modified" linear rate law returns values for $k_I$ that are negative, which is an unphysical result. Therefore, only the parabolic rate law produces a fit that can be considered physical in this circumstance. Accordingly, the growth of layer II appears to be rate-limited by the inward diffusion of Mg across product layers I and II.

Table 2.11: Rate law fitting for growth of II (Mg silicate/Si product layer) measured in Figure 2.13.

| | 700 ˚C | | 750 ˚C | |
|---|---|---|---|---|
| Fitted Rate Law | Fit | $R^2$ | Fit | $R^2$ |
| Modified Linear: $k_{II}t-S(2k_I)^{1/2}t^{1/2}+C$ | $-0.515t+3.42t^{1/2}-2.63$ | 0.975 | $0.179t+2.767t^{1/2}-0.766$ | 0.995 |
| Parabolic: $k*t^{1/2}+C$ | $1.46t^{1/2}-0.931$ | 0.937 | $3.21t^{1/2}-0.992$ | 0.994 |

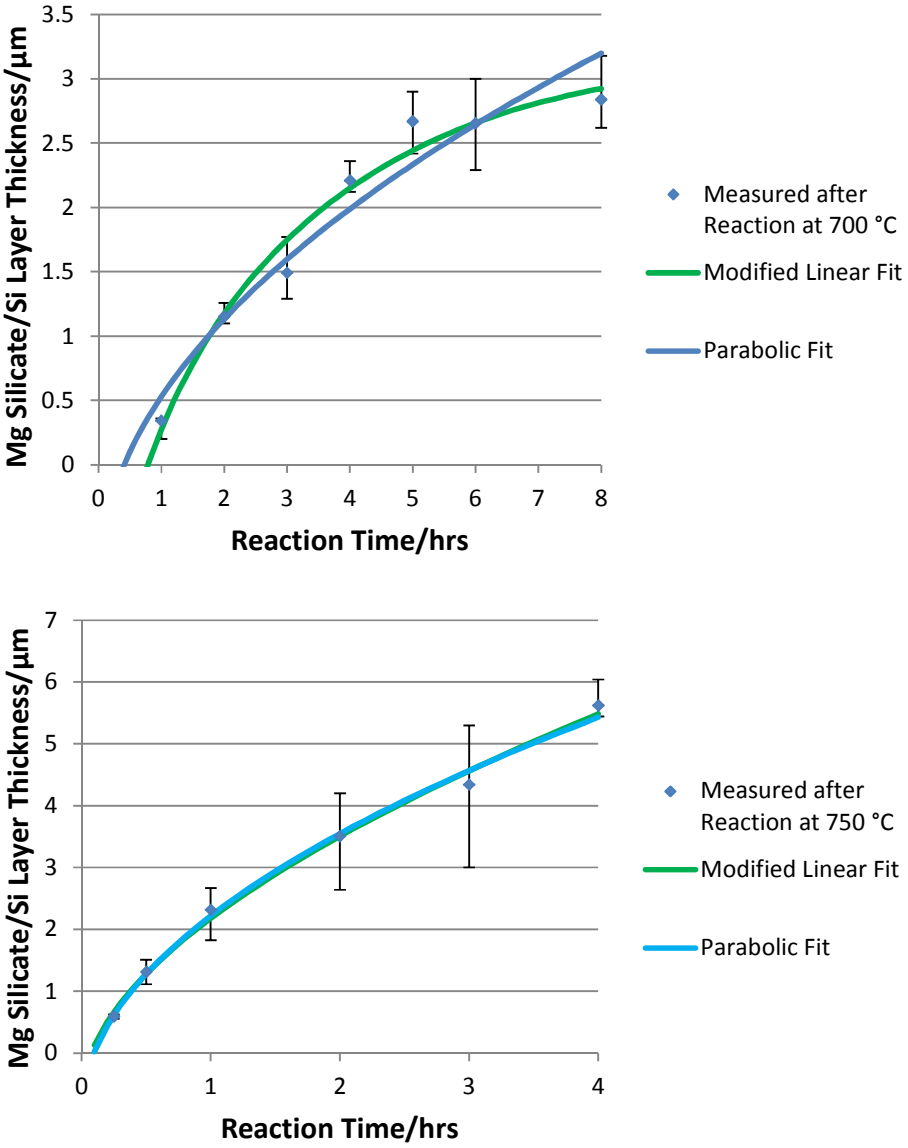


Figure 2.17: Fitted rate laws of Table 2.11 overlaid upon measured thicknesses of Mg silicate/Si product layer after reaction at (top) 700 °C and (bottom) 750 °C.

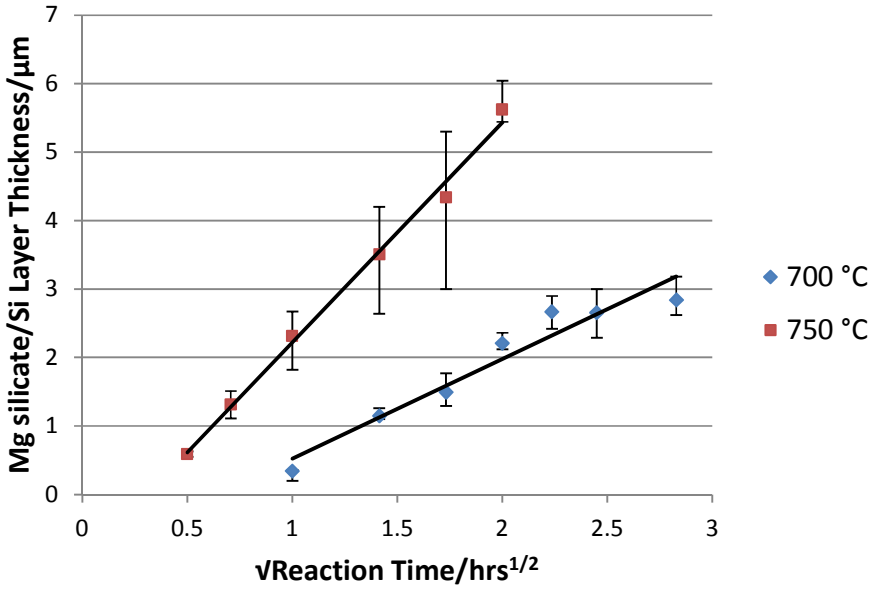


Figure 2.18: Parabolic plot of measured thicknesses of Mg silicate/Si product layer after reaction at 700 °C and 750 °C.

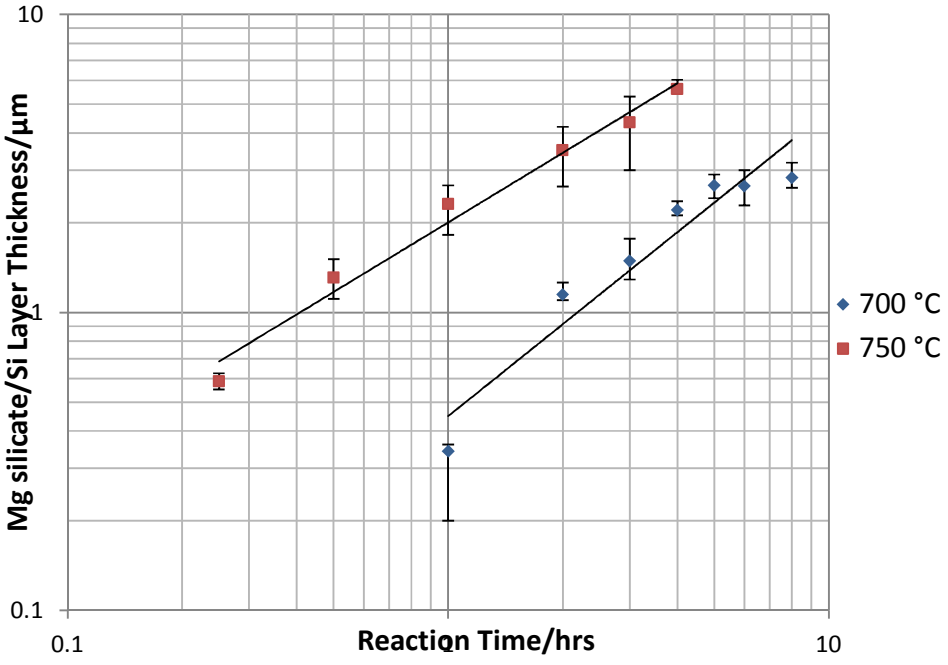


Figure 2.19: Logarithmic scale plot and power law fitting of measured thicknesses of Mg silicate/Si product layer after reaction at 700 °C and 750 °C.

Table 2.12: Power law fitting for growth of II (Mg silicate/Si product layer) shown in Figure 2.19.

| | Power Law Fit of Measured Thicknesses |
|---|---|
| 700 °C | **1.025**log(t)-0.348 |
| 750 °C | **0.775**log(t)+0.302 |

At this point, we can return to the question posed earlier in this chapter. The interwoven aggregate product morphology is found to result from reactions in systems where the product and reactants display a broad mutual solubility range. In the Mg-Si-O system at equilibrium, only line compounds are formed, which places the results of Mg(g)/$SiO_2$ reduction found here at odds with prior work in solid-state displacement reactions. The product phases of Mg(g)/$SiO_2$ reduction (MgO/Si) show an interwoven ("co-continuous") morphology that is robust enough that MgO (which comprises ~65 vol. % of the structure) can be etched from the structure to produce an interconnected, shape-preserved, porous skeleton of Si.

A crystalline magnesium silicate may possess only two possible MgO:$SiO_2$ ratios (2:1 and 1:1)[19]. However as seen in TEM cross-sectional analysis, an amorphous magnesium silicate layer forms between the MgO/Si product and the $SiO_2$ substrate, a likely result of a solid-state amorphization reaction. As demonstrated by the work of Nuth, et al., an amorphous magnesium silicate may possess a wide range of MgO:$SiO_2$ ratios (found to be as low as 0.8 and as high as 16.0)[38]. The amorphous magnesium silicate must then be critical to the formation of an interwoven MgO/Si product.

Tangchitvittaya, et al. provided the first model for the growth of an interwoven aggregate product morphology from a solid-state displacement reaction[21]. Their model

describes the tortuous, branching nature of the product phases as the result of complex, 3-dimensional composition gradients that occur ahead of the reaction front. It is conceivable then that composition gradients in the amorphous magnesium silicate may be responsible for growth of an interwoven MgO/Si product layer, since the MgO/Si product layer is found to consume the magnesium silicate during

## 2.5 Summary

A mechanism of growth for the interwoven MgO/Si composite product of silica magnesiothermic reduction has been presented. A two-layer product film formed when quartz was reacted with Mg gas at 700-750 °C. The most advanced layer was composed of an amorphous Mg silicate/Si composite. The layer adjacent to the external surface was composed of a nanocrystalline mixture of MgO/Si. The growth of both product layers was determined to occur by Mg diffusion inward to the reaction fronts. The MgO/Si layer was found to thicken by consumption of the Mg silicate/Si layer. Complex, 3-dimensional concentration gradients of Si and Mg in the amorphous silicate ahead of the MgO/Si growth front are believed to be responsible for the complex, tortuous pathways the MgO/Si phases take as they grow.

# CHAPTER 3:

# STRESS EVOLUTION AND RELAXATION DURING GAS-SOLID SILICA MAGNESIOTHERMIC REDUCTION

## 3.1 Introduction

In the previous chapter, the reaction kinetics of the Mg(g)/$SiO_2$ reduction reaction were explored to explain the growth of a two-phase interwoven product of MgO/Si which is sufficiently structurally robust so as to survive selective removal of the MgO constituent. In the current chapter, an additional consideration is given to the volume expansion-induced stresses that develop in the product film and occur as a result of the Mg(g)/$SiO_2$ reduction reaction.

The growth of a two-phase MgO/Si product on a $SiO_2$ substrate according the reaction:

$$2Mg(g) + SiO_2 \rightarrow 2MgO + Si \qquad (1.1)$$

results in the formation of 2 moles MgO and 1 mole Si for each mole of $SiO_2$ reacted. All polymorphs of $SiO_2$ have a lower molar volume than this two-phase product mixture. Therefore, there should be a significant compressive stress that evolves in a growing MgO/Si product film formed on $SiO_2$. Nevertheless, appreciable geometric distortions or damage is not observed to occur to the template structure, regardless of complexity, after reaction. In this chapter, it is hypothesized that a mechanism of stress relaxation must be operative during this reaction to allow for the formation of high-fidelity geometric replicas of complex-shaped $SiO_2$ templates.

The goal of the work presented in this chapter is to identify a mechanism operating during Mg(g)/$SiO_2$ reduction that can account for the apparent stress relaxation that occurs during this reaction. Planar quartz specimens have been used as a reaction substrate for MgO/Si product films, and XRD-based residual stress analysis has been used to probe the stress state of these product films. After reaction of the quartz to generate product films, annealing treatments have been used to induce stress relaxation in the products. In the post-annealed samples, stress measurements have been correlated to microstructural changes to identify a stress-relaxation mechanism.

## 3.2 Theory

For each mole of $SiO_2$ undergoing reaction (1.1), 2 moles of MgO and 1 mole of Si are produced. As shown in Table 3.1, this product mixture has a greater molar volume than all polymorphs of $SiO_2$. For instance, the product of (1.1) has a 20% volume expansion over diatomaceous earth silica[39d]. However, in previous studies of shape-preserving magnesiothermic reduction of such structures, the dimensions of the observed reacted structures cannot account for this volume change. During magnesiothermic reduction, layers of the MgO/Si product mixture must then be in a state of compression, constrained by unreacted silica beyond the reaction front. Distortion and/or cracking in converted structures are not observed, which suggests that a stress relief mechanism is operative during the reaction.

Table 3.1: Expansion of magnesiothermic reduction products over silicas.

| | Molar Volume ($cm^3\ mol^{-1}$) | Expansion Upon Magnesiothermic Reduction |
|---|---|---|
| MgO | 11.26 [24a] | n/a |
| Si | 12.05 [24b] | n/a |
| Fused Silica | 26.11 [39a] | 32% |
| Quartz | 21.65 [39b] | 60% |
| Cristobalite | 25.79 [39c] | 34% |
| Diatom Silica | 28.61 [39d] | 20% |

The experiments in this chapter will explore possible mechanisms of stress relief that may occur during the Mg(g)/$SiO_2$ reduction process. In the past, silica structures of many complicated geometries have been subjected to this reaction. For this work, simple planar specimens of silica were preferred. Possible mechanisms of stress relief that may occur during this reaction, which are initially considered, are: 1) stress relaxation via stress-induced migration, 2) stress relaxation via grain coarsening and/or recrystallization, 3) stress relaxation via geometric distortion, and 4) stress relaxation via a reduction in film density through the formation of a volatile product. Planar silica specimens have been partially reacted over a range of times at 750 °C, and the stress state in the reacted zone has been characterized by XRD. Further heat treatments without magnesium have been conducted to induce changes in the residual stress state of the product films. A parallel series of experiments have been conducted to confirm the occurrence of the cases listed above, and to attempt to uncover correlations between those mechanisms and the observed changes in residual stress state.

### 3.2.1 Stress-Induced Migration

The first proposed mechanism to account for stress relaxation in the products of

magnesiothermically-reduced silica is stress-induced diffusion/migration to the external surface of the reacted zone. For this case, the results should show growth of MgO and/or Si on the external surface of the product film. A similar mechanism has been shown to relieve stress during the internal oxidation of noble base metal alloys[40].

Internal oxidation is a well-investigated field that provides some clues to stress relief in magnesiothermically-reduced structures. This process occurs in alloys of noble metal solutes with less noble metals[40]. During oxidation of these alloys, the less noble metal is oxidized, resulting in metal oxide particles dispersed within a matrix of noble metal depleted of the less noble species. Relative to Mg(g)/$SiO_2$ reduction, the processes are comparable in that reaction with a species dissolved from the vapor phase drives the formation of a two-phase product. However, internal oxidation generates a second phase within the depleted parent phase, while Mg(g)/$SiO_2$ reduction generates two new phases from the disappearing parent phase. Regardless, the large volume expansions of the oxide phase over the base alloy can be similar to the volume expansion of the MgO/Si composite product over $SiO_2$.

An important feature observed during internal oxidation is the stress-induced outward diffusion of the noble metal component[40]. The noble metal is found to migrate to the external surface of the oxidized zone to form nodules that can coalesce into an external film. Importantly, a correlation has been found between stress in the oxidized zone and the nodule volume on the external surface. Similar external nodule formation has been observed during Mg(g)/$SiO_2$ reduction (Figure 3.1). A strong impetus then exists to study closely the surface of MgO/Si product films on $SiO_2$ to verify the stress-induced migration of an outwardly diffusing species.

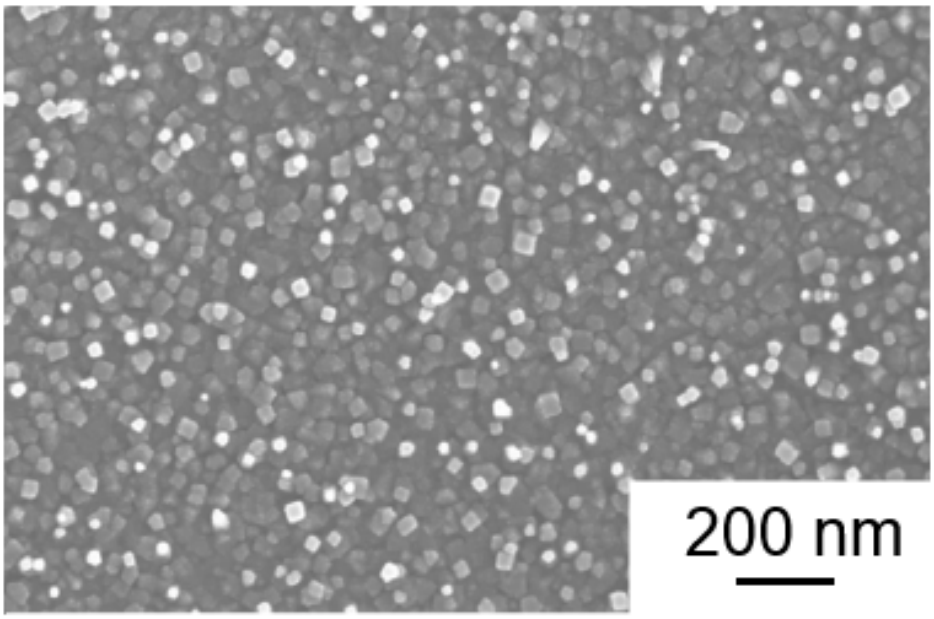


Figure 3.1: Nodule growth on products of Mg(g)/$SiO_2$ reduction: nodule growth on quartz treated in Mg gas at 700 °C for 14 hrs.

### 3.2.2 Recrystallization and Grain Growth

A second proposed stress-relaxation mechanism involves the elimination of defects in the product film (e.g., dislocations, grain/interphase boundaries). Previous theoretical and experimental studies on thin films undergoing grain growth have shown that large tensile stresses can evolve[41]. For thin films under compressive residual stress, these evolved tensile stresses can be large enough to completely relieve residual stress in the film[41]. For this chapter, the MgO and Si grain sizes have been monitored in the product layer with XRD Scherrer analysis.

Grain coarsening has been demonstrated to relax compressive stresses in thin films constrained by a substrate originally by Chaudhari in 1971[41]. Chaudhari attributed

stress relaxation during grain growth to be the result of grain boundary coalescence, which, through reducing the total free volume of grain boundaries within the film, placed grain interiors in a state of tension[41] (illustrated in Figure 3.2). In addition, Chaudhari's model provides descriptions for how the initial strain state of the film affects grain growth, with compressive strains aiding grain growth and tensile strains inhibiting grain growth.

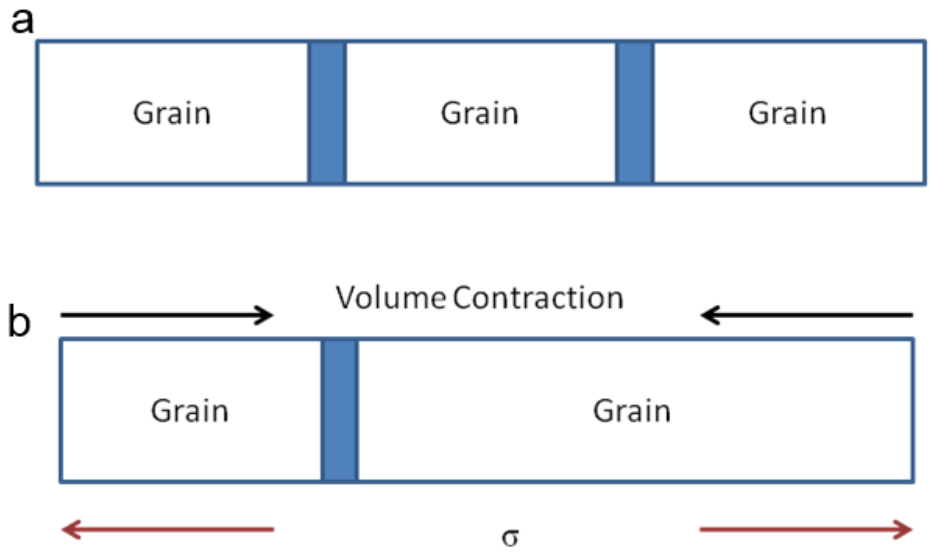


Figure 3.2: Schematic of tensile forces evolved during grain growth: a) initial grain structure of film, b) volume contraction as a result of boundary elimination during grain coalescence and resulting tensile force.

Thompson and Carel provided the first equation for the "densification strain" resulting from grain growth:

$$\varepsilon_d = \Delta a\,((1/d) - (1/d_0)) \qquad (3.1)$$

where $\varepsilon_d$ is the "densification strain", $\Delta a$ is the free volume per unit area of grain boundaries, and d and $d_0$ are the final and initial grain sizes respectively[43]. Additionally in this work, these authors showed that the densification strain can have a sufficient impact on the thermodynamics of the process, that it can place an upper limit on the extent of grain growth.

As has been discussed by Koch[43], the densification strain evolved during grain coarsening can also be extended to the process of recrystallization. The MgO and/or Si products may contain a large density of dislocations. As an increased free volume over the defect-free lattice may be attributed to dislocation defects, the reduction of dislocation density through the process of recrystallization will affect the densification strain in the material. As pointed out by Koch[43], recrystallization will result in a growth of the average grain size of the thin film, and the densification strain during recrystallization may be estimated using a method similar to that developed by Thompson and Carel for grain coarsening. Both the process of grain coarsening and recrystallization will be studied here using the broadening of XRD peaks to monitor the growth of grains within the product films.

### 3.2.3 Geometric Distortion

The possibility exists that geometric distortions may occur in MgO/Si product films formed on planar $SiO_2$ substrates, and these geometric distortions may account for stress relief. SEM and TEM analyses have been used to closely study the geometry of the samples before and after reaction. Several types of disturbances have been found to

occur in thin films as a result of residual stresses, many of which are easy to identify in films of low surface roughness. Hillocking is a type of stress-induced diffusion known to occur in many thin film systems under compression, which is characterized by the growth of whisker-like protrusions from the surface of the film[44]. It has been shown that, during annealing, these protrusion can undergo Ostwald ripening, meaning that the number of these protrusions may decrease with longer annealing times[45]. Sinusoidal buckling of the film can also occur as a result of compressive stress acting on the film[46]. This type of distortion is characterized by the generation of wavy disturbances in the surface profile of the film. Finally, it is entirely possible for the film to undergo cracking or spallation if the residual stress becomes sufficiently large.

### 3.2.4 Vapor Phase Product Formation

Another possibility that will be examined using chemical analysis is the occurrence of a volatile vapor phase as a result of the reaction:

$$Mg(g) + SiO_2 \rightarrow MgO + SiO(g) \qquad (2.9)$$

Although the dominant reaction must be (1.1), the formation of SiO gas from (2.9) can result in relief of compressive stress by reducing the density of the MgO/Si product (the molar ratio of MgO:Si will be altered). Although $p_{SiO}$ as a result of (2.9) is not expected to be very high ($\Delta G°$=14.6 kJ $mol^{-1}$ at 750 °C[20]), compressive stress acting on the MgO product may result in the reaction becoming more favorable. The formation of SiO gas will result in a higher MgO:Si molar ratio that what is expected from (1.1). Thus, chemical analysis by way of quantitative XRF can be used to ascertain whether significant formation of SiO gas occurs during reaction.

## 3.3 Experimental Design

### 3.3.1 Reaction and Annealing of Single Crystal Quartz Substrates

Polished quartz wafers were reacted according to the standard method described in Chapter 2 to form magnesiothermically-reduced product films. Attempts were made initially to use fused silica wafers; however, extensive spalling of the product film was found after reaction at 650-750 °C for ≥ 30 mins. Similar spalling was not found in monocrystalline quartz samples after similar reaction conditions. Polycrystalline quartz was not considered, as the α→β quartz transition, which occurs at 573 °C, is known to introduce complicated thermal stresses in the material[47]. Spalling on reacted fused silica was likely the result of a high coefficient of thermal expansion (CTE) mismatch between the MgO/Si product (average linear CTE calculated to be 10.5 ppm $K^{-1}$ from 25 to 750 °C using a rule of mixtures approximation)[42] and the fused silica substrate (0.5 ppm $K^{-1}$ for 25 to 750 °C)[43]. Attempts were made to cool reacted fused silica from the reaction temperature to room temperature over long periods of time (> 24 hrs), but spalling of the product could not be avoided.

Because the stress state of the product film is a critical property being studied in this work, special consideration must be given to the effect of stresses that evolve as a result of differential thermal expansion between the product film and the $SiO_2$ substrate. These stresses only form during cool down of the reacted wafers from the processing temperature, and are not present during reaction. As the goal of this study is to analyze stress that is a direct result of the conversion of $SiO_2$ to MgO/Si, the interference of thermal expansion mismatch must be minimized. For this reason, z-cut single crystal quartz wafers were selected as substrates for two reasons. First, in a hexagonal crystal

system, the CTE of the crystal can be characterized in two principal directions, those being the direction perpendicular to the principal symmetry axis ($\alpha_{\perp}$) and a direction parallel to the principal symmetry axis ($\alpha_{\parallel}$). Hence, for z-cut quartz, the CTE mismatch strain in the product film will be the same in all directions parallel to the surface. Secondly, $\alpha_{\parallel}$ (15.9 ppm $K^{-1}$)[44] is relatively closely matched to the expected CTE of the MgO/Si composite product (based on a rule of mixtures approximation of a composite of 65 vol.% MgO and 35 vol.% Si) when compared to fused silica, meaning that spalling of the product film was unlikely to occur.

After the initial reaction, samples were annealed to induce stress relaxation without the complicating factor of continued reaction/thickening of the product film. Annealing was carried out at the same temperature as reaction for a given sample in an atmosphere of Mg-gettered ($O_2$-depleted) air. A very low $p_{O2}$ was necessary during such post-reaction annealing so as not to oxidize the Si product. Mg-gettering was accomplished by the method illustrated in Figure 3.3. A 5.5 ft. DOM steel (0.6 max wt.% Mn, 0.04 max wt.% P, 0.05 max wt.% S) tube (1 in. dia.) was clamped and welded shut at one end. 1 g of Mg metal granules was then deposited in the welded end of the tube. This amount of Mg was well in excess of that needed to react all of the $O_2$ present in the final sealed tube (334 mg). A crimp was made roughly in the middle of the tube to prevent Mg granules from crossing to the other end of the tube. The reacted quartz samples were placed in a low-carbon steel boat and slid inward roughly 4-6 in. from the open end of the steel ampoule. The remaining open end was then clamped and welded shut in air.

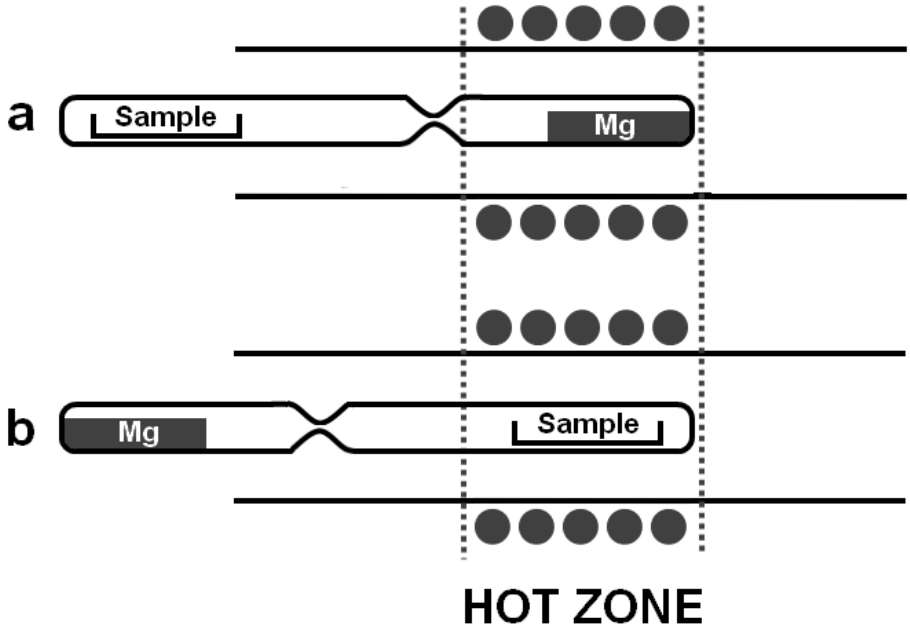


Figure 3.3: Schematic of annealing process under an Mg-gettered, low $p_{O2}$ atmosphere: a) Mg-filled end of the steel ampoule was inserted into the hot zone to melt Mg and reduce the internal $p_{O2}$ by magnesium oxidation, b) Mg-filled end was cooled and the sample-loaded end of the ampoule was thrust into the furnace hot zone for the annealing treatment.

For the first step of annealing, at 750 °C, the tube was placed in a horizontal tube furnace with the Mg-bearing end located at the center of the hot zone and the sample-bearing end located outside of the furnace at room temperature. During this $O_2$ gettering step, melted Mg was reacted with the $O_2$ in the tube to bring the $p_{O2}$ to the equilibrium Mg/MgO partial pressure at 750 °C. At this $p_{O2}$ and temperature, Si oxidation is not favored[20]. During this step, the sample-bearing end of the tube was kept at room temperature, so that Mg gas would condense prior to reaching this area and additional magnesiothermic reduction of the sample would not occur. The gettering step was conducted for 24 hrs, after which the tube was removed from the furnace and allowed to

cool to room temperature. In the second step, the sample-bearing end was thrust into the preheated furnace hot-zone, while the Mg-bearing end was kept far from the hot-zone. This was done to avoid the formation of Mg gas and to allow the sample to be annealed in the $O_2$-depleted inert atmosphere inside of the tube. After annealing, the furnace was turned off and the sample-bearing end of the tube was allowed to cool down to room temperature in roughly 10 hrs. It was found that faster cooling rates resulted in spalling of the product films.

### 3.3.2 X-ray Diffraction Analysis of Product Film Residual Stress

Stress in the MgO/Si product films was characterized using the $\sin^2\psi$ XRD method. This technique quantifies residual strain in a thin film by measuring the dependence of a diffracted peak position on the tilt angle, $\psi$[51]. The MgO {200} peak position, which is the MgO primary peak and the strongest peak in the MgO/Si pattern, was used for this analysis.

In a material with a random distribution of grain orientations and under an applied stress, it has been found that the interplanar spacing for a given diffraction peak, $d_{hkl}$, becomes a function of the angle $\Psi$, which is the angle between the (hkl) plane normal, and the surface normal of the sample[51]. The Bragg equation relates the position of the diffracted peak to that of the interplanar spacing:

$$n\lambda = 2d_{hkl}\sin\theta \tag{3.2}$$

where n is an integer value, $\lambda$ is the wavelength of the incident monochromatic X-ray radiation, and $\theta$ is the Bragg angle. Thus, by tilting the stressed sample (i.e., rotating about the axis $\psi$ in Figure 3.x), a change in the Bragg angle for a given reflection will be

observed, and $d_{hkl}$ can be measured as a function of ψ using the Bragg equation. For this study, a glancing angle modification of the $\sin^2\psi$ method for thin films developed by Ma, et al. has been used[51]:

$$\frac{d_{\alpha\psi} - d_0}{d_O} = \frac{1+\nu}{E}\sigma\cos^2\alpha\sin^2\psi + \frac{1+\nu}{E}\sigma\sin^2\alpha - \frac{2\nu}{E}\sigma \tag{3.3}$$

where $\alpha=\theta_0-\gamma$ ($\theta_0$ is the observed peak for an (hkl) plane at $\psi=0$, and γ is the fixed incident angle), $d_0$ is the lattice spacing of (hkl) when $\psi=0$, $d_{\alpha\gamma}$ is the lattice spacing measured at a given angle α and ψ, E is the Young's modulus, υ is the Poisson's ratio, and σ gives the stress in the film. A schematic of X-ray diffractometer axes is given in Figure 3.4, illustrating the axis about which rotation gives tilt labeled ψ. By plotting $(d_{\alpha\gamma}-d_0)/d_0$ vs. $\sin^2\psi$, the stress, σ, can be found with knowledge of E and υ. For the present work, a Young's modulus of 294 GPa and a Poisson's ratio of 0.186 were used for polycrystalline MgO[52a].

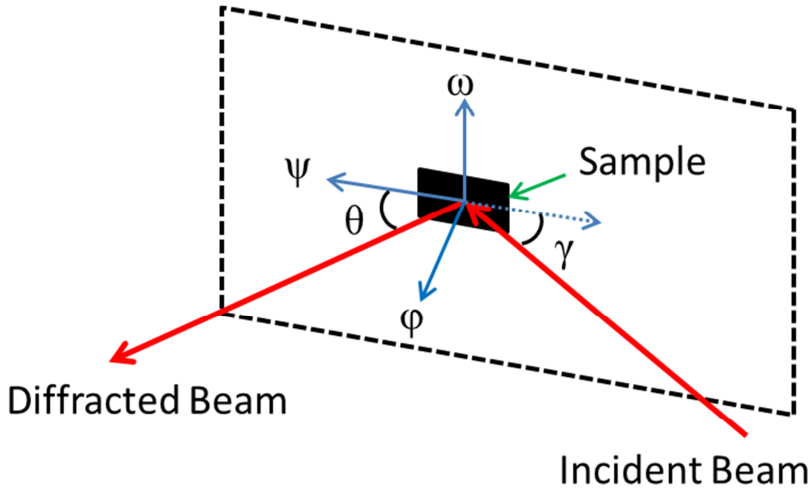


Figure 3.4: Schematic of X-ray diffactometer axes.

To perform diffraction measurements, an X'Pert MRD diffractometer (PANalytical, Alemlo, the Netherlands) was utilized. The diffractometer was configured with a Cu $K_\alpha$ radiation source, with a Cu parabolic mirror in the incident beam path. An incident angle of 0.5° was made with the sample. A 0.09° parallel plate collimator was placed in the diffracted beam path. For stress analysis of annealed product films, measurements were made of the {200} MgO peak at $\psi$ angles of 0°, 5°, 10°, and 15° on two samples for each annealing time for which data was collected. For comparison, a stress measurement was made using the {222} Si peak of a sample reacted at 750 °C for 1 hr.

### 3.3.3 Characterization of Product Film Morphology

SE images were obtained with a LEO 1530 FE-SEM (Carl Zeiss AG, Oberkochen, Germany) at an accelerating voltage of 15 kV. TEM images were acquired with a JEOL 4000EX (JEOL, Tokyo, Japan). To prepare samples for TEM analyses, two samples were glued together with epoxy so that the product films faced each other. The stack was then cured for two minutes. Afterwards, the stack was cut into 1.6 mm slices, which were then embedded in a Cu tube (3 mm OD, 2.2 mm ID) with epoxy. After curing, the tube was cut into 1 mm dia. disks. Each disk was then ground to a thickness of 100 µm, which was followed by dimpling and ion milling to perforation. X-ray fluorescence (XRF) analyses were performed using a MiniPAL 4 XRF (PANalytical, Almelo, the Netherlands) instrument. Weight percentages were calculated from the XRF intensity data using the PANalytical Omnian model.

## 3.4 Results and Discussion

### 3.4.1 Stress Evolution during Annealing

XRD data, shown in Figure 3.5, yielded a residual stress of -5.17 ± 0.14 GPa in the MgO phase and a residual stress of -3.12 ± 0.76 GPa in the Si phase of the product films on samples reacted at 750 °C for 1 hr (error bars indicate standard deviation). This corresponds to a strain of 0.0181 and 0.0175 in the Si and MgO phases respectively. As the strain values for each phase are within 3.3% of each other, an isostrain condition is assumed for these product films. Figure 3.6 illustrates the measured dependence of residual stress in the MgO phase on reaction time at 750 °C. At least some of this residual stress may be attributable to the CTE mismatch between the product film and the underlying quartz substrate. The stress exerted on a film as a result of differential thermal expansion with respect to a substrate is given by:

$$\sigma_f(T) = \frac{(\alpha_s - \alpha_f)(T - T_0)E_f}{1 - \nu_f} \tag{3.4}$$

where $\alpha_s$ and $\alpha_f$ are the CTE values of the substrate and film respectively, $T_0$ is the initial temperature, $E_f$ is the Young's modulus of the film, and $\nu_f$ is the Poisson's ratio of the film[53]. Assuming an isostrain condition, the apparent properties of the MgO/Si composite product required for (3.4) are calculated in Table 3.2 assuming 65 vol.% MgO and 35 vol.% Si and using:

$$E_{MgO/Si} = 0.65E_{MgO} + 0.35E_{Si} \tag{3.5}$$

$$\nu_{MgO/Si} = 0.65\nu_{MgO} + 0.35\nu_{Si}$$

$$\alpha_{MgO/Si} = \frac{0.65E_{MgO}\alpha_{MgO} + 0.35E_{Si}\alpha_{Si}}{0.65E_{MgO} + 0.35E_{Si}}$$

The average linear CTE parallel to the surface of z-oriented quartz is 15.9 ppm $K^{-1}$ (averaged from 298 to 1023 K)[50]. The calculated stress generated as a result of differential thermal expansion is then -1.273 GPa. As this value is well below the measured residual stress from XRD, the remainder is assumed to have resulted from the reaction-induced stress.

Table 3.2: Calculated MgO/Si product film properties.

| | MgO | Si | MgO/Si |
|---|---|---|---|
| Young's Modulus | 294.7 GPa[52a] | 172 GPa[52b] | 252 GPa |
| Poisson's Ratio | 0.186[52a] | 0.25[52c] | 0.21 |
| Coefficient of Thermal Expansion | 13.0 ppm $K^{-1}$[26b] | 2.6 ppm $K^{-1}$[26c] | 10.5 ppm $K^{-1}$[54] |

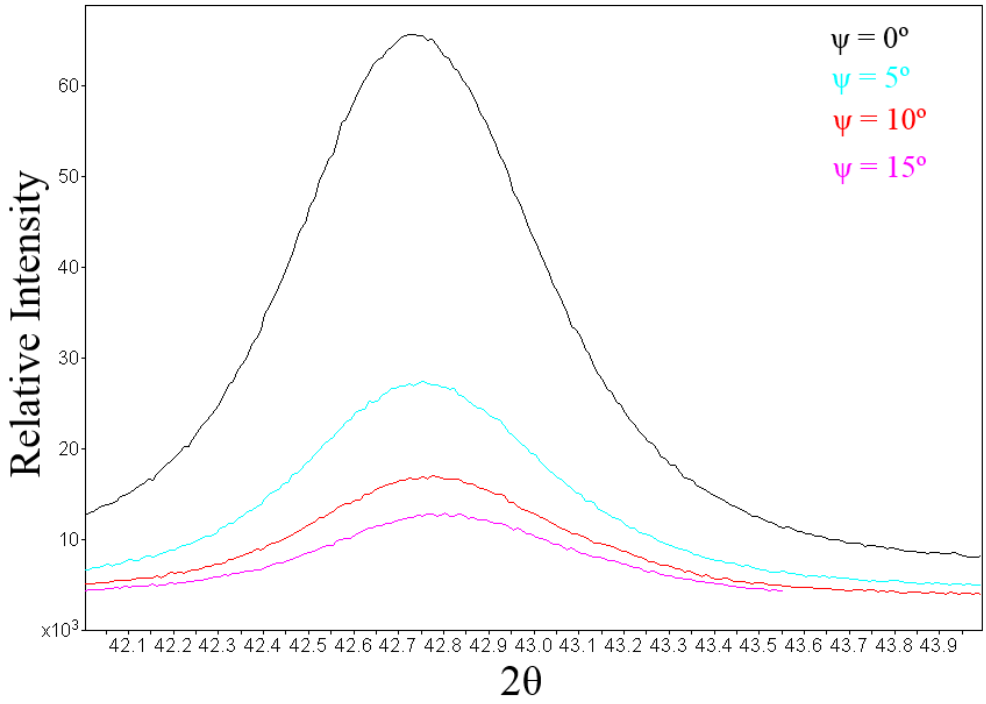


Figure 3.5: XRD residual stress analyses of (Top) MgO and (Bottom) Si phases in a magnesiothermically-reduced product film on quartz generated by reaction at 750 °C for 1 hr.

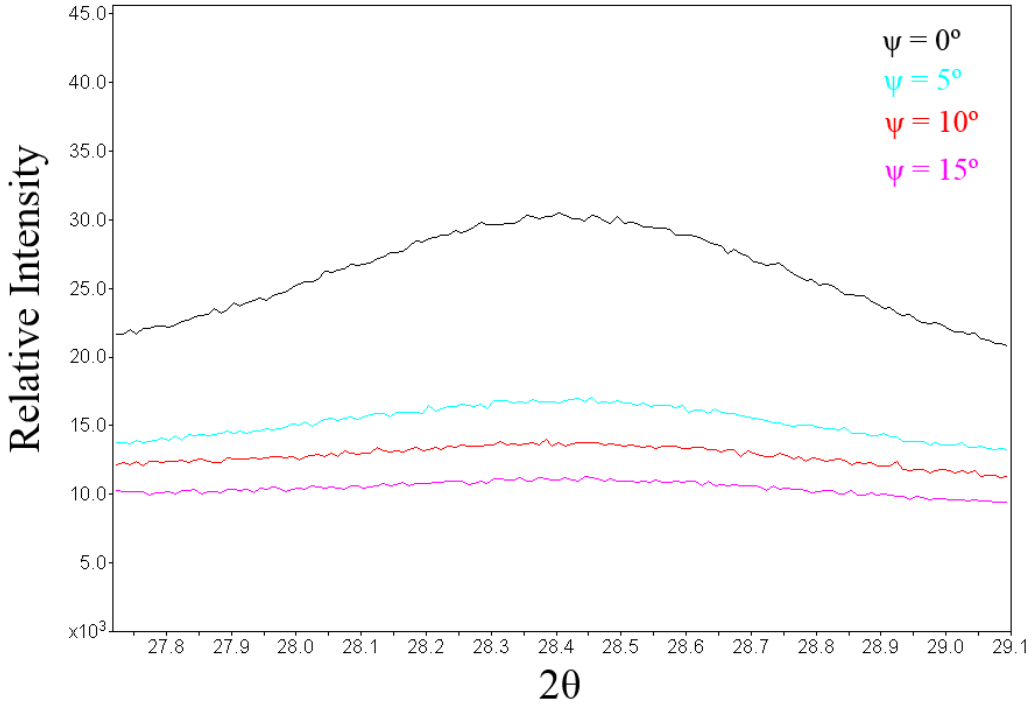


Figure 3.5 continued.

Samples were annealed in a low-$p_{O2}$ atmosphere at 750 °C to induce relaxation in the product films. The results are shown in Figure 3.7. After 2 hrs of annealing, stress is seen to increase from -5.17 GPa (before annealing) to -6.35 GPa. The sudden increase in the residual stress state may be linked to the complete crystallization of the amorphous magnesium silicate product layer that occurs after less than 2 hrs of annealing. $Mg_2SiO_4$ is known to expand upon crystallization[52d]. The constraint of the quartz substrate is expected to impose additional compressive stress on the product film as a result of expansion due to forsterite formation. Gradual stress relief was found to occur during annealing, with a greater reduction in residual stress detected at longer annealing times. However, the stress relaxation rate was found to decrease with annealing time. The

power law fitting of the annealing data is shown in Figure 3.8. The slope of the logarithmic plot of the power law fitting is -0.276. A parabolic plot of the annealing data is shown in Figure 3.9, which demonstrates a roughly parabolic behavior of the residual stress dependence on annealing time.


Figure 3.6: Product film residual stress (MgO phase) measured as a function of reaction time for samples reacted at 750 °C. Error bars indicate standard deviation.

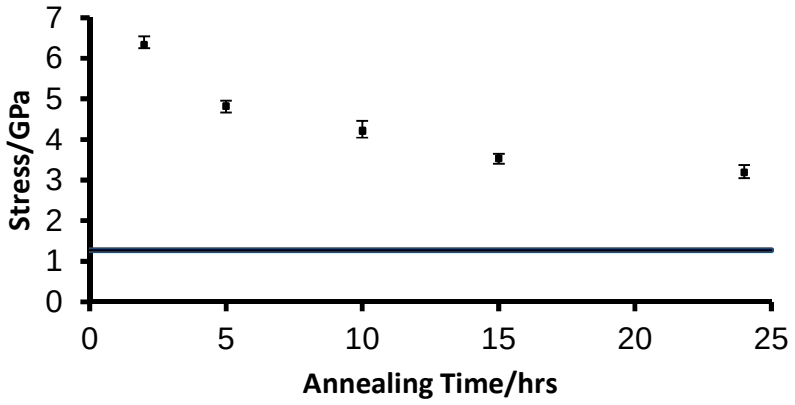


Figure 3.7: Product film residual stress (MgO phase) measured as a function of annealing time for samples reacted at 750 °C for 1 hr and annealed at 750 °C. Blue line indicates expected residual stress as a result of differential thermal expansion. Error bars indicate standard deviation.

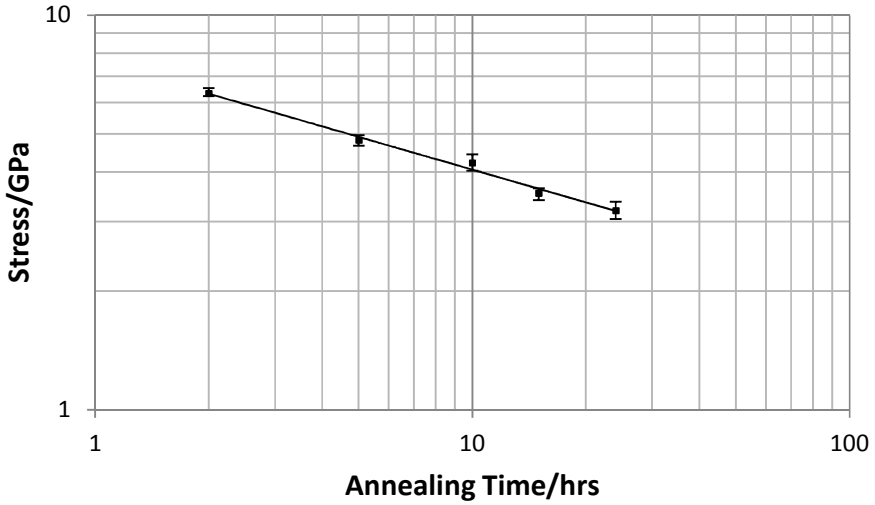


Figure 3.8: Logarithmic scale plot and power law fitting of product film residual stress (MgO phase) measured as a function of annealing time for samples reacted at 750 °C for 1 hr and annealed at 750 °C. Error bars indicate standard deviation.

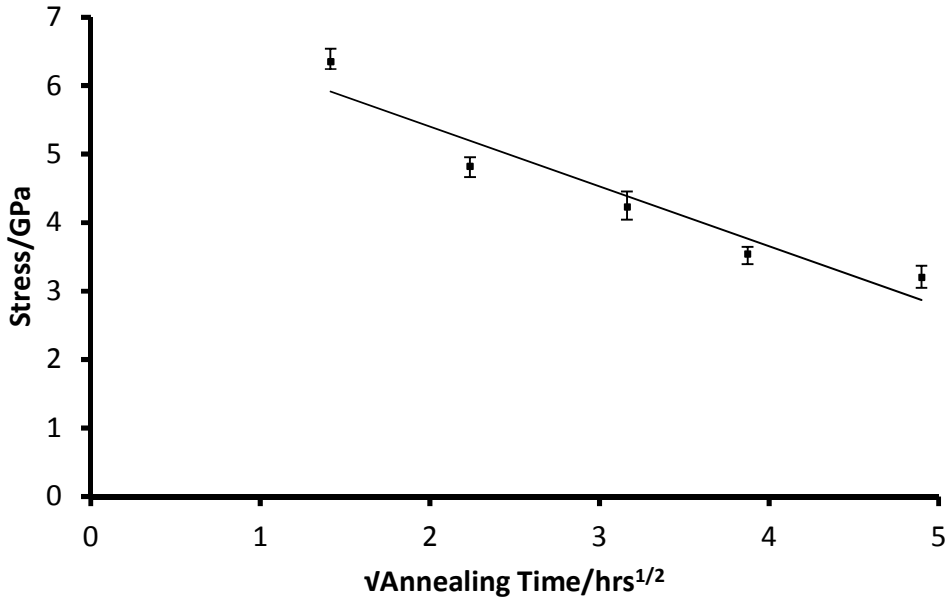


Figure 3.9: Parabolic plot of product film residual stress (MgO phase) measured as a function of annealing time for samples reacted at 750 °C for 1 hr and annealed at 750 °C. Error bars indicate standard deviation. $R^2$ of trendline was 0.9165.

### 3.4.2 TEM Cross-Sectional Analysis

TEM cross-sections revealed two major changes in the product films after annealing. The first was that the inner magnesium silicate containing layer had completely crystallized into forsterite ($Mg_2SiO_4$). SAED analysis of this layer revealed that it was composed of a two-phase mixture of forsterite and Si (see Chapter 2). The lack of evidence for quartz or periclase phases in this layer after crystallization implied that the initial composition of the amorphous silicate must have been close to $Mg_2SiO_4$.

The second major change in the product film occurred at the external surface, where it was found that a rough polycrystalline layer of MgO particles had formed (Figure 3.10a,b). This is evidenced by top-down SEM, where a high density of particles can be seen on the external surface of the sample after annealing (Figure 3.10c,d). The thickness of this MgO overlayer was found to follow a parabolic growth rate as a function of annealing time at 750 °C (Figure 3.11, 3.12). The power law fitting of the overlayer growth data is shown in Figure 3.13. The slope of the logarithmic plot of the power law fitting is 0.361. This corresponds closely to the overlayer growth rate predicted from the measured residual stresses in the product film. As demonstrated in Appendix B, if the product film is considered to deform elastically, then the power law fitting of the overlayer growth rate is predicted to have a logarithmic slope of 0.366. A linear relationship was found between residual stress and overlayer thickness, implying a correlation between overlayer growth and residual stress. Additional MgO overlayers are shown in Figure 3.14.

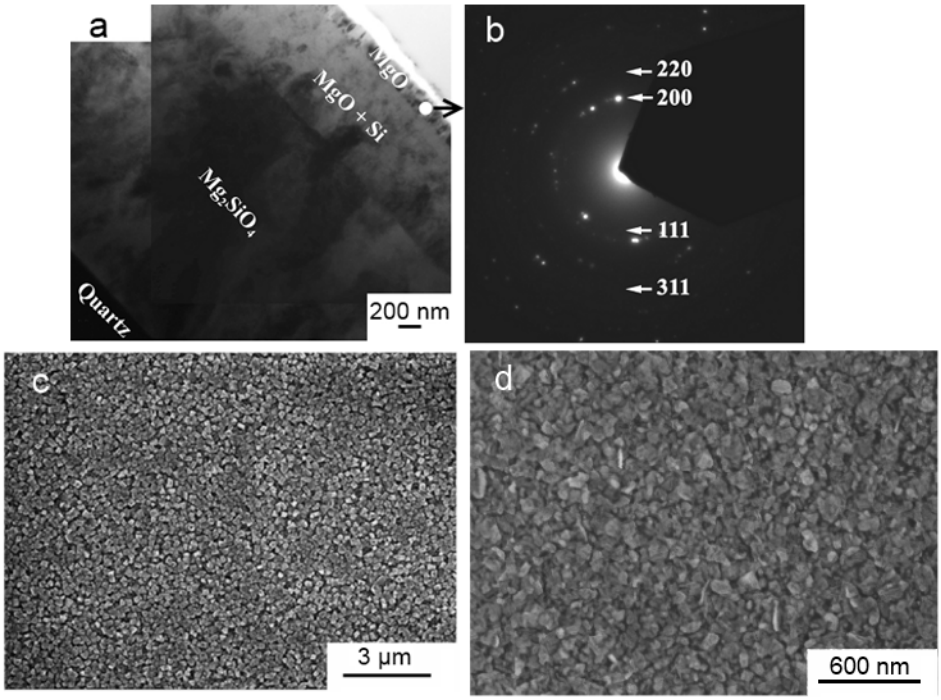


Figure 3.10: MgO overlayer growth on Mg(g)/$SiO_2$ reduced quartz product films after reaction for 1 hr at 750 °C and annealing for 1 hr at 750 °C: a) cross-sectional TE image, b) SAED analysis of surface MgO layer, and c) top-down SE image of MgO overlayer film. (TE images provided by Dr. Ye Cai.)

Two possibilities can be proposed for the appearance of an MgO overlayer on an annealed sample: 1) stress-induced migration of MgO to the external surface of the product film occurs, or 2) Si is removed through a volatile species (such as SiO), which then leaves behind a MgO-rich layer. To explore the possible formation of a volatile product during Mg(g)/$SiO_2$ reduction, magnesiothermically-reduced silica powder was probed via XRF analyses. Silica diatomaceous earth powder was chosen for this experiment, as the high surface area of this powder facilitated rapid and thorough reaction with Mg gas. Unreacted $SiO_2$ would render the results of this experiment invalid. 1 g of $SiO_2$ diatomaceous earth powder was reacted with Mg vapor from an $Mg_2Si$ gas source

over a period of 72 hrs at 750 °C. After reaction, it was found that the weight of the powder had increased to 1.80 g (expected weight after full conversion of pure $SiO_2$ is 1.81 g). From the reaction stoichiometry, the product was expected to have an MgO:Si molar ratio of 2:1. The product would then expectedly be composed of 25.8 wt.% Si and 74.2 wt.% Mg (metals basis). The measured wt.% of Si was 24.9%, indicating that a volatile product was likely not forming during this reaction.

Based on these results, stress-induced migration of MgO is the apparent cause of MgO overlayer growth. If it is assumed that both MgO and Si phases are under the same residual strain (isostrain condition), then by necessity of possessing a higher elastic modulus, the MgO grains will carry a greater fraction of the residual stress. XRD measurements carried out on the Si {222} peak determined there to be a residual stress of $-3.12 \pm 0.76$ GPa in this phase. This corresponds to a strain in Si of 0.0181, which is close to the measured strain in MgO of 0.0175, validating the isostrain assumption. As a result, a higher driving force for stress-induced migration may exist in the MgO phase than in the Si phase. The preference for MgO relocation to the surface may be a result of the ease of sliding of fine (nanocrystalline) MgO grains. Superplasticity and grain boundary sliding in nanocrystalline MgO have been reported by a number of authors[55].

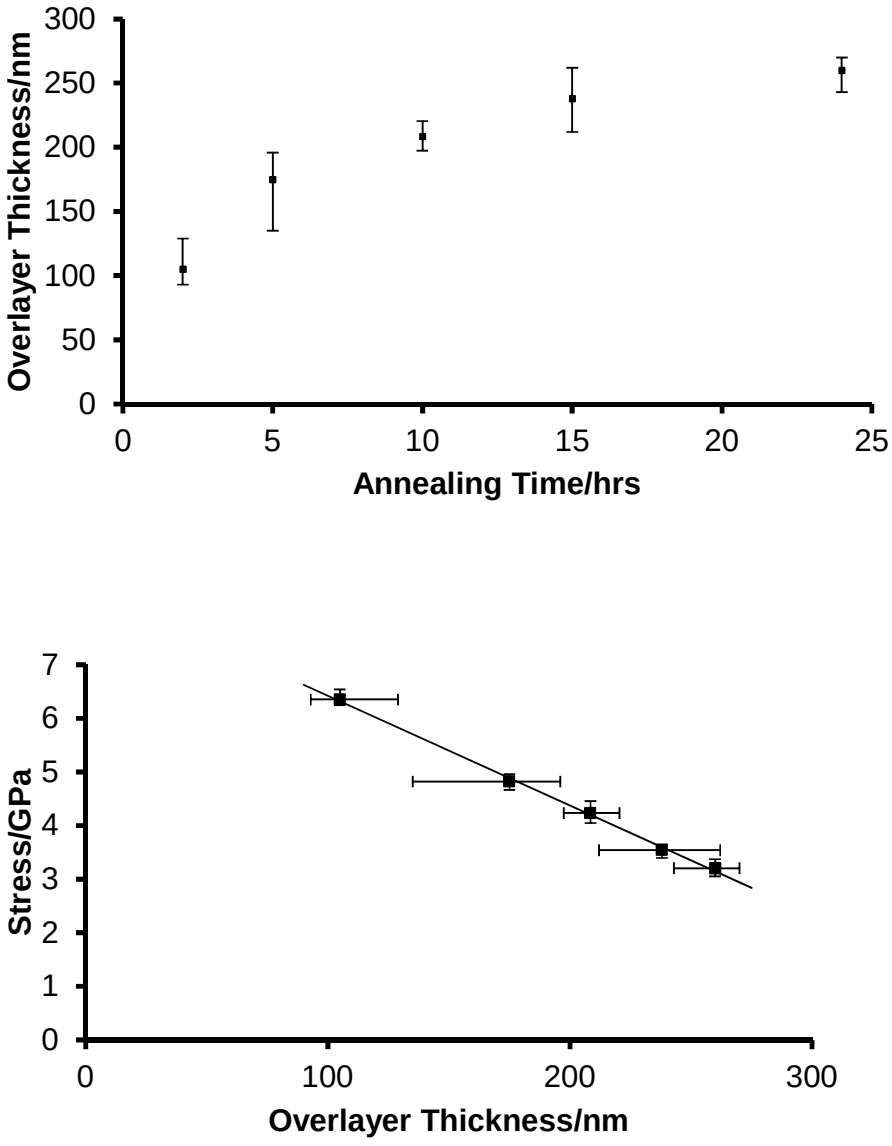


Figure 3.11: (Top) MgO overlayer thickness measured as a function of annealing time at 750 °C (error bars indicate full range of measured data), and (Bottom) observed residual stress in the product film (MgO phase) as a function of observed MgO overlayer thickness (horizontal error bars indicate full range of measured data, vertical error bars indicate standard deviation).

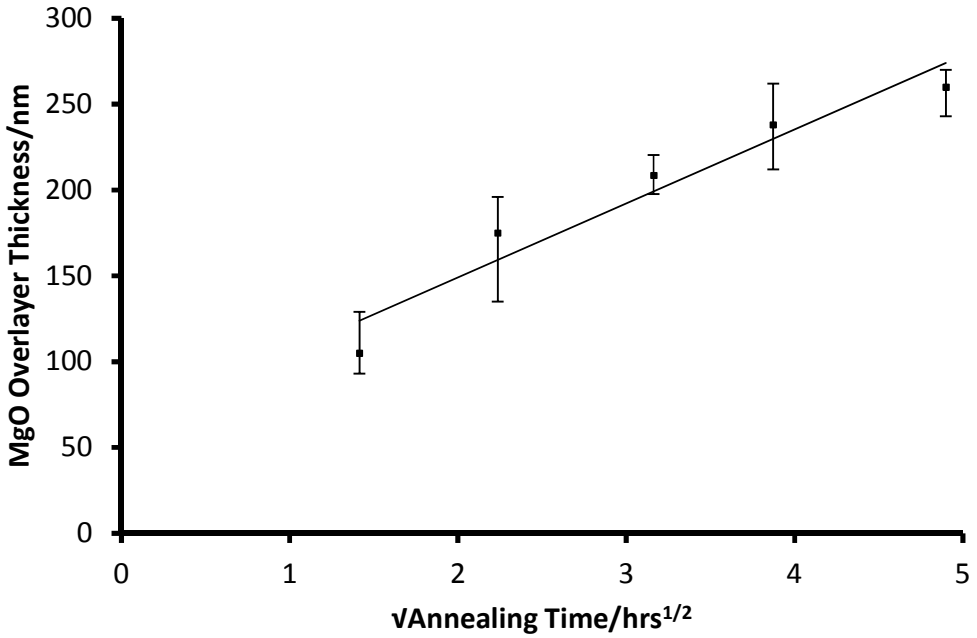


Figure 3.12: Parabolic plot of MgO overlayer thickness measured as a function of annealing time at 750 °C. Error bars indicate full range of data. $R^2$ of trendline was 0.9353

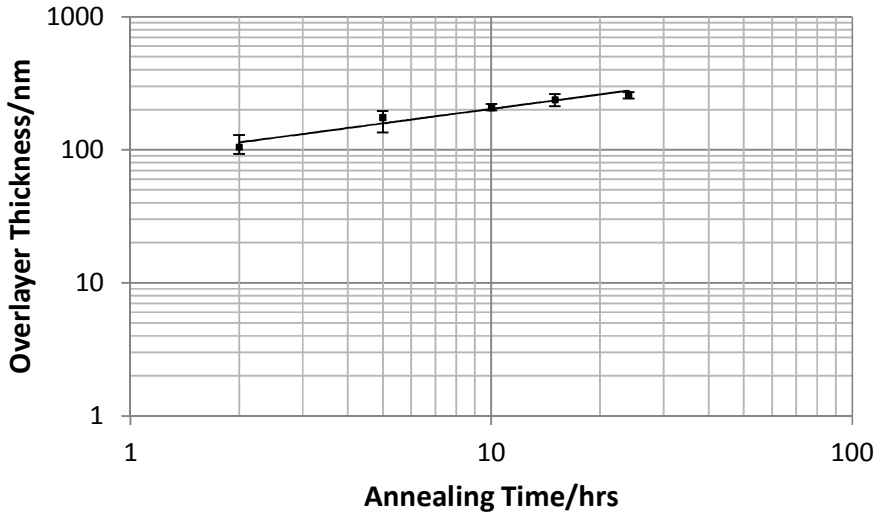


Figure 3.13: Logarithmic scale plot and power law fitting of MgO overlayer thickness measured as a function of annealing time at 750 °C. Error bars indicate full range of data.

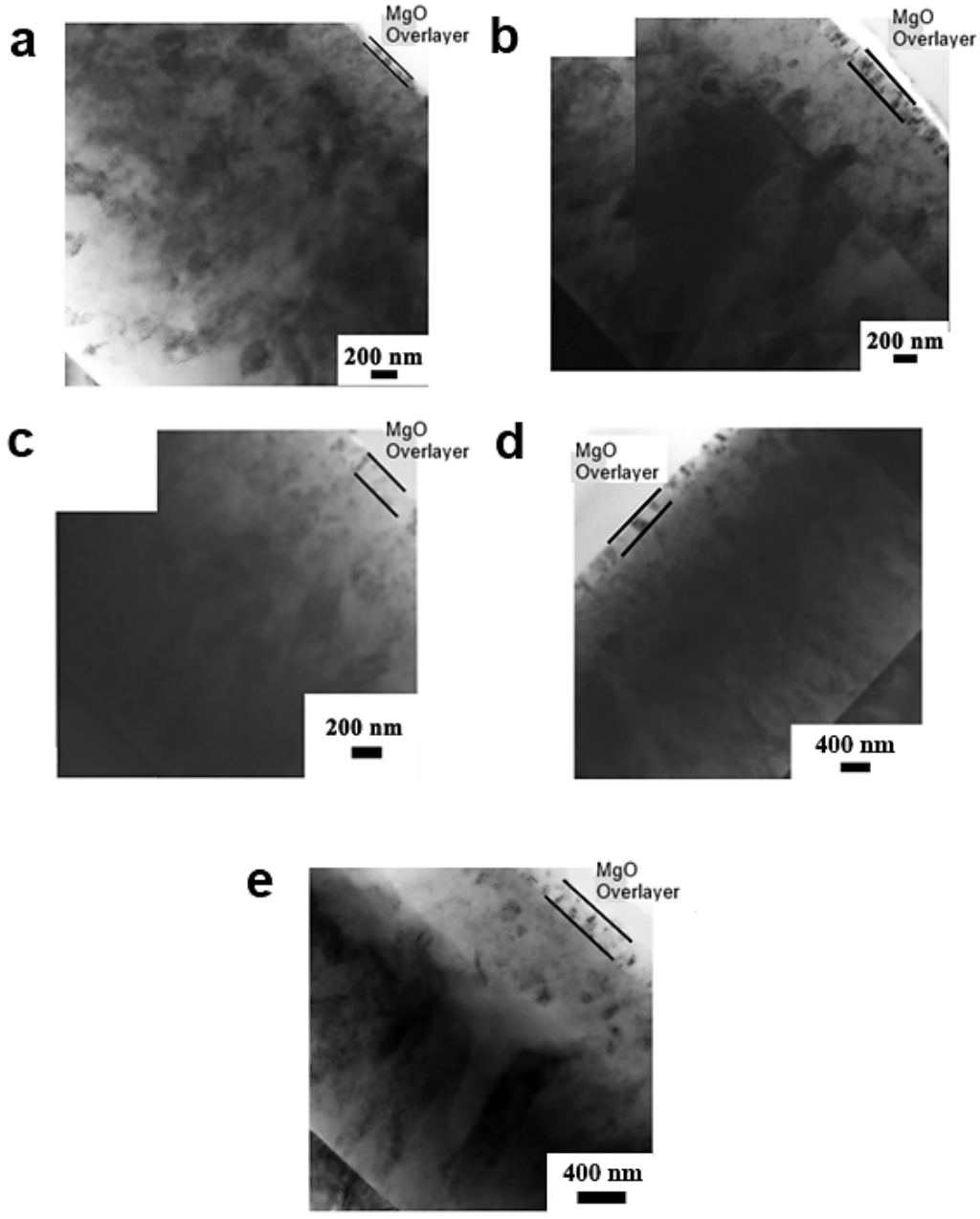


Figure 3.14: TE cross-sections demonstrating MgO overlayer growth as a function of annealing time at 750 °C on quartz wafers reacted at 750 °C for 1 hr: a) 2 hr annealing, b) 5 hr annealing, c) 10 hr annealing, d) 15 hr annealing, e) 24 hr annealing.

### 3.4.3 Alternative Explanations

Although a correlation can be made between stress and MgO overlayer growth in magnesiothermically-reduced product films, other possibilities proposed earlier have yet to be eliminated. The elimination of these possibilities is discussed here.

As discussed previously, compressive residual stress in the product film may generate geometric distortions, such as hillocks or buckles. As seen in Figure 3.6, the surfaces of the annealed samples were found to be dominated by nodular MgO particles, with no whisker-like hillock protrusions being detectable. AFM profiles of the product films after annealing show no buckling of the product film (Figure. 3.15). In addition, no cracking was found in the film by SEM.

Grain coarsening through the course of annealing was evaluated using Scherrer analysis and the FWHM of the MgO and Si primary peaks. Only a marginal change in grain size was found to occur during annealing (Table 3.3). MgO/Si grain/interphase boundaries likely do not possess a high mobility due to the dissimilarity of MgO and Si phases. The marginal growth in grain size cannot be used to account for the substantial reduction in residual stress that is measured after annealing.

Table 3.3: Effect of annealing on grain size in MgO/Si product films. Error bars indicate standard deviation.

| | Grain Size Before Annealing (nm) | Grain Size After 24 hrs of Annealing (nm) |
|---|---|---|
| MgO | 36.3 ± 2.1 | 37.2 ± 2.1 |
| Si | 17.6 ± 1.7 | 20.4 ± 1.9 |

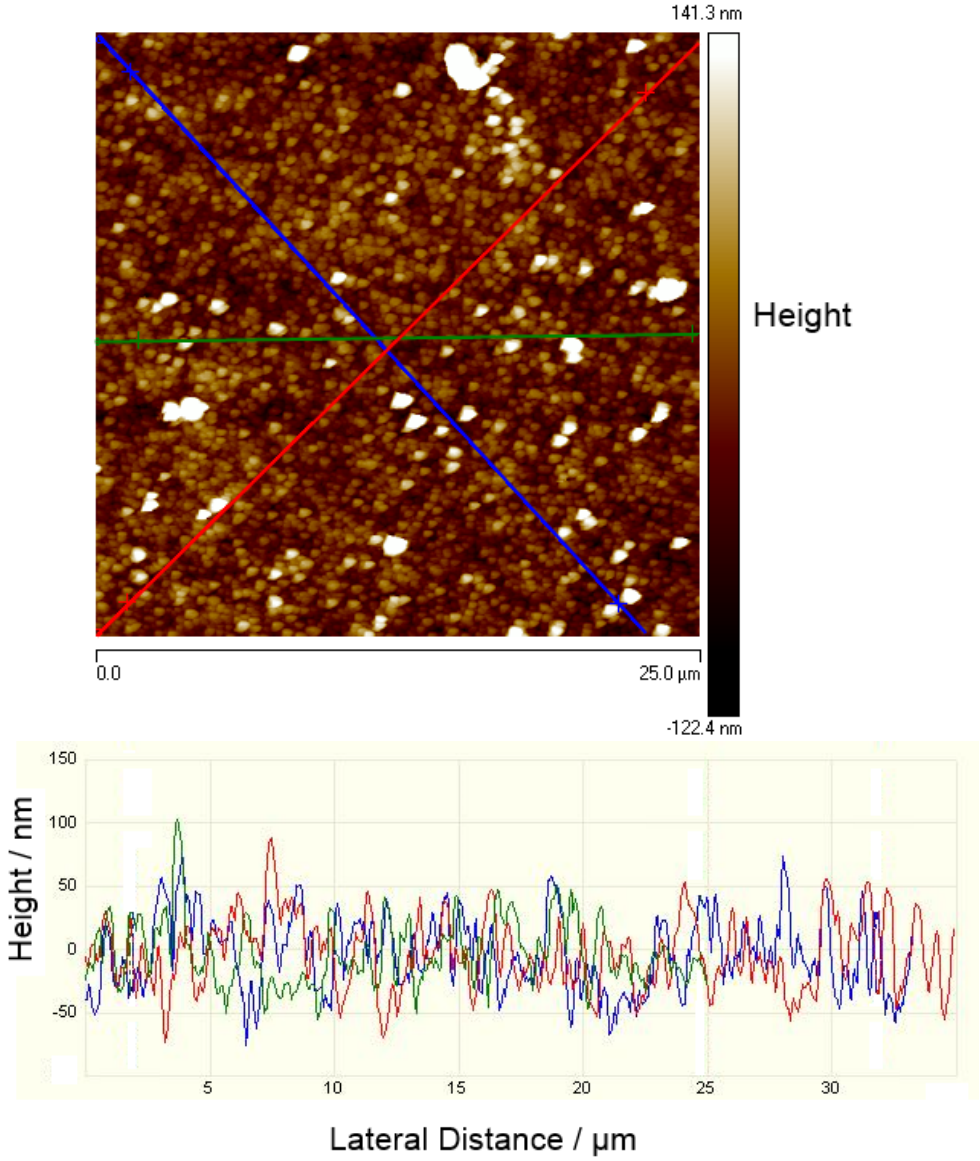


Figure 3.15: AFM analysis of a product film on a quartz sample magnesiothermically-reduced at 750 °C for 1 hr followed by annealing at 750 °C for 24 hrs: (Top) Top-down image, (Bottom) surface height profiles along colored lines shown in (top). (Provided by Brandon Goodwin)

### 3.5 Summary

A significant evolution of residual stress was found to occur in MgO/Si product films on magnesiothermically-reacted quartz (> 5 GPa in the MgO phase) at 750 °C. The residual stress was appreciably higher than what could be attributed to differential thermal expansion between the MgO/Si product film and the quartz substrate. This stress is attributed to being the result of the volume expansion induced upon the conversion of 1 mole of $SiO_2$ to 2 moles of MgO and 1 mole of Si during reaction. Upon post-reaction annealing of samples at 750 °C, stress relaxation was found to occur in the product films, along with the growth of a rough nanocrystalline overlayer of MgO. Stress relaxation and MgO overlayer thickening were found to occur at similar rates, strongly suggesting a correlation. Other mechanisms of stress relaxation were not observed, implying that stress-induced migration of MgO to the external surface of the product film was responsible for the observed stress relief.

# CHAPTER 4:

# CARBONIZATION OF SILICON DIATOMACEOUS EARTH TEMPLATES AND APPLICATIONS

## 4.1 Introduction

Shape preserving inorganic conversion reactions, such as $Mg(g)/SiO_2$ reduction, offer not merely a means to control the chemistry of a template, but in many cases, a means to tailor the pore size distribution of the product structure of a reacted template. For example, the *Aulacoseira* diatom frustule (DE) natively possesses large macropores on the length scales of microns to hundreds of nanometers (Figure 4.1). When subjected to $Mg(g)/SiO_2$ reduction, the *Aulacoseira* frustule structure becomes composed of an interwoven two-phase composite of MgO and Si, with a surface area and pore size distribution closely similar to that of the starting *Aulacoseira* template[56a]. Selective etching of the MgO component then results in an increase in surface area and mesopore volume, with the pore volume increase primarily occurring in the size range corresponding to the grain size of the MgO phase. By using the reaction temperature to control grain size in the product structure, it has been found that significant pore volume enhancements can be made in the mesopore to macropore ranges, with corresponding enhancements in specific surface area (SSA).

A logical question may then be asked: if on top of meso- and macropore enhancements, can a means be developed to increase microporosity in a reacted structure? One way to answer this question is to apply additional processing to the porous Si replicas that results in the formation of microporosity without adversely

affecting meso-/macroporosity. Work in this chapter builds upon previous work in the development of a shape-preserving reactive conversion route to convert magnesiothermically-produced Si diatomaceous earth replicas (SiDE) into very high surface area, highly microporous C replicas[56]. This technique utilizes a two-step procedure of 1) carburizing SiDE to form β-SiC replicas, and 2) selectively etching Si from the β-SiC product structure via high temperature chlorination to form highly microporous C replicas according to the reaction:

$$SiC + 2Cl_2(g) \rightarrow C + SiCl_4(g) \quad (4.1)$$

A large volume of micropores is introduced during this reaction due to the selective removal of individual Si atoms from the SiC lattice, which leads to a large SSA enhancement of the C diatomaceous earth replicas (CDE) over the DE templates. In addition, the microporosity is additive to the previously-existing macropores (natural features of the diatom template and in some cases a product of magnesiothermic reduction) and mesopores (a product of the magnesiothermic reduction process found in SiDE), resulting in a highly-porous product structure with a hierarchical pore distribution across all pore size ranges.

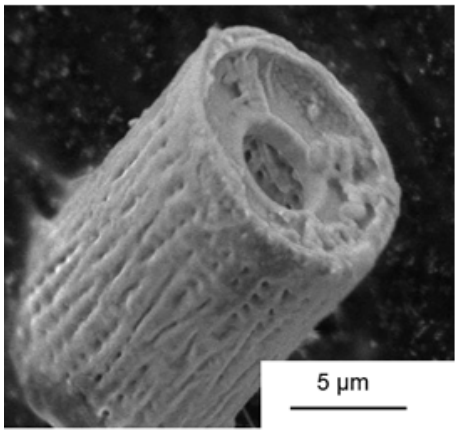


Figure 4.1: *Aulacoseira* $SiO_2$ diatom frustule particle.

A C product structure can be particularly useful, as carbon is widely studied as a substrate for a number of inorganic and organic catalysts[57]. The hierarchically porous CDE are expected to provide performance advantages over other porous C substrates lacking this quality (e.g. carbon black, activated carbons), because of the combined benefits offered by macropores, which offer high mass transport rates, and meso-/micropores, which offer high surface areas for loading of catalyst sites[58]. The goal of this chapter is to demonstrate the synthesis and characterization of hierarchically porous CDE, and, in particular, demonstrate that the surface of these structures can be tailored with both organic and inorganic modifications for catalytic applications. The relative performance of the catalyst-loaded CDE has also been evaluated to demonstrate the advantages of these biogenic materials as catalyst substrates.

Two different schemes for loading technologically important catalysts into CDE powders were developed and the performance of the catalyst-loaded product powders was tested. For an inorganic catalyst, Pt nanoparticles were embedded in the CDE and

applied to glassy carbon working electrodes to test the electrocatalytic activity of the Pt-loaded CDE with respect to the oxygen reduction reaction (ORR). ORR occurs at the cathode of proton exchange membrane fuel cells (PEMFC)[59]. PEMFCs have received a significant amount of attention in the field of energy conversion[60]. The Pt catalyst necessary to facilitate this reaction requires a catalyst support to disperse the catalyst particles and prevent sintering (and therefore loss of surface area) which can occur at the operating temperatures of these devices[60]. Carbon materials, such as carbon blacks, CNTs, mesoporous carbons, and carbon xerogels have been studied as Pt catalyst supports because of their relative chemical stability in a wide range of environments[60].

For organic/biomolecular catalyst loading, a model enzyme, glucose oxidase (GOx), which catalyzes the decomposition of glucose into hydrogen peroxide[61], was immobilized on CDE and tested in a flow-through reactor. A catalyst support is required in such systems to maintain separation of the enzyme from the product-containing solution, so that the enzyme may be continuously reused, and evidence has been found to demonstrate that biocatalyst stability is often increased by immobilizing the enzyme on a solid surface[62]. Several types of materials have been tested as enzyme supports, such as mesoporous silica cellular foams, carbon blacks, and activated carbons[62]. While these supports typically boast high mesoporosity for accommodating relatively high levels of immobilized enzyme, they often do not possess the high degree of macroporosity found in the hierarchically-porous CDE. The macropores of the CDE are expected to enhance performance in a flow-through setup, as rapid fluid flow through these pores may be accomplished with a relatively small pressure drop across the enzyme-loaded CDE powder compact. The enzyme glucose oxidase (GOx) was used in this work to determine

the efficacy of surface-modified CDE as a support for enzyme biocatalysts. GOx is capable of catalyzing the decomposition of glucose to $H_2O_2$ and D-glucono-δ-lactone[61]. GOx was chosen as it is a commonly-used model enzyme system, for which the catalyst kinetics are well characterized[61]. In addition, the compound is known to be reasonably stable and can be readily obtained in high purity[61].

Furthermore, in this chapter, CDE is used as a template for the fabrication of high SSA Au-bearing diatom replicas. Diatom replicas of gold and other precious metals have been studied for their use in catalysis[63a], SERS[63b], and photonics applications[63c]. Thus far however, the surface areas of these Au diatom replicas (AuDE) have been modest. Even when electrolessly depositing Au on high surface area SiDE produced through magnesiothermic reduction (SSA=541 $m^2\ g^{-1}$), the SSA of the Au replica was greatly reduced (SSA=10.1 $m^2\ g^{-1}$)[64]. In this chapter, it is proposed that surface-oxidized CDE (SSA=793 $m^2\ g^{-1}$) may be used as a template to produce high SSA Au-bearing diatom replicas (AuDE).

As with CDE, the AuDE diatom frustule replicas are expected to show performance advantages as catalyst supports due to the hierarchical nature of the structure's porosity. This is particularly true in flow-through applications, wherein macroporosity can allow for enhanced fluid flow through a powder compact. As with CDE, for this work the AuDE samples were loaded with GOx and the catalytic activity of the samples were tested with respect to glucose decomposition in a flow-through reactor.

## 4.2 Experimental Design

### 4.2.1 Synthesis of Enhanced Surface Area, Microporous Carbon Diatom Replicas

Magnesiothermically-generated SiDE were used as a starting platform for the generation of high surface area, microporous CDE. The Mg(g)/$SiO_2$ reduction process as described in previous chapters was applied to DE. Magnesiothermic processing was carried out at 900 °C for 1.5 hrs, using Mg metal as a gas source. Into an 8 in. long, 1 in. diameter low C steel ampoule with one end welded closed, 600 mg of Mg was loaded into the bottom of the ampoule, and a crimp was made in the ampoule roughly 1in. from the sealed end. A powder bed of 600 mg of $SiO_2$ diatomaceous earth powder (PoolTime DE, Chemtura, Lawrenceville, GA) was loaded into a 4 in. Fe boat and then inserted into the ampoule. The open end of the ampoule was then sealed. The ampoules were placed in a preheated horizontal tube furnace and processed at 900 °C for 1.5 hrs. After such processing, the ampoule was promptly removed from the furnace and cooled in air to room temperature.

When the diatom powder-loaded Fe boats were removed from the ampoules, an apparent gradient in products was seen across the powder bed, defined by distance along the powder bed from the Mg-bearing end of the ampoule. Closest to the Mg-bearing end of the ampoule, a blue product powder was seen, which in previous work has been identified as $Mg_2Si$/MgO diatom replica powder[10]. Adjacent to the blue product and further away from the Mg-bearing end of the ampoule, a black product was found, which was previously identified as MgO/Si diatom replica powder[10]. Beyond the black product existed a brown product, which had been identified previously as $Mg_2SiO_4$/Si diatom replica powder[10]. Occasionally, white unreacted $SiO_2$ powder was found at the end of the ampoule, farthest away from the Mg-bearing end.

The black MgO/Si powder was collected from the product powder bed, and the other products were disposed. To dissolve the MgO phase from the product powder and form a Si-only powder, the MgO/Si product was subject to etching in 1N HCl for 3 hrs with gentle stirring. Afterwards, the powder was thoroughly washed with water and methanol. The resultant powder was brown in color, and was determined by XRD to be composed only of a Si phase.

The 900 °C-generated SiDE were then used as a starting template for the generation of CDE via a two-step process. In the first step, SiDE was carburized to form β-SiC replica powder. A powder bed of 150 mg of SiDE was loaded onto an MgO boat, and placed in a horizontal tube furnace. The tube furnace was sealed at both ends, except for an inlet and outlet line for flow-through processing gases. Initially, the furnace was purged with flowing Ar (450 $cm^3$ $min^{-1}$) for 2 hrs at room temperature. The temperature was raised to 950 °C (5 °C $min^{-1}$ ramp rate) while maintaining Ar flow. Once the 950 °C temperature was reached, $CH_4$ was applied in an Ar carrier gas (10% $CH_4$) at a flow rate of 200 $cm^3$ $min^{-1}$ for 2.5 hrs. During this step, a thin C layer was deposited via pyrolysis of $CH_4$ on the surfaces of SiDE. Although higher surface area SiDE could be attained with a lower processing temperature, 900 °C-generated SiDE was used, as the pores needed to be large enough for rapid infiltration of $CH_4$ gas. After $CH_4$ treatment, pure Ar flow was restored and the sample was annealed at 1200 °C for 12 hrs to react the deposited C layer with the underlying SiDE. This processing step was shape-preserving and results in β-SiC replica powder.

The second part of the carbon conversion process entailed the selective etching of Si from the β-SiC product powder to form microporous CDE. An $Al_2O_3$ boat was loaded

with a 600 mg powder bed of β-SiC diatom frustule replica powder. This boat was then inserted into a horizontal tube furnace, which was then purged with Ar gas for 2 hrs (450 $cm^3 min^{-1}$ flow rate). The temperature was raised to 950 °C (5 °C $min^{-1}$ ramp rate) and the Ar flow was replaced with $Cl_2$ gas (450 $cm^3$ $min^{-1}$ flow rate) for 2 hrs. The resultant powder was then treated in flowing $H_2$ gas at room temperature for 1.5 hrs to desorb residual $Cl_2$ present on the surface of the as-treated CDE.

### 4.2.2 Loading of C Diatom Replica Powder with Pt Nanoparticle Catalysts

A gas impregnation method was employed to deposit Pt nanoparticles into the pores of CDE, as well as two C control materials, through the sublimation of $PtCl_2$ in the presence of CO gas according to the reaction[65]:

$$PtCl_2 (s) + 2CO (g) \rightarrow Pt(CO)_2Cl_2 (g) \quad (4.2)$$

An $Al_2O_3$ boat was loaded with a powder bed of a varied amount of $PtCl_2$ (98%, Alfa Aesar, Ward Hill, MA) powder (50-450 mg). The amount of $PtCl_2$ available in the boat during reaction was used to control the extent of Pt-loading. The $PtCl_2$ powder bed was covered with three layers of $Al_2O_3$ cloth (Zicar Zirconia, Florida, NY), and a powder bed of 200 mg of CDE was deposited over the cloth. The boat was then loaded into a closed horizontal tube furnace, which was then purged with Ar for 2 hrs at room temperature. After purging, the furnace temperature was raised to 230 °C (5 °C $min^{-1}$ ramp rate), and flowing CO gas was applied (450 $cm^3$ $min^{-1}$ flow rate). This treatment was conducted for 30 mins, during which, through vapor infiltration, $Pt(CO)_2Cl_2$ particles were deposited into the pores of the CDE sample. Afterwards, CO flow was terminated for Ar flow, and the system was cooled to room temperature. The Pt-infliltrated CDE was collected from

the boat and placed in another $Al_2O_3$ boat. This boat was re-inserted into the horizontal tube furnace, which was purged with Ar for 2 hrs and then raised to 300 °C. At this temperature, flowing $H_2$ gas was applied to completely reduce the deposited Pt-bearing particles within the CDE from the chlorine-containing Pt compound. $H_2$ gas treatment was carried out for 1 hr. In addition to CDE, Pt was loaded into Vulcan XC72R carbon black (Cabot Corporation, Boston, MA) and SiC-derived C microparticles (8.7 µm average diameter) generated from the chlorination method described in section 4.2.1. These additional C samples were used as controls in catalytic testing.

### 4.2.3 Electrocatalytic Testing of Pt-Loaded C Diatom Frustule Replicas

To test the electocatalytic activity of Pt loaded into the three porous C samples, Pt-loaded CDE, Vulcan C, and SiC-derived C were deposited from a Nafion (Nafion NR50, Aldrich, St. Louis, MO) solution onto glassy carbon working electrodes. For each sample, the electrodes were deposited with Pt-loaded C such that for each electrode 0.1 mg $cm^{-1}$ Pt was deposited. The performance of these electrodes with respect to the oxygen reduction reaction (ORR) was tested by the rotating disk electrode (RDE) method, with the electrodes submerged in an oxygen-saturated $H_2SO_4$ (0.5 M) aqueous solution[66].

### 4.2.4 Acidic Surface Modification of CDE for Enzyme Biocatalyst Loading

CDE was treated in 2.6M $HNO_3$ (100 mg CDE per 250 ml bath) at 75 ºC in reflux to generate carboxylic acid surface sites necessary to bind enzymes. Afterwards, thorough washing of the oxidized CDE ($CDE_{ox}$) was performed, followed by drying at 60

°C overnight. $HNO_3$ oxidation was performed for times up to 72 hrs to determine the effect of acid oxidation time on surface carboxylate loading.

As it was found that long acid oxidation times led to disintegration of the CDE structure, a method of dendritic amplification of surface carboxylates was devised to allow for further increases in surface carboxylate loading than what was achievable by acid oxidation. This method was based partly upon a method previously designed to amplify surface hydroxyl groups on oxides[67]. In the devised method, a dendrimer coating composed of alternating layers of polyfunctional amine and acrylate bearing molecules was grown on the $CDE_{ox}$ surface as demonstrated in Figure 4.2. In Step 1, molecules with three primary amines, tris(2-aminoethyl)amine, were cross-linked with surface carboxylates on CDE. After application to the C surface, the polyamine presents two primary amines at each successfully joined surface carboxylate. Each primary amine was then reacted through Michael addition with a polyacrylate, dipentaerythritol penta/hexa-acrylate, to introduce 4-5 acrylate groups at each available primary amine on the surface (Step 2). Finally, through the same reaction, exposed acrylate groups were reacted with an amine-terminated polyacrylic acid which possessed a large number of carboxylic acid functional groups (Step 3). Through this method, a dendrimer that begins at a single surface carboxylate site and terminates with multiple polyacrylic acid molecules, each possessing multiple carboxylic acid functional groups, was generated to amplify surface carboxylate loading.

The specifics of this method were as follows. Initially, 20 mg of a 48 hr $HNO_3$-oxidized CDE specimen ($CDE_{48hr/ox}$) was incubated in an aqueous MES buffer (100 mM, pH 5.85) with 4 mg of 1-ethyl-3-(3-dimethylaminopropyl)carbodiimide (EDC) (Alfa

Aesar, Ward Hill, MA) and 12 mg of sulfo-N-hydroxysuccinimide (SNHS) (Alfa Aesar, Ward Hill, MA) with gentle rotation. After 2 hrs of incubation, 14 µl of 2-mercaptoethanol (Alfa Aesar, Ward Hill, MA) was pipetted into the suspension to quench free EDC and SNHS in solution, and the suspension was allowed to rotate for an additional 10 mins. The sample was centrifuged and thoroughly washed with water and then resuspended in 4 ml of a phosphate-buffered saline (PBS) solution (100 mM, pH 7.2) containing 1 ml of tris(2-aminoethyl)amine (TAEA) (Alfa Aesar, Ward Hill, MA) and gently rotated for 2 hrs. Afterwards, the sample was pelleted by centrifugation and thoroughly washed with water and methanol. The sample was then dried overnight at 65 °C. The dried sample was suspended in a solution of 8 ml of ethanol and 4 ml of dipentaerythritol penta/hexa-acrylate (Alfa Aesar, Ward Hill, MA) and gently rotated for 2 hrs. Afterwards, the sample was pelleted by centrifugation and washed thoroughly in ethanol. In the final step, the sample was suspended in 5 ml of ethanol with 8 mg of an amino-terminated polyacrylic acid (P5839A-AANH2 from Polymer Source Inc., Montreal, Quebec) and gently rotated for 2 hrs, after which the sample was pelleted by centrifugation and washed thoroughly in ethanol, and then finally dried overnight at 65 $^{o}$C.

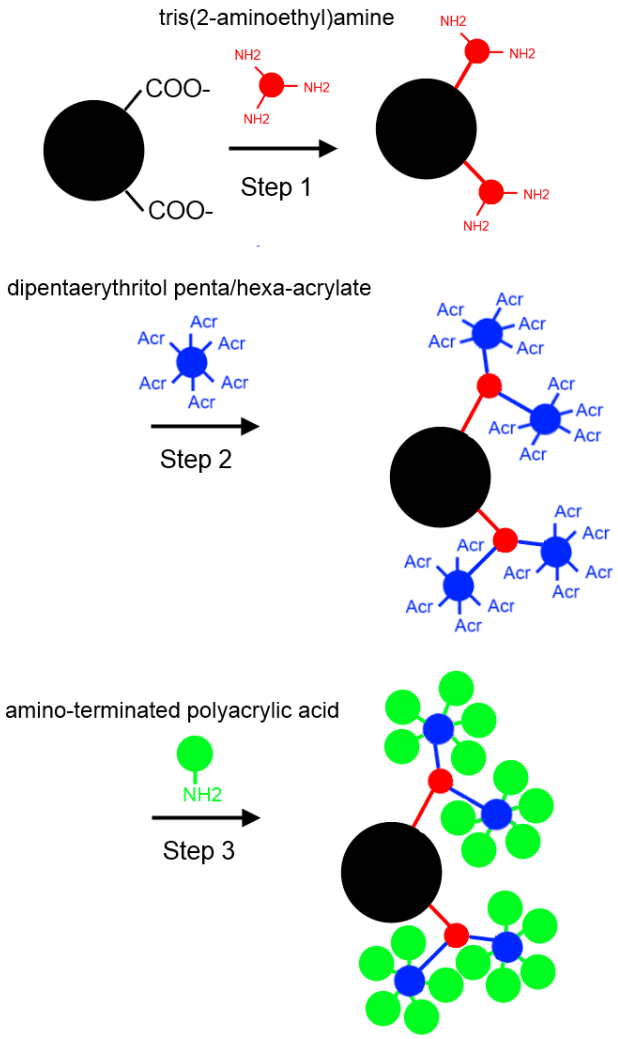


Figure 4.2: Schematic of dendritic amplification of surface carboxylates on $HNO_3$-oxidized carbon.

### 4.2.5 Enzyme Loading of Surface Modified CDE

The model enzyme glucose oxidase (GOx) was loaded onto surface-modified CDE to test these samples as supports for enzyme biocatalysts. Enzymes may be attached to a surface carboxylate site either by chemical crosslinking of the carboxylate with a terminal amine on the enzyme or by electrostatic attachment. The typical pH of a

practical enzyme solution is 7.0. At this pH, a carboxylate-functionalized surface is negatively charged (pKa values of carboxylic acid groups are generally < 5[68]). Electrostatic attachment of the enzyme then requires the enzyme to be positively charged at neutral pH. However, the model enzyme studied in this work, glucose oxidase, does not possess this quality[69]. GOx may be cross-linked with a polycationic peptide, protamine (PA), which can provide positive charge to allow for electrostatic attachment to the negatively charged carboxylate surface sites. Furthermore, if enzyme attachment to the CDE surface occurs at the PA component, then the CDE surface may not as significantly influence conformational changes in GOx. Such surface influences could inhibit the enzyme's catalytic activity.

GOx-PA was synthesized by the method described by Haase, et al.[71] (performed by Dr. Vonda Sheppard). GOx-PA was loaded onto $CDE_{48hr/ox}$ and $CDE_{48hr/ox/amp}$ ($CDE_{48/hr}$ samples subjected to dendritic amplification described in section 4.2.4). One milligram of sample was incubated with variable amounts of GOx-PA in a tris-HCl buffer (50 mM, pH 7.0) solution at room temperature for 20 hrs with gentle agitation. Afterwards, the suspension was centrifuged and the supernatant was collected and saved for later analysis. The pelleted sample was washed thoroughly with the tris-HCl buffer (50 mM, pH 7.0) solution. The sample and supernatant were subjected to a standard activity assay for glucose (Glucose (HK) Assay Reagent, Sigma-Aldrich, St. Louis, MO) to determine the presence of GOx-PA. The activity assay as performed on the supernatant was used to determine if the sample had reached its saturation point with GOx-PA. If no GOx activity was found for the supernatant, then it was assumed that the

sample was not saturated with GOx-PA, and the sample was incubated with increasing amounts of GOx-PA until GOx activity was detected for the supernatant.

### 4.2.6 Synthesis of Au-Bearing Diatom Replicas from High Surface Area C Diatom Templates

To convert high SSA CDE into Au-bearing replicas (AuDE), $CDE_{48hr/ox}$ was treated in a Sn-sensitizing solution to introduce surface-bound $Sn^{2+}$ (chelated by surface carboxylates) sites[71]. $CDE_{48hr/ox}$ was treated for 1 hr at room temperature in a 26 mM $SnCl_2$ (Alfa Aesar, Ward Hill, MA) and 70 mM trifluoroacetic acid (American Bioanalytical, Natick, MA) solution in a 1:1 mixture of $H_2O$ and MeOH solvent. Gentle agitation was provided during treatment. Afterwards, the samples were pelleted in a centrifuge, washed thoroughly in water and methanol, and dried overnight at 60 °C.

Surface bound $Sn^{2+}$ was then used to reduce a solution of $Ag^+$ to $Ag^0$ on the surface of CDE, according to the reaction[72]:

$$2Ag^+ + Sn^{2+} \rightarrow 2Ag^0 + Sn^{4+} \quad (4.3)$$

Sn-sensitized $CDE_{48hr/ox}$ was treated in a solution of ammoniacal 30 mM $AgNO_3$ (Mallinckrodt, Paris, NY), for 15 mins with gentle agitation[71]. Afterwards, the sample was pelleted in a centrifuge, washed thoroughly in water and methanol, and dried overnight at 60 °C.

The Ag-coated CDE was then converted to a fully metallic replica through pyrolysis of the C substrate at 300 °C for 2 hrs in air. The Ag-coated CDE samples were placed in an MgO boat and inserted into a preheated furnace open to air. After pyrolysis, the samples were immediately removed from the hot furnace and allowed to cool down in

air to room temperature in a 10 min span, so as to minimize Ag oxidation. Thermodynamically, Ag oxidation should not occur at 300 °C[20], and air quenching is used to avoid oxidation during cool down.

The following redox displacement reaction was then applied to the CDE-templated, free-standing AgDE:

$$3Ag(s) + HAuCl_4 \rightarrow Au(s) + 3AgCl(aq) + HCl(aq) \quad (4.4)$$

to convert AgDE into Au-bearing diatom replicas (AuDE)[72]. A 50 ml aqueous solution of 10 μmol $HAuCl_4$ (Alfa Aesar, Ward Hill, MA) was prepared and AgDE was poured into the room temperature solution. The solution was then heated to 100 °C in reflux, and treatment was carried out at this temperature for 10 mins. After treatment, the solution was cooled to room temperature and the sample was pelleted in a centrifuge, washed thoroughly with water and methanol, and dried overnight at 60 °C.

### 4.2.7 GOx-PA Loading of AuDE

To generate negative charge sites for GOx-PA binding, 3-mercaptopropionic acid (MPA) (Aldrich, St. Louis, MO) was introduced to the AuDE surface. MPA is known to self-assemble upon a Au surface via gold-thiolate bonding[73]. AuDE was suspended in a 1 M ethanolic MPA solution and incubated with rotation at room temperature for 24 hrs. After incubation, the powder was pelleted from suspension with centrifugation and washed with a 50 mM tris-HCl (pH 7.0) buffer solution (performed by Dr. Vonda Sheppard).

To immobilize GOx-PA on MPA-coated AuDE, the sample powder was suspended in a 50 mM tris-HCl (pH 7.0) solution and incubated with GOx-PA with

rotation for 20 hrs. The GOx-PA saturation was determined as described in the section 4.2.5 (performed by Dr. Vonda Sheppard). After incubation, the sample was pelleted with centrifugation and washed thoroughly with a 50 mM tris-HCl (pH 7.0) solution.

### 4.2.8 Catalytic Activity Testing of GOx-PA Loaded C and Au Materials in an In-line Flow-through System

An in-line flow-through system was assembled to test the catalytic activity of GOx-PA-loaded $CDE_{48hr/ox/amp}$, $VC_{48hr/ox}$ (48 hour acid-oxidized Vulcan carbon black), AuDE, AuNP (Au nanoparticles) and DE (Figure 4.3). For each sample, a suspension with 200 ml of solid volume was pipetted onto a nylon membrane (200 nm pore size, Millipore, Billerica, MA) supported by a stainless steel mesh, which was then sealed in an in-line filter cartridge. A peristaltic pump was used to circulate solution from a glucose bath through the in-line filter cartridge at a rate of 10 ml $min^{-1}$.

At the start of each test, the glucose bath consisted of a 50 ml solution of 20 mM glucose in a sodium acetate buffer (100 mM, pH 5.5) solution. At periodic 5 min intervals over a 2 hr span, a 0.2 ml aliquot of the glucose bath was collected. The glucose concentration for each aliquot was then determined by a standard glucose assay (Glucose (HK) Assay Reagent, Sigma-Aldrich, St. Louis, MO). Such measurements were used to obtain the extent of glucose consumption with flow-through time. An initial glucose decomposition rate was determined by a linear fit of the glucose concentration in the bath as function of time for the first 15 minutes of flow-through.

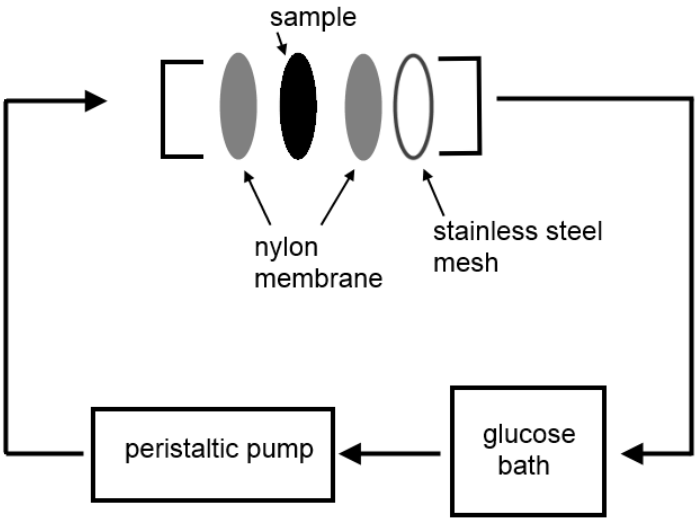


Figure 4.3: Schematic of in-line flow-through system for testing efficacy of GOx-PA-loaded supports at catalyzing glucose decomposition.

### 4.2.9 Sample Characterization

SE images were obtained using a LEO 1530 FE-SEM (Carl Zeiss SMT, Thronwood, NY) at a 15 kV accelerating voltage. An Autosorb-1 (Quantachrome Instruments, Boynton Beach, FL) was used to obtain surface area and pore size distribution measurements using BET/NLDFT methods. An X'Pert Pro Alpha-1 diffractometer configured in glancing angle mode was used to obtain XRD patterns of samples. For these measurements, a fixed incident angle of 1° was used with Cu $K_{\alpha}$ radiation. XRF analysis was performed using a Mini-PAL 4 (PANalytical, Almelo, the Netherlands) instrument configured with Ag and Al x-ray sources. The PANalytical Omnian model was employed for quantitative determination of elemental composition. Zeta-potential measurements were conducted by suspending powder samples in tris-HCl buffer (100 mM, pH 7.0) and DLS analysis was performed using a Zetasizer Nano ZS

(Malvern Instruments, Malvern, UK). The Smoluchowski approximation was applied to the collected DLS data to determine zeta-potential[74].

## 4.3 Results and Discussion

### 4.3.1 Characterization of β-SiC and C Diatom Replica Powders

SEM/XRD analyses of the β-SiC and C diatom replicas are shown in Figure 4.4. The morphology of the diatom frustule was well maintained through all steps of conversion. The β-SiC grain size was found to be 53 nm by Scherrer analysis. The CDE are found to be composed of an amorphous, graphite-like ($sp^2$-bonded) carbon.

The β-SiC product powder was found to have a surface area which closely matched that of the SiDE template powder (Table 4.1). This is attributable to the similar molar volumes of Si and β-SiC (12.05 and 12.47 $cm^3\ mol^{-1}$ respectively[75]), and the fact that no new pores are being generated during this stage of processing. The CDE powder was found to have a greatly enhanced surface area (1370 $m^2\ g^{-1}$), as well as specific mesopore volume (SMeV) (1.53 $cm^3\ g^{-1}$). In addition, a large specific micropore volume (SMiV) (0.282 $cm^3\ g^{-1}$) was generated by the selective etching of Si.

Table 4.1: BET/NLDFT surface area and pore size analysis of diatom and diatom replica samples[56b*].

| Sample | SSA ($m^2\ g^{-1}$) | SMiV ($cm^3\ g^{-1}$) | SMeV ($cm^3\ g^{-1}$) |
|---|---|---|---|
| $SiO_2$ | 1.7 | n.d. | 0.005 |
| Si | 52.6 | n.d. | 0.448 |
| β-SiC | 48.4 | n.d. | 0.370 |
| C | 1370 | 0.282 | 1.53 |

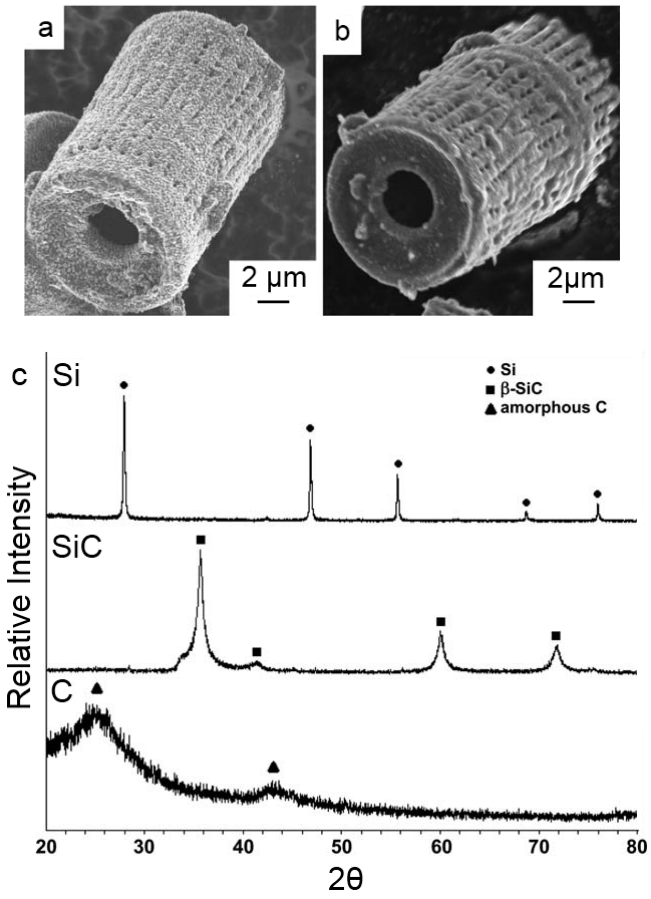


Figure 4.4: Characterization of DE replicas: a) SE image of β-SiC frustule replica, b) SE image of C frustule replica (CDE), c) XRD analysis of Si, SiC and C diatom replica powders[56b*,75].

### 4.3.2 Loading of C Diatom Replica Powder with Pt Nanoparticle Catalysts

Loading of a Pt phase into the CDE microparticles was confirmed by XRD analysis of the treated CDE (Figure 4.5a). HRTEM analyses of cross-sections of the Pt-loaded powder indicated that embedded in the porous CDE structure were very fine (~1-2 nm) Pt particles, meaning that the particle size was likely constrained by surrounding micropore cavities (Figure 4.5b). BET/NLDFT analysis (Table 4.2) of the Pt-loaded CDE powder revealed a significant drop in microporosity upon Pt loading (0.282 to

0.0584 $cm^3$ $g^{-1}$), which was consistent with significant filling of the CDE micropores. Based on these results, the micropores of the CDE appeared to be an important feature in constraining the size of the growing Pt nanoparticles during deposition. Constraint of the Pt particle size is desirable, as it results in an enhanced surface area to mass ratio of the embedded Pt phase.

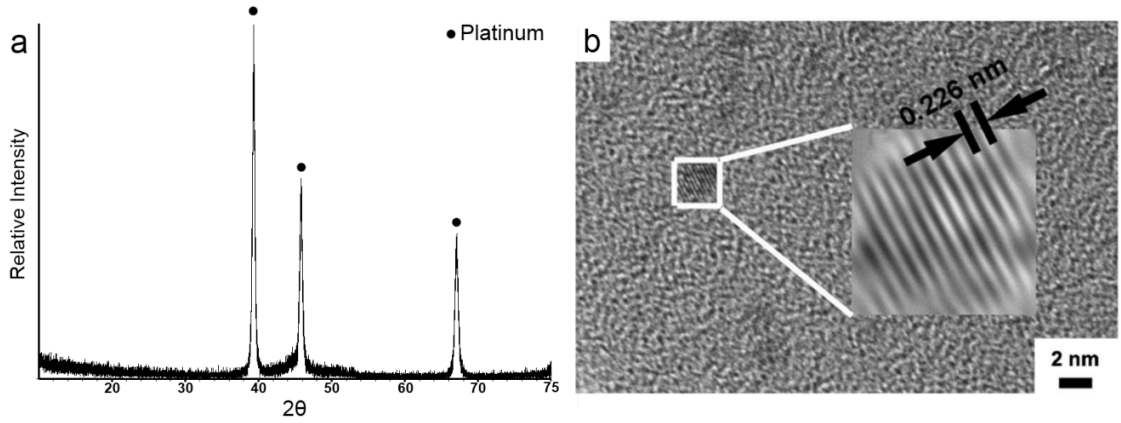


Figure 4.5: Characterization of CDE after Pt-impregnation: a) XRD analysis of Pt-impregnated CDE, b) HRTEM of Pt nanoparticles embedded in the CDE structure[56b*]. (Provided by Dr. Ye Cai)

Table 4.2: BET/NLDFT surface area and pore volume comparison of C diatom replicas and C controls before and after Pt-loading[56b*].

| Sample | SSA ($m^2$ $g^{-1}$) | Specific Mesoporosity ($cm^3$ $g^{-1}$) | Specific Microporosity ($cm^3$ $g^{-1}$) |
|---|---|---|---|
| C Diatom | 1370 | 1.53 | 0.282 |
| C Diatom + Pt | 662 | 0.689 | 0.0584 |
| Vulcan XC72R | 227 | 0.413 | 0.0232 |
| XC72R + Pt | 141 | 0.183 | 0.0215 |
| SiC-derived Microporous C | 1230 | 1.40 | 0.286 |

Table 4.2 (continued)

| | | | |
|---|---|---|---|
| SiC-derived Microporous C + Pt | 734 | 0.837 | 0.170 |

For comparison, Vulcan XC72R carbon black was subjected to similar processing. Vulcan XC72R is highly macroporous (Table 4.2), as well as containing some degree of mesoporosity (0.431 $cm^3 g^{-1}$ SMeV), but does not possess the high degree of microporosity found in the CDE (only 0.0232 $cm^3 g^{-1}$ SMiV in Vulcan C). In addition, this sample does not possess the hollow, thin-walled structure of the *Aulacoseira* diatom frustule (Figure 4.6). Upon Pt loading, the SMiV of the Pt-loaded Vulcan C was found to be 0.0215 $cm^3 g^{-1}$, indicating little of the micropore volume was filled by Pt, which means that Pt particle size was not significantly constrained by structural microporosity as in the case of the Pt-loaded CDE.

Since Vulcan C possesses a large degree of macroporosity, a highly micro-/mesoporous control sample that lacks macroprosity is also required to prove that the hierarchical porosity of CDE provides a performance advantage in catalytic applications. SiC microparticles were subjected to similar Si chlorination as SiC diatom replica powders to produce a highly micro-/mesoporous C sample. This sample possessed comparable surface area (1230 $m^2 g^{-1}$) as well as SMiV (0.286 $cm^3 g^{-1}$) and SMeV (1.40 $cm^3 g^{-1}$) as CDE (Table 4.2). However, these SiC-derived C powders do not have the same large macropores that occur naturally in the diatom frustule structure. These SiC-derived powders were subjected to similar Pt-loading as the C diatom frustule replicas. A similar drop in SMiV was detected after Pt-loading (0.286 to 0.170 $cm^3 g^{-1}$), indicating filling of micropores by Pt.

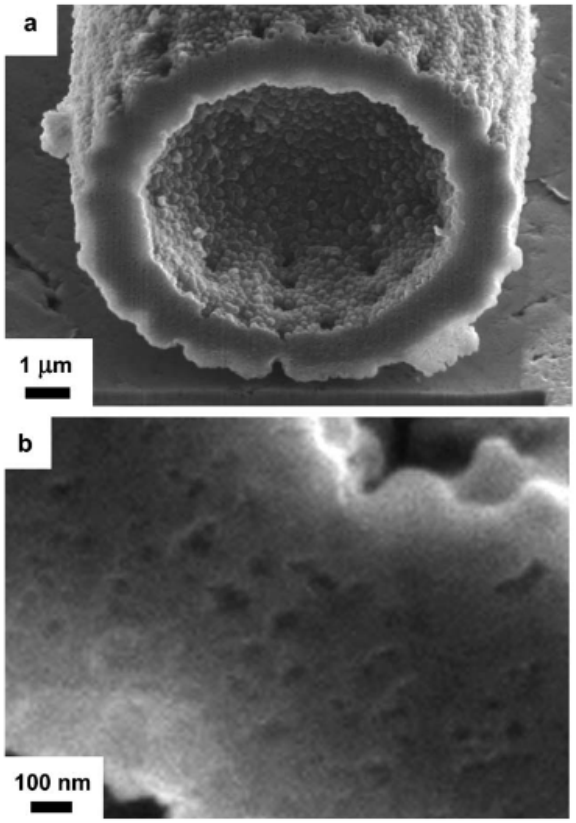


Figure 4.6: SE image of FIB cross-sectioned C diatom frustule replica[56b*]. (Provided by Dr. Ye Cai)

The mass ratio of Pt:C in Pt-loaded samples was controlled by the ratio of $PtCl_2$:C during Pt infiltration. However, similar ratios of $PtCl_2$:C did not yield similar Pt loading across the C powder samples tested. For CDE and commercial SiC-derived C powder, treatment using 240 mg of $PtCl_2$ produced Pt-loading values of 38.3 wt.% and 41.4 wt.% respectively, as determined by TGA measurements. However for Vulcan C, only 10.5 wt.% Pt-loading was achieved under these conditions. The greatly reduced Pt-loading in Vulcan C may be attributed to the much lower SSA of such samples. Increasing the amount of $PtCl_2$ used during Pt-loading of Vulcan C had only a small effect on the wt.%

of the deposited Pt phase. The mass ratio of $PtCl_2$:Vulcan C was increased up to 4:1, and only 14.2 wt.% Pt could be achieved.

### 4.3.3 Electrocatalytic Testing of Pt-Loaded C Diatom Frustule Replicas

Electrocatalytic testing of the Pt-loaded C samples was carried out with respect to the oxygen reduction reaction (ORR), which occurs at the cathode of PEM fuel cells[59]. The results of electrocatalytic testing of Pt-loaded C samples are shown in Figure 4.7 (provided by Dr. Min Kyu Song). Chronoamperometric analysis (Figure 4.7a) was carried out at 0.8 V (vs. Normal Hydrogen Electrode), an operating voltage comparable to those used in PEMFCs[76]. Chronoamperometry indicated a significantly higher steady state current for the Pt-loaded CDE than for the two Pt-loaded C controls. The polarization curves for each sample, taken at variable operating voltages, showed considerably higher current densities at potentials $\geq 0.9$ V for Pt-loaded CDE than for the controls (Figure 4.7b). At these potentials, the kinetics of the ORR is controlled by charge-transfer kinetics (the transfer of charge from Pt to O). The higher current densities in both of these analyses imply a higher rate of reaction, and therefore a higher catalytic activity of Pt, for the samples based on CDE supports.

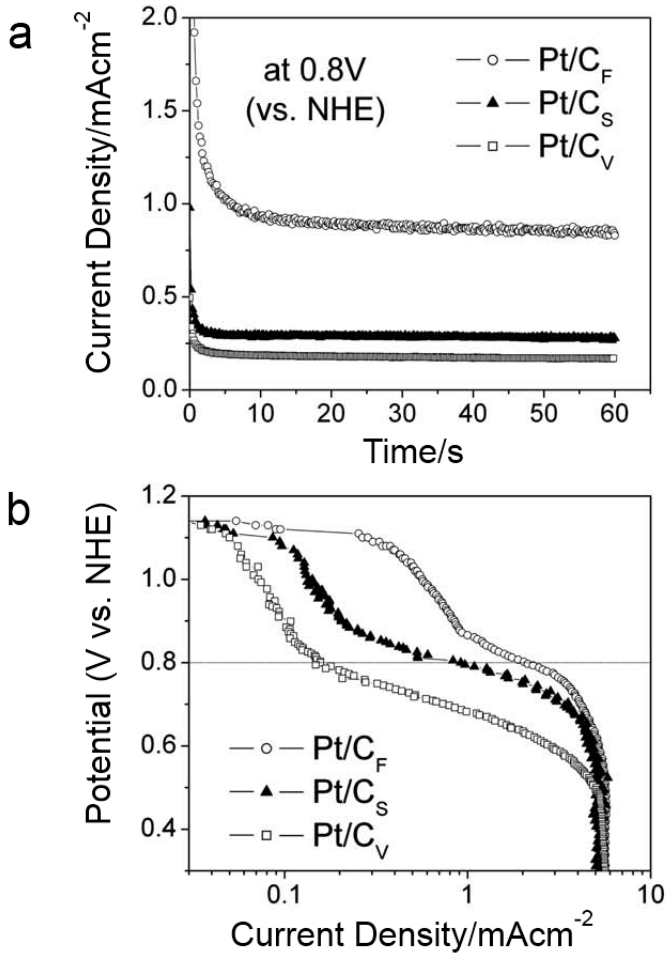


Figure 4.7: Results of electrocatalytic testing of Pt-loaded carbons with respect to oxygen reduction[56b*]: a) chronoamperometric analysis at 0.8V vs. NHE, and b) polarization curve. $Pt/C_F$=Pt-loaded CDE, $Pt/C_s$=Pt-loaded SiC-derived C, $Pt/C_V$=Pt-loaded Vulcan XC724 (Provided by Dr. Min Kyu Song)

### 4.3.4 Characterization of CDE with Surface Modified Acidic Sites

FTIR analysis (performed by Dr. Gousia Begum) was used to characterize the functional groups introduced to the CDE surface after acid oxidation and dendritic amplification of surface carboxylates. Initially, CDE only displayed an absorption band at 1585 $cm^{-1}$, which has been shown to be characteristic of $sp^2$-bonded carbon[77a]. Upon

acid oxidation for 48 hrs, the C=O stretching vibration (1719 $cm^{-1}$) characteristic of surface carboxylate anions[77b] became apparent. The dendrimer-surface-modified CDE ($CDE_{amp}$) displayed several absorption bands consistent with functional groups possessed by the polyamine and polyacrylate components of the dendrimer, including a C-N stretching vibration consistent with amine at 1036 $cm^{-1}$, an O-H bending vibration consistent with alcohol (present on the polyacrylate) at 1055 $cm^{-1}$, an N-H bending vibration consisted with amide at 1554 $cm^{-1}$, as well as the characteristic C=O stretching vibration of surface carboxylate anions[77b].

The loading of surface carboxylates on $CDE_{ox}$ was characterized through zeta-potential measurements at neutral pH and is shown in Figure 4.8. As carboxylic acid groups typically have very low $pK_a$ values[68], surface carboxylates under these conditions should induce a negative surface charge on CDE. Zeta-potential measurements were conducted by suspending $CDE_{ox}$ in tris-HCl buffer (100 mM, pH 7.0). Immediately noticeable was the high hydrophilicity of the $CDE_{ox}$ samples, which readily formed suspensions, whereas the non-acid-oxidized samples rapidly settled from solution. The magnitude of negative surface charge was found to increase with increasing acid oxidation times up to 48 hrs, when surface charge reached a maximum -23.0 mV.

For acid oxidation times longer than 48 hrs, the CDE structure was found to have thoroughly disintegrated (Figure 4.8). For this reason, the dendritic amplification process was developed to increase surface carboxylate loading beyond that which can be accomplished by acid oxidation before the onset of structural disintegration. The dendritic amplification process was applied to CDE that had undergone acid oxidation for 1 hr ($CDE_{1hr/ox}$) and 48 hrs ($CDE_{48hr/ox}$). For $CDE_{1hr/ox}$, the negative surface charge

increased from -1.92 mV to -10.1 mV (a factor of 5.26). For $CDE_{48hr/ox}$, the negative surface charge increased from -23.0 mV to -31.1 mV (a factor of 1.35). The reduced amplification factor for the $CDE_{48hr/ox}$ sample is likely the result of the higher density of surface carboxylates prior to the dendritic amplification process. Steric crowding likely led to a reduced ability of the dendrimer to access all available surface carboxylate sites on the $CDE_{48hr/ox}$.

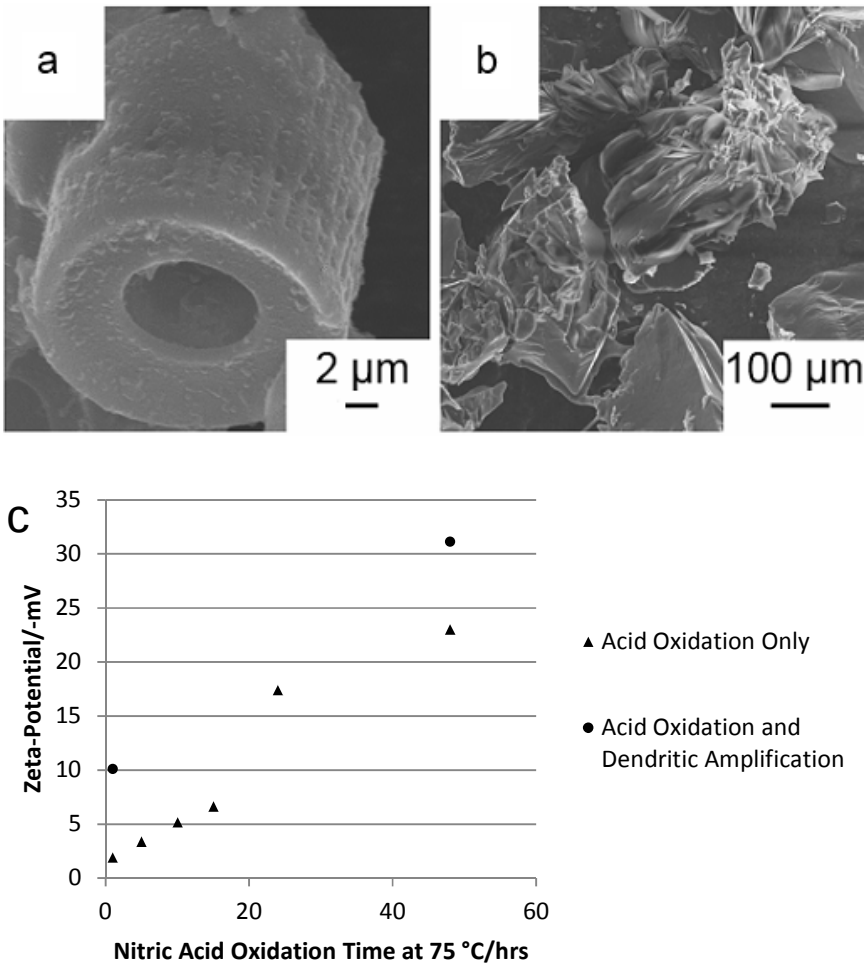


Figure 4.8: Structural integrity of CDE during $HNO_3$ oxidation: a) intact CDE structure after 48 hrs of $HNO_3$ oxidation, b) disintegrated CDE after 72 hrs of $HNO_3$ oxidation, c) zeta-potential of acid-oxidized CDE as a function of surface treatment time.

BET/NLDFT analyses of the surface-modified CDE samples are reported in Table 4.3. BET analysis shows a decrease in SSA after acid oxidation. For $CDE_{1hr/ox}$, the SSA decreased from 1330 $m^2 g^{-1}$ to 898 $m^2 g^{-1}$. However for $CDE_{48hr/ox}$, acid oxidation only reduced the SSA to 793 $m^2 g^{-1}$, meaning there was initially a very large loss in SSA, followed by a more modest decrease with longer acid oxidation time. Upon application of the dendritic amplification process to $CDE_{48hr/ox}$ (becoming $CDE_{48hr/ox/amp}$), the SSA value was found to be 180 $m^2 g^{-1}$, which was a large loss in SSA attributable to the addition of the dendrimer. After dendritic amplification, microporosity was no longer detectable in the sample. Micropores in the structure were apparently blocked/filled by the developed dendrimer. For enzyme loading, loss of microporosity is not a concern, as the bulky nature of enzyme molecules precludes them from accessing such small pores. For mesoporosity, there was also a large loss due to the applied dendrimer. The SMeV was found to drop from 1.160 $cm^3 g^{-1}$ to 0.307 $cm^3 g^{-1}$.

Table 4.3: BET/BJH analysis of surface modified CDE samples.

| | Specific Surface Area ($m^2 g^{-1}$) | Specific Micropore Volume($cm^3 g^{-1}$) | Specific Mesopore Volume ($cm^3 g^{-1}$) |
|---|---|---|---|
| CDE | 1330 | 0.282 | 1.530 |
| $CDE_{1hr/ox}$ | 898 | 0.329 | 0.628 |
| $CDE_{48hr/ox}$ | 793 | 0.212 | 1.160 |
| $CDE_{48hr/ox/amp}$ | 180 | none detected | 0.307 |
| $CDE_{48hr/ox/2amp}$ | 93.8 | none detected | 0.0842 |
| VC | 227 | 0.0232 | 0.413 |
| $VC_{48hr/ox}$ | 63.6 | 0.0190 | 0.0370 |

The possibility existed to grow a larger, more extensively branched dendrimer on the CDE surface by introducing additional layers of polyamine and polyacrylate between

the polyacrylate and amine-terminated polyacrylic acid layers of the molecule. Such an approach is essentially a second cycle of amplification ($CDE_{48hr/ox/2amp}$). Upon treating $CDE_{48hr/ox}$ in this manner, the surface charge was found to decrease to -9.1 mV and the SSA was found to decrease to 93.8 $m^2 g^{-1}$. The large decrease in magnitude of negative surface charge upon this extended amplification is likely due to the large loss in pore volume. The SMeV was found to decline from 0.307 $cm^3 g^{-1}$ to 0.0842 $cm^3 g^{-1}$ upon inclusion of the additional layers of polyamine and polyacrylate. The loss of mesoporosity was likely the cause of the reduced negative surface charge, as there was a lower surface area to support carboxylate sites.

### 4.3.5 Enzyme Loading of Surface Modified CDE

Saturated GOx-PA loadings of various samples are compared in Table 4.4 (provided by Dr. Vonda Sheppard). GOx-PA saturation for a given sample should be a function of the SSA and negative surface charge (indicative of the amount of carboxylate binding sites). For $CDE_{ox/amp}$ specimens, the negative surface charge was greater than for $CDE_{ox}$ specimens. On the other hand, the SSA for the $CDE_{ox/amp}$ was considerably lower. Comparison of the GOx-PA saturation for $CDE_{48hr/ox}$ and $CDE_{48hr/ox/amp}$ showed that much higher GOx-PA saturation was achievable with dendritic amplification ($63.7x10^{-3}$ g GOx-PA $g^{-1}$ support for $CDE_{48hr/ox/amp}$ vs. $34.6x10^{-3}$ g GOx-PA $g^{-1}$ support for $CDE_{48hr/ox}$). Although dendritic amplification resulted in a much lower SSA, much of the SSA loss was attributable to the filling/blocking of microporosity. As the bulky GOx-PA molecule cannot access the fine micropores, the increased negative surface charge appears to have been more influential than the reduced SSA in producing a higher GOx-PA saturation.

As a control, 48 hour acid-oxidized Vulcan XC72R carbon ($VC_{48hr/ox}$) specimens were also subjected to GOx-PA loading and exhibited a GOx-PA saturation of $12.3x10^{-3}$ g GOx-PA $g^{-1}$ support, which was consistent with the reduced SSA and SMeV of Vulcan C. DE was also subjected to GOx-PA loading, as a $SiO_2$ surface is negatively charged at pH 7.0 (pI of $SiO_2$ ~ 2)[78]. The GOx-PA saturation on DE was $1.9x10^{-3}$ g GOx-PA $g^{-1}$ support, which was much smaller than for CDE and VC samples, and can be attributed to the much the reduced SSA of DE and the higher density of $SiO_2$ relative to C (GOx-PA saturation was normalized to the mass of the support).

Table 4.4: Enzyme loading of GOx-PA at saturation for C-based samples. (Provided by Dr. Vonda Sheppard)

| Sample | Loading of GOx-PA at Saturation (mg enzyme $g^{-1}$ support) |
|---|---|
| DE | 1.9 ± 0.4 |
| $CDE_{48hr/ox}$ | 34.6 ± 0.7 |
| $CDE_{48hr/ox/amp}$ | 63.7 ± 2.3 |
| $CDE_{48hr/ox/2amp}$ | 55.5 ± 1.6 |
| $VC_{48hr/ox}$ | 12.3 ± 0.7 |

### 4.3.6 Gold Conversion of Carbon Diatomaceous Earth Replicas

In the previous sections, surface carboxylation on CDE was used as a means of anchoring organic components. However, surface carboxylates also allow for the possibility of inorganic tailoring of CDE through electroless chemistry. It was hypothesized here that AuDE templated from CDE could be useful as an enzyme support in applications such as biosensors[79a,b], biodelivery[79c], biofuel cells[79d], and other applications which require a porous substrate. An electroless coating method was developed to convert CDE into high SSA AuDE. As a starting point, $CDE_{48hr/ox}$

specimens were activated with $Sn^{2+}$, by chelating aqueous $Sn^{2+}$ cations to surface carboxylates. The anchored $Sn^{2+}$ cations were then used to reduce aqueous $Ag^{+}$ cations to $Ag^{0}$ at the CDE surface. The CDE substrate was then selectively removed via high temperature pyrolysis to yield Ag-bearing diatom frustule replicas (AgDE). Finally, the AgDE was converted into AuDE through the displacement reaction (4.3). Of the possible electroless reactions to coat and/or convert Ag layers to Au layers, this displacement reaction was chosen as the substitution of 3 Ag atoms with only 1 Au atom was expected to lead to an increase in SSA.

SEM/EDS analyses of CDE-templated AuDE specimens are shown in Figure 4.9. The diatom structure was well retained at all stages of the Au metallization process. EDS analysis revealed significant Sn content present in AuDE samples (Figure 4.10b). XRF analysis conducted on the AuDE samples determined the metal basis composition of the AuDE to be 37.9 wt.% Au, 14.1 wt.% Ag, and 48.0 wt.% Sn.

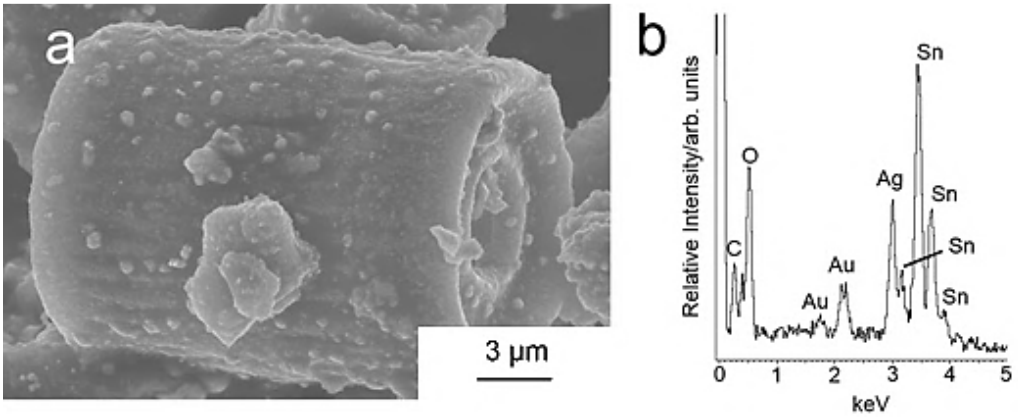


Figure 4.9: SE analysis of CDE-templated AuDE structures: a) SE image of AuDE microparticle structure, and b) EDS analysis of (a).

XRD analysis of a AuDE specimen is presented in Figure 4.10. No crystalline Sn-containing compound was detected by XRD. In AuDE, the Au/Ag grain size was found to be 34.8 nm ± 5.9 nm (note: FCC Au and Ag display XRD peaks with a less than < 0.1° difference[80]).

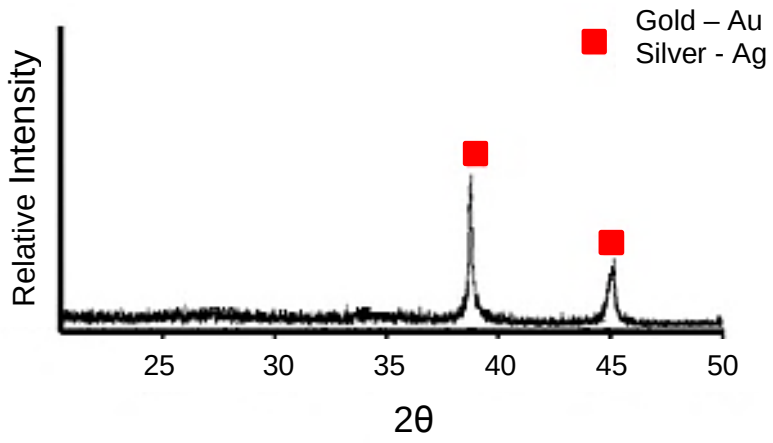


Figure 4.10: XRD analyses of stages of final AuDE product[80].

The lack of an identifiable Sn containing phase via XRD analysis is at odds with the XRF results which indicated that the AuDE samples were comprised of (metals basis) 48.0 wt.% Sn. TEM analysis was performed on AuDE cross-sections to gain a better understanding of the microstructure of the samples (Figure 4.11). Very large crystalline particles were found growing on the outside walls of the diatom frustule replicas, with finer nanocrystalline particles interspersed in an amorphous phase within the interior of the replicas. SAED analysis of the crystalline phase confirmed that it was composed of

FCC Au/Ag. The amorphous matrix phase was likely composed of $SnO_2$, as nanocrystalline $SnO_2$ was found dispersed in the structure as well.

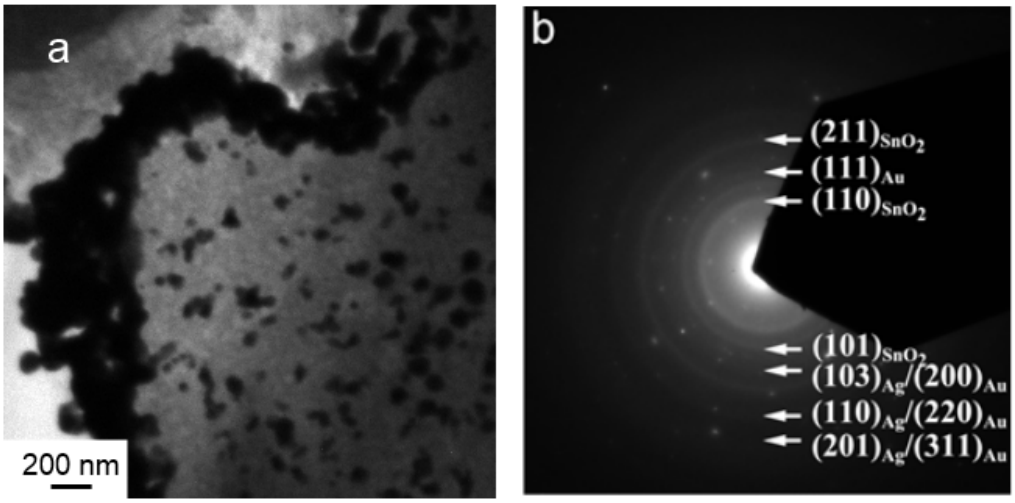


Figure 4.11: TE analysis of AuDE cross-section, a) TE imaging depicting metallic nanoparticles embedded in an amorphous matrix, b) SAED analysis of area represented in (a). (Provided by Dr. Ye Cai)

BET/NLDFT surface area and pore size analyses are reported in Table 4.5. BET analysis indicated that the SSA decreased from 793 $m^2 g^{-1}$ for $CDE_{48hr/ox}$ to 78.2 $m^2 g^{-1}$ for AgDE. Upon conversion into AuDE, the SSA increased to 127 $m^2 g^{-1}$, as a result of the displacement of 3 Ag atoms by 1 Au atom consistent with (4.3), which results in a decrease in solid volume. SMiV and SMeV values followed a similar trend. The value of SSA for AuDE was significantly higher than previously reported SSA values for Au diatom frustule replicas ($\leq$10.1 $m^2 g^{-1}$)[64]. The high SSA of AuDE was attributable to the high SSA of the CDE template and the aforementioned volume-decreasing reaction stoichiometry of (4.3).

Table 4.5: BET/NLDFT analyses of stages of CDE conversion into AuDE.

| Sample | Specific Surface Area ($m^2$ $g^{-1}$) | Specific Micropore Volume ($cm^3$ $g^{-1}$) | Specific Mesopore Volume ($cm^3$ $g^{-1}$) |
|---|---|---|---|
| $CDE_{48hr/ox}$ | 793 | 0.212 | 1.160 |
| AgDE | 78.2 | 0.0148 | 0.153 |
| AuDE | 127 | 0.0298 | 0.206 |

### 4.3.7 GOx-PA Loading of Carbon-templated Gold-bearing Diatom Replicas

Composites of gold nanoparticles in metal oxide matrices have been studied as catalyst supports[81], and although AuDE is not composed exclusively of Au, it may still be useful in certain applications. FTIR analysis was performed on AuDE and MPA-coated AuDE (performed by Dr. Gousia Begum). Upon MPA coating, the AuDE developed an absorption band at 1704 $cm^{-1}$, which was characteristic of the C=O stretching absorption of carboxylic acid present in MPA[77b]. Meanwhile, the S-H stretching absorption band (2573 $cm^{-1}$) was absent, indicating successful adsorption of MPA by gold-thiolate bonding[77b]. Saturated GOx-PA loading of AuDE samples was compared to an MPA-coated Au nanoparticle control (AuNP) (particle size 50-100 nm, SkySpring Nanomaterials Inc., Houston, TX) in Table 4.6. GOx-PA saturation for the MPA-coated AuDE was higher than that of MPA-coated AuNP (15.7 vs. 10.1 mg GOx-PA per g support).

Table 4.6: Enzyme loading of GOx-PA at saturation for Au-based samples. (Provided by Dr. Vonda Sheppard)

| Sample | GOx-PA Loading at Saturation (mg enzyme $g^{-1}$ support) |
|---|---|
| $AuDE_{MPA}$ | 15.7 |
| $AuNP_{MPA}$ | 10.1 |

### 4.3.8 Catalytic Activity of GOx-PA-Loaded Materials

The rate of glucose consumption by GOx-PA-loaded samples in an in-line flow-through reactor was measured to indicate the GOx-PA catalytic activity for each sample. It was expected that GOx-PA catalytic activity should be influenced by two factors. The first was the GOx-PA saturation point, since a higher GOx-PA loading should result in a higher rate of glucose consumption. The second was the structure of the support. The open, hierarchical porosity of the diatom frustule structure was expected to allow for a more rapid mass transport of glucose and its decomposition products to and away from catalytic sites.

$CDE_{48hr/ox/amp}$ specimens were chosen for the flow-through test as these specimens had the highest GOx-PA saturation of all CDE samples. The C control specimen for this experiment was GOx-PA-loaded $VC_{48hr/ox}$. The GOx-PA-loaded Au-bearing samples, $AuDE_{MPA}$ and $AuNP_{MPA}$, were also tested. GOx-PA-loaded DE was tested as a control for the diatom frustule structure. The results of flow-through testing are shown in Table 4.7, where the rates of glucose consumption normalized to weight of loaded enzyme, the specific activity, are compared. The measured specific activities of the diatom-based samples are all comparable. DE showed the highest performance in terms of specific

activity of this group. However, it should be noted that because $CDE_{48hr/ox/amp}$ possesses a higher GOx-PA-loading, the absolute catalytic activity of this sample is actually higher (62.0 vs. 33.9 µmol glucose consumed $min^{-1}$ for $CDE_{48hr/ox/amp}$ and DE respectively). The $VC_{48hr/ox}$ and $AuNP_{MPA}$ controls show similar performance to each other. Since specific catalytic activity is normalized to the amount of loaded enzyme, this value should not be affected by the increased SSA of the diatom-based samples. This means that the higher group performance of the diatom-based samples over the non-diatom-based controls implies a structural advantage of the former. This structural advantage is likely the hierarchical porosity present in the diatom frustule structure that does not exist in the samples without such a pore structure.

Table 4.7: Glucose decomposition activity of GOx-PA-loaded samples.

| Sample | Glucose Decomposition Rate Normalized to GOx-PA Loading (µmol $min^{-1}$ $g^{-1}$ GOx-PA) |
|---|---|
| DE | 56.0 |
| $CDE_{48hr/ox/amp}$ | 51.3 |
| $VC_{48hr/ox}$ | 25.3 |
| $AuDE_{MPA}$ | 49.3 |
| $AuNP_{MPA}$ | 20.7 |

## 4.4 Summary

The pore volume and SSA of SiDE were significantly enhanced via a reactive conversion route that converted Si replicas to replicas of highly-microporous C. First, SiDE was converted into β-SiC by a high temperature (1200 °C) carburization process. Second, Si was selectively removed from the β-SiC replicas to form CDE, during which a

large volume of microporosity was introduced without disrupting the pre-existing macropore structure. The high SSA (> 1300 $m^2 g^{-1}$) and hierarchical porosity of CDE samples offers potential for applications in catalyst supports, especially in flow-through reactors. The activity of Pt-loaded CDE was tested with respect to the oxygen reduction reaction, which occurs at the cathode of PEM fuel cells. Pt-loaded CDE displayed a significant performance advantage over other Pt-loaded microporous carbon and carbon black specimens. CDE was loaded with a model enzyme for testing in a flow-through system, and displayed a significant performance advantage again over a carbon black control.

CDE can also be used as a substrate for the deposition of precious metals. In this work, AuDE fabricated from high SSA CDE was developed as proof. The AuDE was found to have a significantly higher SSA and pore volume than Au diatom frustule replicas reported in previous work. AuDE was loaded with a model enzyme and tested in a flow-through reactor. AuDE displayed a significant performance advantage over a Au nanoparticle control. When catalytic activity was normalized to enzyme loading, all DE-based enzyme supports ($SiO_2$, Au, and C) showed similar enzyme activities, which were significantly higher than that displayed by the spheroidal particle controls (Vulcan C and Au nanoparticles), implying an inherent structural advantage of the diatom-derived particles. The structural advantage of these particles is likely attributable to their hierarchical porosity, which was absent in the controls.

# CHAPTER 5:

# UTILIZATION OF SHAPE-PRESERVING GAS-SOLID DISPLACEMENT REACTIONS IN PHOTONIC APPLICATIONS

## 5.1 Introduction

Silicon is an attractive material for use in photonic structures and devices, owing to the material's high refractive index and low loss in the IR spectrum[82]. In addition, Si microdevice fabrication is highly developed due to its importance in the microelectronics industry. In this chapter, the use of Mg(g)/$SiO_2$ reduction to generate porous Si replicas of complex $SiO_2$ templates has been explored in structures relevant to optical and photonic applications.

Inverse opals are a class of structures that are presently being widely studied in the field of photonics[83]. These structures are composed of a three dimensional periodic arrangement of macropores (Figure 5.1) that possess a photonic bandgap (PBG) at a wavelength related to the pore spacing and dielectric constant of the medium[84]. Applications of inverse opals include telecommunications[85a,b], information processing[85c,d], and chemical sensing[85e,f]. A popular fabrication method for such 3D periodic structures involves the infiltration of self-assembled colloidal crystals composed of spherical polymer particles (e.g., PMMA, PS) with a sol-gel precursor of a metal oxide (e.g. $TiO_2$, $SiO_2$, $GeO_2$), such that the sol-gel precursor fills the interstices between spheres[82]. Hydrolysis of the interstitial sol-gel precursor followed by burnout of the polymer spheres results in the formation of an inorganic inverse opal structure with large macropores remaining in the space originally occupied by the spherical templates[86].

While this method cannot be used to create Si inverse opals directly, it may be used to generate inverse opals of $SiO_2$. Porous Si has been shown to possess a number of difficult to obtain optical properties, including photoluminescence[83a], high refractive index[83b], and low absorbance in the IR spectrum[83b]. In this chapter, the fabrication and properties of porous Si inverse opals are explored through the application of Mg(g)/$SiO_2$ reduction to sol-gel derived $SiO_2$ inverse opals.

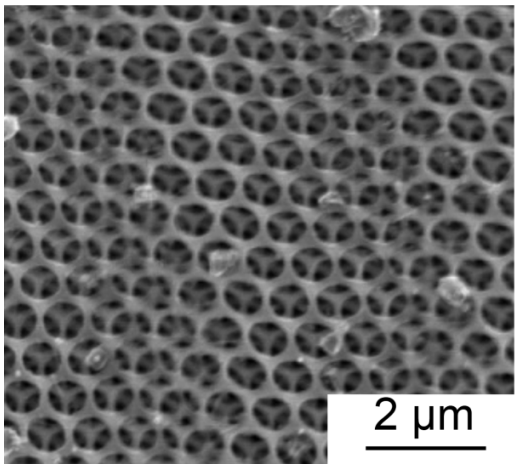


Figure 5.1: Top-down SE image of periodic macroporosity possessed by an inverse opal photonic crystal structure.

Optical chemical sensors based upon on-chip optical resonators are receiving increasing attention in the area of low-cost portable sensors, as these devices have been known to have immunity to interfering electromagnetic radiation, along with high sensitivity, and good compactness[88]. Microcavity resonators are particularly attractive, as these sensors can be several orders of magnitude smaller than the alternatives[88]. In these devices, the resonance frequency of a microcavity resonator is shifted upon the adsorption of an analyte species, which is a result of the interaction of the adsorbed

species with the evanescent tail emerging from the confined electromagnetic field[88]. The addition of a thin porous Si layer to the surface of such a resonator is expected to enhance the chemical sensitivity of the device by offering an increased surface area for the adsorption of analyte. In this chapter, Mg(g)/$SiO_2$ reduction will be used to convert thin oxide films coated on microcavity resonator sensors to porous Si.

### 5.2 Porous Silicon Inverse Opals Derived from Silica-Based Templates

Recently, an innovative "co-assembly" method has been developed to allow for the formation of large-area, crack-free inverse opals of $SiO_2$ by means of colloidal self-assembly of polymer particles[89]. The key difference between this co-assembly method and the standard colloidal assembly method is that, in the co-assembly method, self-assembly of colloidal crystals occurs in a solution that bears the metal oxide sol-gel precursor, whereas in other methods the sol-gel precursor is infiltrated after deposition of the colloidal crystal. It has been found that this new method produces a $SiO_2$ structure with significantly less cracking than the standard method[89]. In addition, the standard method often produces an overlayer film covering the inverse opal as a result of using too great an excess of sol-gel precursor during the infiltration step. This overlayer has been found to be absent in the co-assembly method[89].

Unfortunately, the co-assembly method has so far only been shown to be effective in generating large-area, crack-free inverse opals with TEOS, a sol-gel precursor of $SiO_2$[89]. A $TiO_2$ precursor, TiBALDH, was explored for this method, but a large-area, crack-free inverse opal structure could not be achieved. As $TiO_2$ is an important material in the inverse opal literature, due to its relatively high refractive index and photocatalytic

activity[90], there is an impetus to develop a means to convert $SiO_2$ inverse opals generated by the co-assembly method into $TiO_2$ replicas. Building upon previous work in generating $TiO_2$ diatom frustule replicas[91], the following metathetic gas-solid displacement reaction:

$$SiO_2 + 2TiF_4(g) \rightarrow 2TiOF_2 + SiF_4(g) \quad (5.1)$$

was applied to $SiO_2$ inverse opals generated by the co-assembly method. The $TiOF_2$ replicas could then be converted into $TiO_2$ by treatment with water vapor according to the reaction:

$$TiOF_2 + H_2O(g) \rightarrow TiO_2 + 2HF(g) \quad (5.2)$$

In previous work, this series of reactions has been shown to successfully convert $SiO_2$ diatom frustules to replicas of anatase $TiO_2$[91].

In addition to $TiO_2$, Si inverse opals could also be valuable due to the high refractive index of Si and the low absorption of this material in the IR spectrum[78b]. However, elemental Si cannot be directly generated by sol-gel methods. Instead, in this work, $Mg(g)/SiO_2$ reduction explored in previous chapters has been applied to inverse opals generated by the co-assembly method. The $Mg(g)/SiO_2$ reduction process produces porous Si, which is expected to have a lower refractive index than dense Si, but such porous Si would be ideal for inverse opal chemical sensors. Such a sensor detects the concentration of an adsorbed analyte species through shifts in the reflectance peak of the inverse opal structure[92]. Porous Si would provide a high surface area for the adsorption of analytes, and, thus, sensors based on this material could possess higher sensitivity.

### 5.2.1 Experimental Design - Porous Si and $TiO_2$ Inverse Opal Replicas

5.2.1.1 Synthesis

Mg(g)/$SiO_2$ reduction was applied to $SiO_2$ inverse opal structures to generate porous Si replicas of these structures. Silica inverse opal templates were generated using a novel colloidal self-assembly method ("co-assembly")[89] (inverse opal templates were provided by Dr. Benjamin Hatton). Initially, 1.0 ml of a 2.5 vol.% stock suspension of monodispersed PMMA particles (250-400 nm dia., Invitrogen, Grand Island, NY) was added to 20 ml of dI $H_2O$, along with 0.30 ml of a hydrolyzed TEOS solution (98%, Aldrich, St. Louis, MO), which was composed of a 1:1:1.5 weight ratio mixture of TEOS, 0.10 M HCl, and EtOH. Piranha-cleaned Si wafers were submerged vertically in a vial containing the aforementioned suspension of PMMA in TEOS solution, and treated in an oven at 65 °C for 1-2 days. During this heat treatment, the solution slowly evaporated leaving behind a deposited, well ordered layer of PMMA spheres on the wafer with $SiO_2$ (from hydrolyzed TEOS) filling the interstices between the spheres. The PMMA/$SiO_2$ films were then fired at 500 °C for 2 hrs in air to remove the PMMA and partially sinter the $SiO_2$ framework into a structurally stable inverse opal.

The $SiO_2$ inverse opal structures were then subjected to silica magnesiothermic reduction. As demonstrated in Figure 5.2, a 3-well Fe boat was used to hold the samples and the magnesium vapor source. The inverse opal sample was loaded into an end well of the boat, with 250 mg of $Mg_2Si$ powder (99.5%, Alfa Aesar, Ward Hill, MA) loaded into the opposite end well. The middle well was left clear to catch $Mg_2Si$ powder that may drift toward the inverse opal sample during processing, and thus prevent contamination of the structure. As discussed in Chapter 2, $Mg_2Si$ was chosen as an Mg

vapor source to prevent overreaction of the Si product to $Mg_2Si$. The boat with the sample and reactant was loaded into an Fe ampoule which was sealed in an Ar atmosphere.

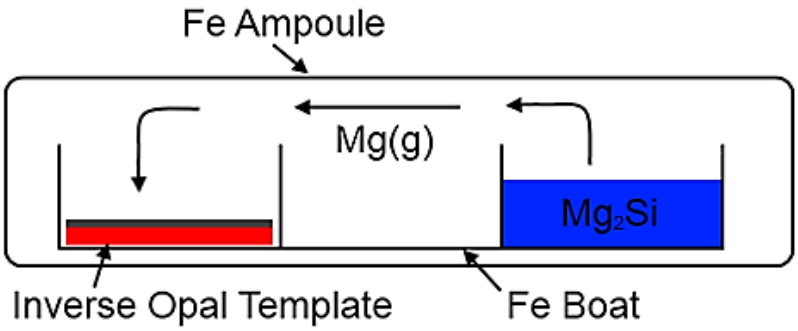


Figure 5.2: Schematic of Mg(g)/$SiO_2$ reduction performed on inverse opal templates.

The ampoules were treated at 850 °C for 4 hrs to allow for full conversion of the $SiO_2$ inverse opal templates to MgO/Si. To prevent thermally-induced mechanical instability in the structure, the ampoules were heated from room temperature to 850 °C at a 5 °C $min^{-1}$ ramp rate. After heat treatment and subsequent cooling to room temperature, the inverse opal samples were removed from the ampoules and treated in 0.10 M HCl for 3 hrs to selectively dissolve the MgO product and generate a porous Si inverse opal structure. Following acid treatment, the samples were washed thoroughly with $H_2O$ and MeOH.

The conversion of $SiO_2$ inverse opal templates into replicas of anatase $TiO_2$ is demonstrated in Figure 5.3. An $SiO_2$ inverse opal sample was loaded into an end well of a 3-well Ni boat, with 100 mg of $TiF_4$ powder (98%, Alfa Aesar, Ward Hill, MA) added to the well on the opposing end. The boat was then contained in a welded Ti ampoule in

an Ar atmosphere (Figure 5.3a). The ampoule was then heated to 215 °C in a horizontal tube furnace at a 5 °C $min^{-1}$ ramp rate and treated for 2 hrs to generate a $TiOF_2$ inverse opal replica. After subsequent cooling to room temperature, the sample was removed from the ampoule. The $TiOF_2$ sample was then loaded onto an MgO crucible and treated in a horizontal tube furnace at 400 °C for 5 hrs to convert $TiOF_2$ to $TiO_2$. Treatment was carried out under a flowing atmosphere of $H_2O$-saturated $O_2$, generated by flowing $O_2$ through an $H_2O$ bubbler at 60 °C, as illustrated in Figure 5.3b. The flow rate was maintained at 200 $cm^3$ $min^{-1}$.

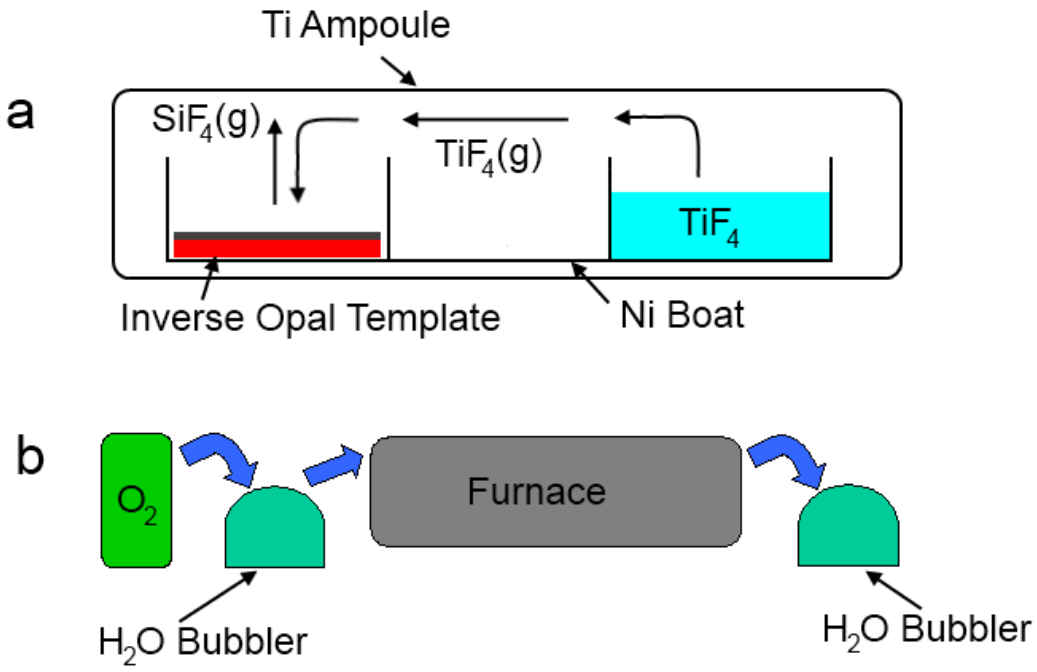


Figure 5.3: Schematic of $TiO_2$ conversion performed on $SiO_2$ inverse opal templates: a) conversion of $SiO_2$ into $TiOF_2$, and b) conversion of $TiOF_2$ into $TiO_2$.

5.2.1.2 Characterization Methods

Reflectance spectra were obtained with a Leica DMRX microscope at a 10x objective with a microscope-based fiber optic spectrometer system (Ocean Optics USB2000+). SEM imaging was obtained on a Zeiss Ultra at 10 kV. TEM imaging was obtained on a JEOL 2100 at 200 kV. Samples for TEM imaging were prepared with crushed fragments that were deposited on Formvar-coated Cu grids (Electron Microscopy Sciences, Hatfield, PA).

### 5.2.2 Results and Discussion - Porous Si and $TiO_2$ Inverse Opal Replicas

5.2.2.1 Porous Si Inverse Opals

SEM analyses of cross-sections of inverse opal samples at each step of the silica magnesiothermic reduction process are shown in Figure 5.4. The inverse opal structure is well maintained at all steps of the conversion process. While interpore spacing is maintained parallel to the substrate, a slight, ~15% contraction was found perpendicular to the substrate. No cracking of the inverse opal structure was found during conversion. TEM/SAED analyses of the inverse opal structure are shown in Figure 5.5. Initially, no crystalline phases were found in the $SiO_2$ inverse opal template (Figure 5.5a). After magnesiothermic treatment (Figure 5.5b,c), MgO and Si crystalline phases are found, and after acid treatment in HCl, only an Si phase was detected. The Si crystallite size was measured to be ~5-10 nm.

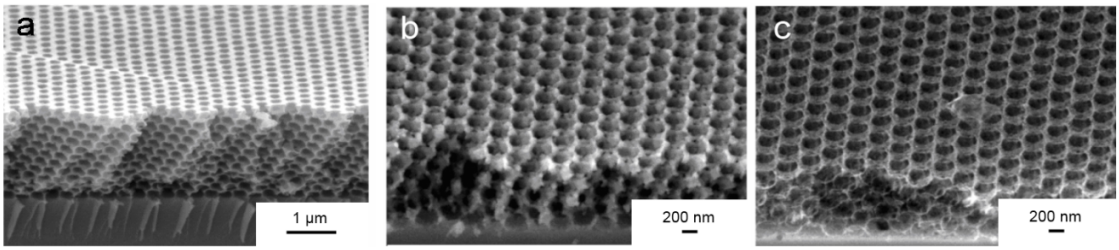


Figure 5.4: SE cross-sectional images of a) $SiO_2$ inverse opal template, b) MgO/Si composite inverse opal replica, c) porous Si inverse opal replica[89]. (Provided by Dr. Benjamin Hatton) Reused with permission from Ref. 89: Copyright 2010 National Academy of Sciences, USA.

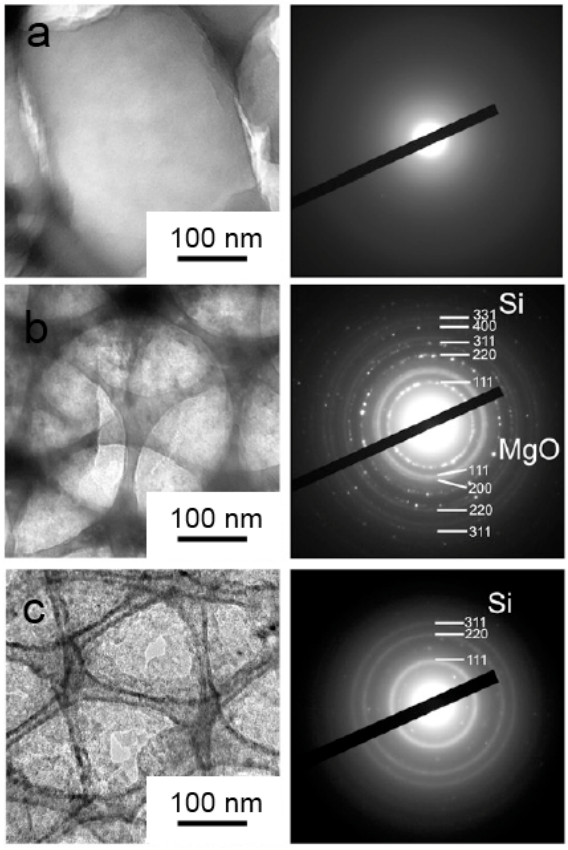


Figure 5.5: (Left) TE images and (Right) SAED analyses of: a) $SiO_2$ template, b) MgO/Si replica, and c) porous Si replica samples. (Provided by Dr. Benjamin Hatton) Reused with permission from Ref. 89: Copyright 2010 National Academy of Sciences, USA.

Reflectance spectra of the inverse opal structures at each stage of magnesiothermic treatment are shown in Figure 5.6. The $SiO_2$ inverse opal templates exhibited a reflectance peak maximum at 460 nm. Upon conversion to MgO/Si, the reflectance peak shifted to longer wavelengths, which was a consequence of the higher refractive index of the MgO/Si composite. Based upon the stoichiometry of the reaction, the MgO/Si composite was expected to be composed of 65 vol.% MgO and 35 vol.% Si. The refractive index of bulk MgO in the visible spectrum is estimated as 1.74[82a]. The refractive index of bulk Si in the visible spectrum is estimated as 4.22[78b]. These values are the refractive indices of these materials at a wavelength of 515 nm. Using a volumetric rule of mixtures approximation, the MgO/Si composite refractive index is expected to be 2.61, which is comparable to rutile $TiO_2$, a widely-regarded high index material[82c,d]. The following equation can be used to determine the reflectance peak of a [111]-oriented FCC structured inverse opal[93]:

$$\lambda_{max} = 2\sqrt{\frac{2}{3}}D\sqrt{n^2 - \sin(\varphi)} \tag{5.3}$$

where $\lambda_{max}$ is the wavelength at which maximum reflectance occurs, D is the diameter of the spherical inverse opal macropores, n is the refractive index of the inverse opal structure (i.e., the composite refractive index of the wall material and inverse opal macropores), and φ is the incident angle of illumination (measured from the sample normal). Using the estimated MgO/Si composite refractive index, the MgO/Si composite structure should have a reflectance peak at 579 nm. This is slightly lower than the observed result of 635 nm, which would indicate that the refractive index of the material must be greater than what was predicted above. The refractive index of the MgO/Si walls

based on the observed reflectance peak was 3.15. The difference between predicted and observed may reflect a higher vol.% of Si in the product or deviations in refractive index of the nanocrystalline MgO/Si structure from bulk values.

Upon MgO dissolution and formation of porous Si, the reflectance peak is seen to shift back to shorter wavelengths. The porosity introduced during this step has a dramatic effect on the refractive index of the inverse opal walls. The air-filled pores in the walls counteract the high refractive index of Si. Based on 65 vol.% air and 35 vol.% Si and using a volumetric rule of mixtures approximation, the expected refractive index of porous Si in these structures was 2.13. The reflectance peak was then expected to be found at 526 nm. The observed reflectance peak is found at 430 nm, significantly lower than what is predicted and below that of the initial $SiO_2$ inverse opal template. Based on these observations, the refractive index of porous Si was calculated to be 1.19. This may be the result of a high content of natively-oxidized Si in the structure, which would not be unreasonably considering the high surface area of the porous Si, or deviation of the refractive index of porous, nanocrystalline Si from that of the bulk Si value.

Although porous Si as produced by $Mg(g)/SiO_2$ reduction was found to have a much lower refractive index than dense Si, the high degree of porosity found in these structures may be advantageous in inverse opal chemical sensors. Indeed, the inverse opal structure is well maintained despite what must be a high vol.% porosity, as indicated by the apparent refractive index of the material. The MgO/Si composite-based inverse opals, however, exhibit a high apparent refractive index. MgO has excellent transparency in the visible and near-IR spectrum, and the MgO/Si structures may be more applicable in applications where high refractive index is required.

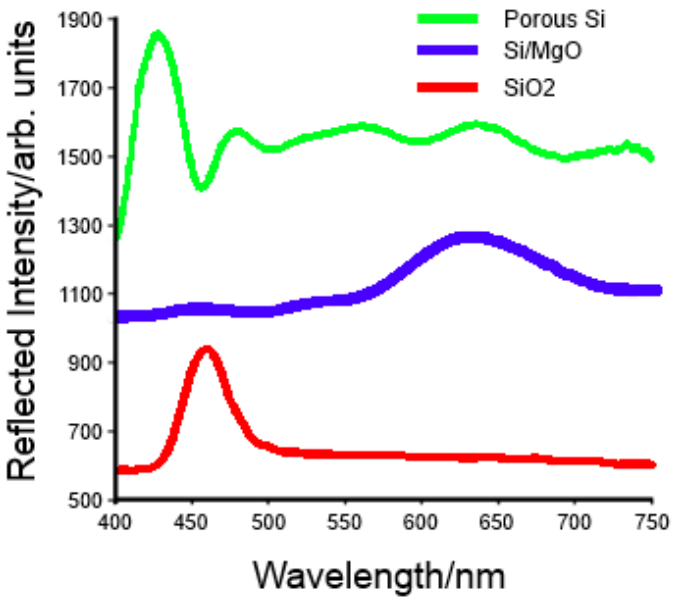


Figure 5.6: Reflectance spectra for inverse opal replicas produced by Mg(g)/$SiO_2$ reduction. (Provided by Dr. Benjamin Hatton)

5.2.2.2 Anatase $TiO_2$ Inverse Opals

SEM analyses of cross-sections from inverse opal structures before and after $TiO_2$ conversion are shown in Figure 5.7. Interpore spacing was well retained after reaction. No cracking of the inverse opal structure was found as a result of reaction. TEM/SAED analyses of the inverse opal structure before and after reaction are shown in Figure 5.8. SAED analysis clearly demonstrated the formation of the anatase polymorph of $TiO_2$ after reaction.

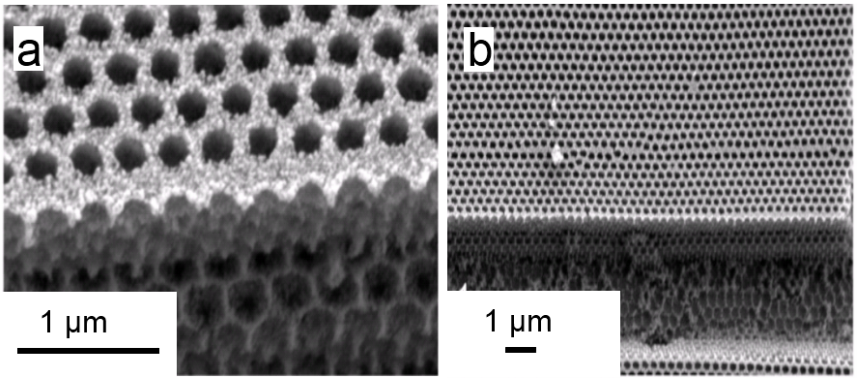


Figure 5.7: SE cross-sectional images of $SiO_2$ inverse opal: a) before conversion to $TiO_2$, and b) after conversion to $TiO_2$. (Provided by Dr. Benjamin Hatton)

Reflectance spectra before and after reaction are shown in Figure 5.9. There is a shift to longer wavelengths upon conversion into $TiOF_2$ and $TiO_2$. The shift was consistent with the greater refractive index of anatase $TiO_2$. Assuming minimal porosity of the $TiO_2$ walls, the expected reflectance peak was 551 nm, based on a refractive index of 2.35 (estimated from the value of the refractive index at a wavelength of 515 nm) for bulk anatase $TiO_2$[82e]. This matches closely with the observed spectrum, which places the reflectance peak at 589 nm, which was consistent with the $TiO_2$ having a low vol.% of pores. The slightly higher than expected refractive index for anatase $TiO_2$ may be the result of residual F doping from the process. In previous work, $TiO_2$ structures produced from the reaction of $SiO_2$ and $TiF_4$ were found to have a significant residual F concentration, which was found to enhance the catalytic activity of the anatase $TiO_2$[91b]. No data could be found regarding the refractive index of $TiOF_2$. However, based on the observed reflectance peak, the refractive index of $TiOF_2$ was calculated to be 2.65.

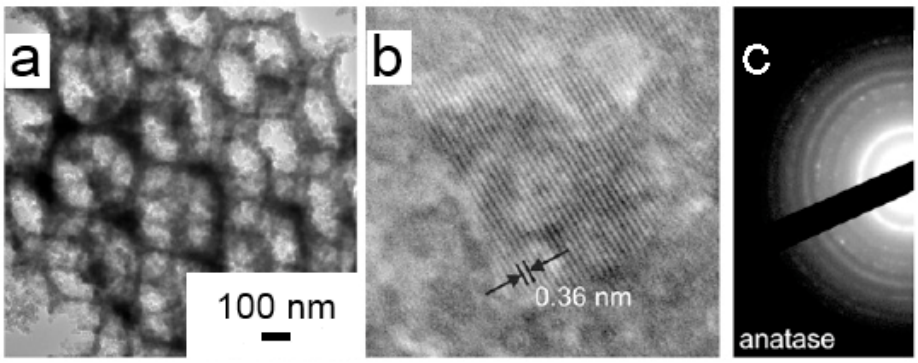


Figure 5.8: TE analysis of $TiO_2$ inverse opal replicas: a) TE imaging of $TiO_2$ inverse opal replica, b) lattice-fringe imaging of $TiO_2$ replica, and c) SAED of $TiO_2$ replica. (Provided by Dr. Benjamin Hatton) Reused with permission from Ref. 89: Copyright 2010 National Academy of Sciences, USA.

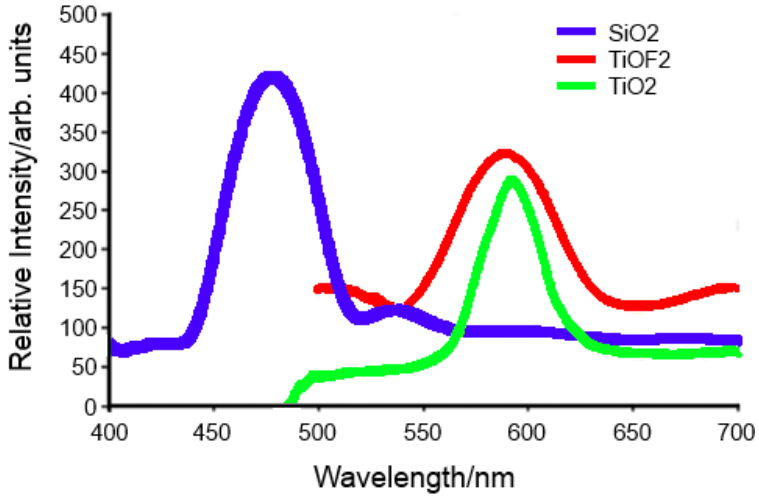


Figure 5.9: Reflectance spectra for inverse opal replicas produced by metathetic displacement reaction between $TiF_4$ and $SiO_2$. (Provided by Dr. Benjamin Hatton)

### 5.3 Porous Silicon Enhanced Optical Chemical Microresonator Sensors

As established in the preceding section, porous Si as produced by the $Mg(g)/SiO_2$ reduction reaction has a high degree of porosity that can make this material highly-

suitable for chemical sensing applications. In this section, Mg(g)/$SiO_2$ reduction has been applied to integrated optical microresonator sensors, which are a new class of optics-based on-chip chemical sensing devices. In these devices, waveguides coupled to microring or racetrack resonators are patterned onto SOI wafers (Figure 5.10). Adsorption of analyte species on the surface of the microring leads to a shift in the absorption (resonance) frequency ($f_r$) of the resonator[85]. It is hypothesized here that the chemical sensitivity of the resonator can be enhanced by cladding the device with porous Si (i.e., introducing a thin layer of porous Si to the surface of the device).

The most common method of generating porous Si on chip is the anodic etching method. In this method, Si is reduced by an anodizing potential, which is then etched by a surrounding HF bath[2]. Etching does not occur evenly across the Si surface, and instead, etch pits are made in the Si, resulting in porosity[2]. It is found that porous Si films of a wide range of morphologies can be attained using this method[94]. The anodic etching method has serious drawbacks when considered for optical and photonic applications. Anodic etching requires greater electrical conductivity than that which is provided by intrinsic Si, and thus doped Si is required[94]. Doping of Si increases electrical conductivity by an increase in free charge carriers. The consequence for optical applications is that the doped Si needed for the anodic porosification method will exhibit significant optical absorption, which would significantly reduce the transmittance of a Si waveguide. In addition, silicon-on-insulator (SOI) substrates are used for integrated waveguide devices (to provide an oxide cladding of the waveguide patterned in the Si device layer). In this material, a ~200 nm Si device layer exists on top of a buried $SiO_2$ layer (as shown in Figure 5.10). Anodic etching in HF would lead to significant damage

of the buried oxide layer due to oxide dissolution in the acid. In this section, it is proposed that Mg(g)/$SiO_2$ reduction of thin $SiO_2$ films grown on the Si device layer can provide a functional alternative for porous Si production that is compatible with the requirements of integrated optical devices on SOI.

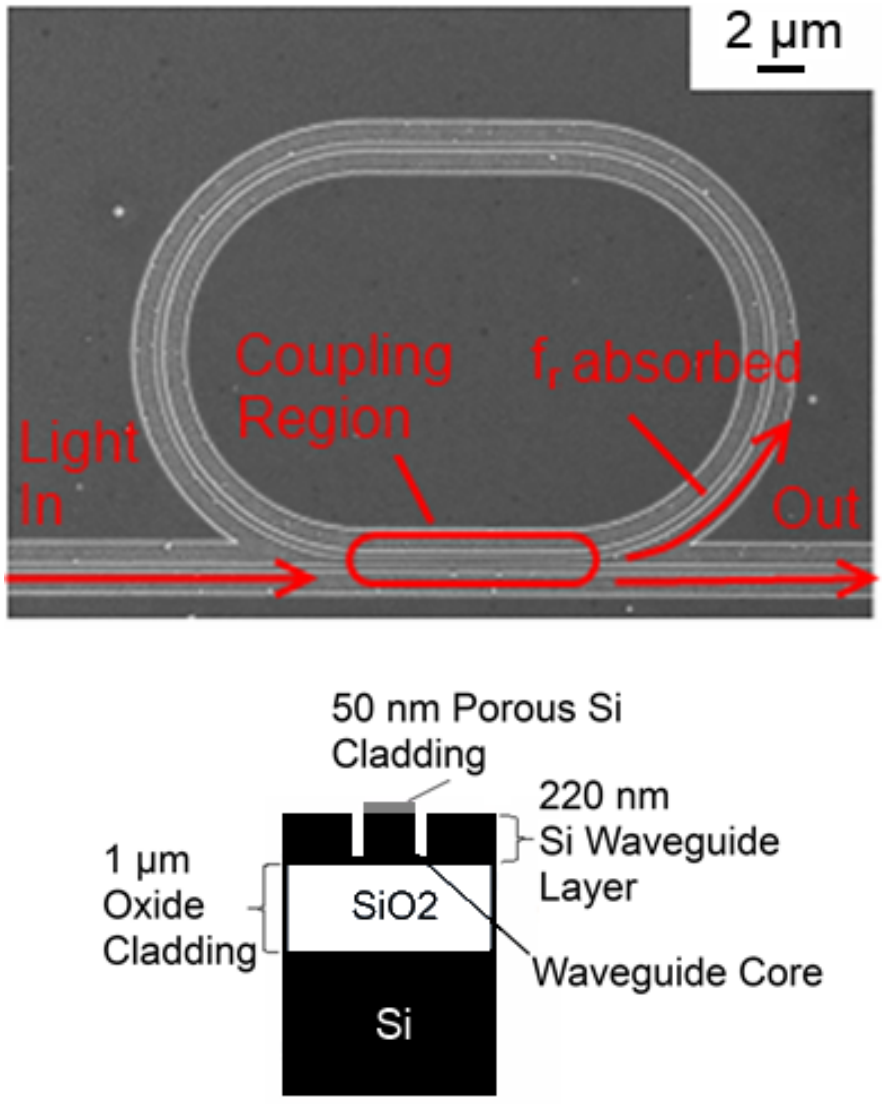


Figure 5.10: Overview of microcavity resonator sensor: (Top) top-down view of device (image provided by Zhixuan Xia), (Bottom) cross-sectional schematic of device with porous Si cladding.

### 5.3.1 Experimental Design - Fabrication of Porous Si Enhanced Microresonator Sensors

5.3.1.1 Overview of Device Fabrication

Development of a magnesiothermic reduction scheme compatible with micropatterned SOI has involved multiple process design iterations. The initial iteration involved first patterning the microresonator devices on SOI, and then applying $Mg(g)/SiO_2$ reduction to a thin (~80 nm) oxide layer grown on the surface of the Si devices, as illustrated in Figure 5.11. This method is referred to as the "pattern-then-react" method. After treatment at 700-800 °C, significant cracking was found in the trenches surrounding the waveguides. It is likely this cracking is the result of Mg attack of the underlying oxide layer, as porous Si can be seen within the cracks (Figure 5.12b). During device fabrication, a 10 nm Si pedestal in the trenches of the waveguide was used to protect the buried oxide from Mg. Unfortunately, it appears this pedestal was not sufficiently thick as to prevent Mg from diffusing to the underlying oxide. Increasing the pedestal thickness past 10 nm would result in a significant leakage of confined light from within the waveguide. Hence, the "pattern-then-react" method was abandoned.

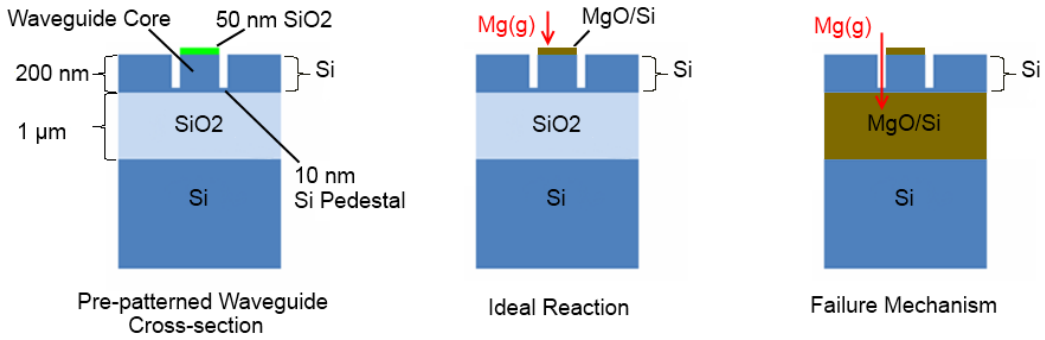


Figure 5.11: Schematic of "pattern-then-react" method applied to patterned SOI specimens: (Left) initial device structure, (Middle) depicting expected ideal results, and (Right) observed failure mechanism.

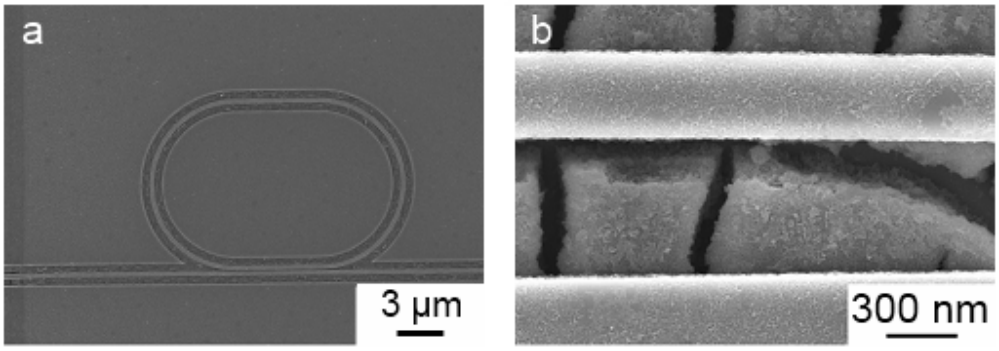


Figure 5.12: Microresonator device fabricated from "pattern-then-react" method: a) top-down SE image of device, b) high-magnification SE image depicting cracking around the waveguide.

In the second iteration, known as the "react-then-pattern" method (Figure 5.13), the surfaces of SOI substrates were first oxidized to form an 80 nm thick $SiO_2$ blanket layer. The oxidized layer was then patterned to form a small "window" of oxide on the surface of the SOI. After Mg(g)/$SiO_2$ reduction, microresonators were patterned in the region of the windows (now composed of porous Si). The result was that porous Si surface layers only existed on the microresonators and the length of the waveguide near

the resonators. The presence of porous Si along the entire external surface of the waveguide would be disadvantageous, as a slight leakage of confined light occurs through the porous Si. When porous Si covers the entire extent of the waveguide, the cumulative leakage could become quite significant. If, however, porous Si is confined to a small area of the device (here the area in the vicinity of the microresonator), the effect of cumulative leakage on light transmittance through the device should be greatly reduced (thus the reason for only converting a small oxide window into porous Si).

This second method was also not successful. Light transmittance through devices obtained by this method was found to be impractically low. As leakage of light could not be detected, a significant absorption of light must have been occurring within the devices. The most likely explanation is that the Mg gas source introduced a significant dopant concentration in the Si waveguides that resulted in a significant reduction in transparency.

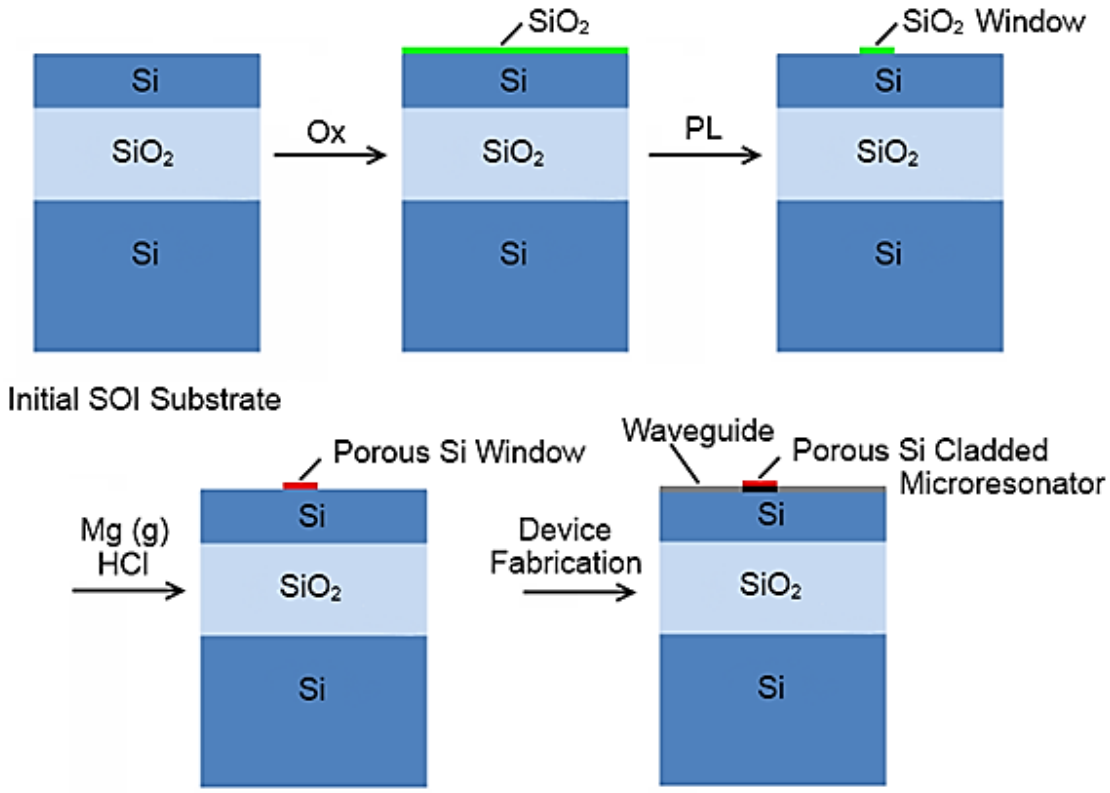


Figure 5.13: Schematic of "react-then-pattern" method depicting device fabrication flow.

The final iteration was a variation of the react-then-pattern method (Figure 5.14), in which a blanket porous Si film was formed (from Mg(g)/$SiO_2$ reduction of a $SiO_2$ blanket film), photolithographically patterned into a porous Si window, and then subjected to device fabrication. A major drawback of this method concerned the transfer of the rough porous Si surface to the surface of the patterned waveguides (Figure 5.15). Surface roughness is expected to introduce some leakage into the waveguides. In practice, however, microresonator devices fabricated through this method were found to have acceptable light transmittance, making sensing measurements possible.

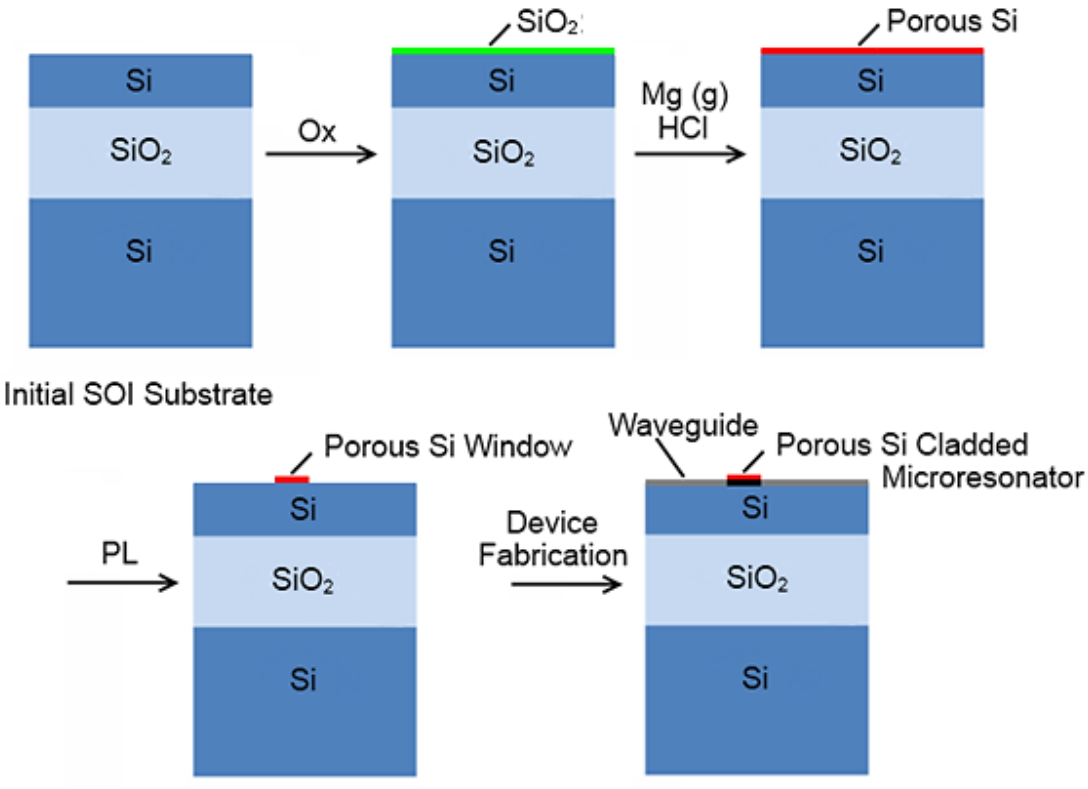


Figure 5.14: Schematic of final iteration of the "react-then-pattern" method depicting device fabrication flow.

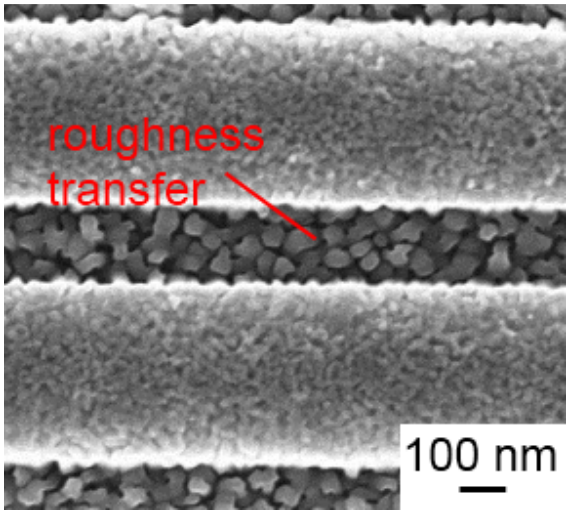


Figure 5.15: Roughness transfer from porous Si blanket film to patterned device.

5.3.1.2 Porous Si Fabrication Procedure

An 80 nm thick thermal oxide was grown on SOI wafers (200 nm Si device layer/1 μm buried oxide, Soitec, Grenoble, France) that were roughly 1 $in.^2$ using dry oxidation in flowing $O_2$ (1000 $cm^3$ $min^{-1}$) at 1050 °C. The thermal oxide films on these samples were subjected to $Mg(g)/SiO_2$ reduction using a similar method to that described in Chapter 2 for quartz wafers. The method developed earlier in this chapter for inverse opals (Figure 5.13) was avoided. As depicted in Figure 5.16, when applied to thermally-oxidized SOI samples, the method presented earlier for inverse opals produced a number of cubic defects on the sample surface. These defects were likely $Mg_2Si$ precursor particles that deposited on and diffusion bonded to the surface of the samples. When the magnesiothermically-treated samples were then subjected to HCl etching, the $Mg_2Si$ particles were dissolved, leaving behind "footprint" indentations in the sample. For patterned optical devices, these indentations produced light scattering that rendered the device nonfunctional.

A method, similar to the "standard" method developed in Chapter 2, that utilized a porous YSZ cloth partition was found to eliminate cubic surface defects in the treated samples (Figure 5.17). Within a 1 $in.^2$ Fe boat, 500 mg of $Mg_2Si$ powder (99.5%, Alfa Aesar, Ward Hill, MA) was loaded and covered with 2 layers of YSZ cloth (Zicar Zirconia, Florida, NY). The aforementioned thermally-oxidized SOI wafers were placed atop the YSZ cloth partition with the oxidized face down. The sample-loaded boat was then inserted into an Fe ampoule and sealed in air. The sample-loaded ampoules were treated at 750 °C for 1 hr to convert the thermal oxide film to MgO/Si. Treatment was conducted by inserting the samples into a preheated furnace and, at the end of treatment,

removing the samples from the furnace and cooling in air to room temperature in the span of 10 mins. After such magnesiothermic treatment, the MgO/Si-coated SOI wafers were then treated in 1 N HCl for 30 s to generate porous Si.

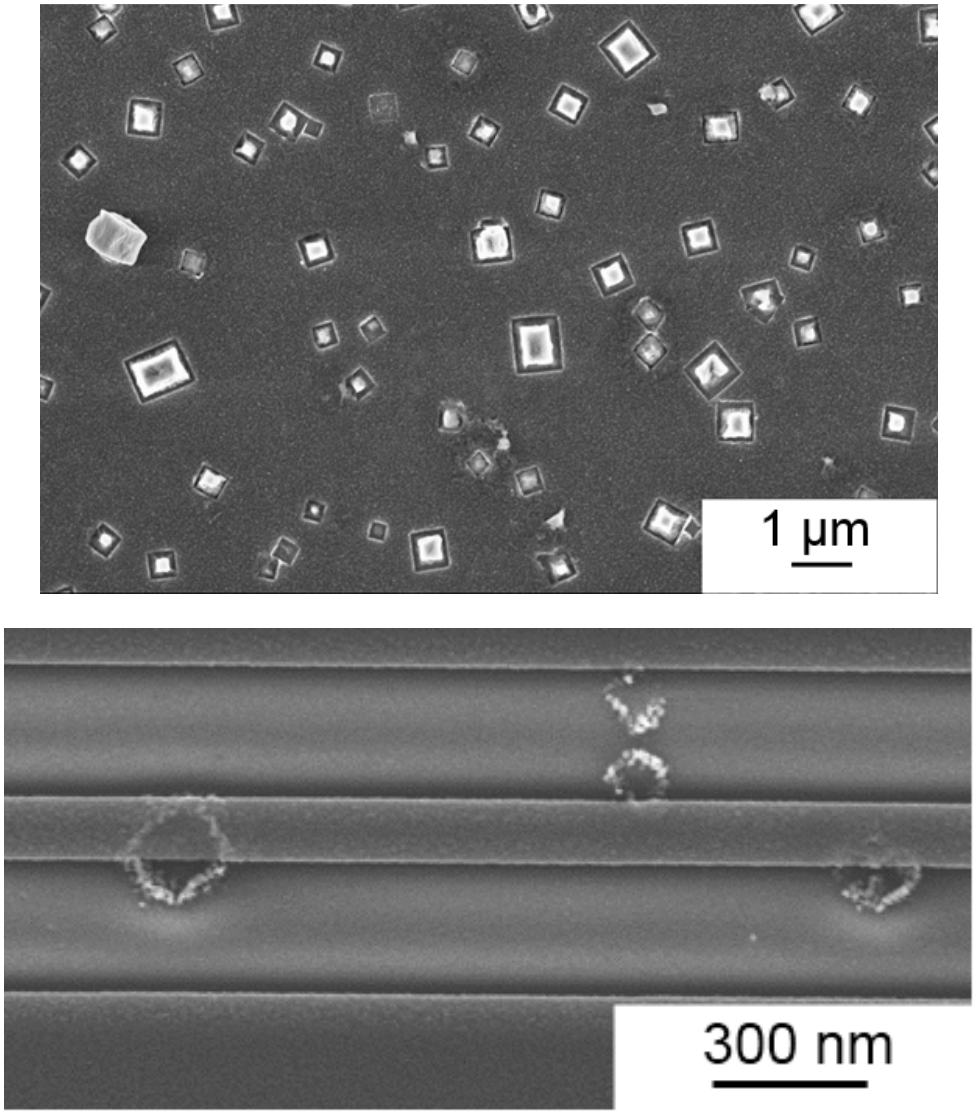


Figure 5.16: (Top) SE images of pervasive cubic defects on SOI wafers magnesiothermically-treated using the method of Figure 5.13, and (Bottom) light scattering from cubic defects on a patterned waveguide. (Bottom image provided by Zhixuan Xia)

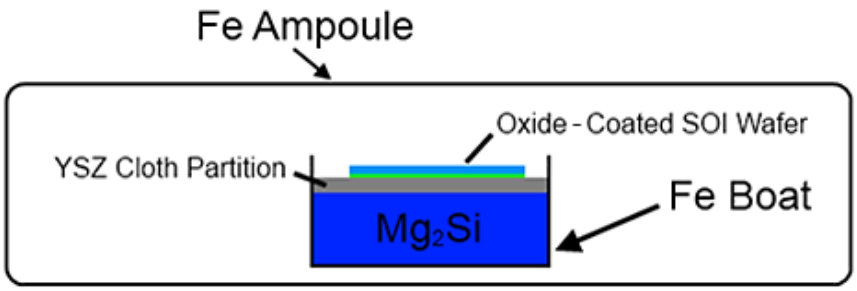


Figure 5.17: Schematic of Mg(g)/$SiO_2$ reduction applied to blanket oxide-coated SOI.

5.3.1.3 Device Fabrication and Testing

The porous Si-coated SOI wafers were spin coated with 750 nm ZEP 520A resist (Zeon Corporation, Tokyo, Japan) and patterned with electron beam lithography at a base dosage of 200 μC $cm^2$ at a 50% modulation. Porous Si and Si were etched via ICP (Plasma Therm, St. Petersburg, FL) with $Cl_2$ gas at a flow rate of 20 $cm^3$ $min^{-1}$. (Device patterning was performed by Zhixuan Xia.)

To test the sensitivity of the devices to adsorbed species, an amino-silanization agent, APTES (Aldrich, St. Louis, MO), was functionalized to the surface of the patterned sensors. APTES functionalization was accomplished by treating the devices in a 4 vol.% APTES solution (4 parts APTES, 46 part MeOH, 50 part $H_2O$) for 24 hrs. The APTES was used to provide a selective functionality (a primary amine) to capture carboxylic acid containing biomolecule analytes. Here, biotin was used as an analyte. NHS-Biotin (Thermo Fisher Scientific, Rockford, IL) was dissolved in dry DMSO to form a 1 mg $ml^{-1}$ solution. APTES-functionalized devices were then treated in the NHS-biotin solution for 24 hrs.

For sensing tests, a tunable laser (81640A, Agilent Technologies, Santa Clara, CA) operating in the 1460-1580 nm wavelength range was coupled via fiber optic cable to the input waveguide of the device. The absorption spectra were taken at the output with an InGaAs photoreceiver (PDB 150C, Thorlabs, Newton, NJ). (Sensing tests were performed by Zhixuan Xia.)

5.3.1.4 Sample Chracterization

XRD patterns were obtained using an X'Pert MRD diffractometer (PANalytical, Almelo, the Netherlands) in glancing angle mode with a fixed 0.5° incident angle. The diffractometer was configured with a Cu $K_\alpha$ radiation source, with a Cu parabolic mirror in the incident beam path and a 0.09° parallel plate collimator in the diffracted beam path. SE images were taken with a LEO 1530 FE-SEM (Carl Zeiss AG, Oberkochen, Germany) at an accelerating voltage of 15 kV.

### 5.3.2 Results and Discussion

GIXRD analysis of magnesiothermically-treated MgO/Si-coated SOI wafers is shown in Figure 5.18. Both MgO and polcrystalline Si peaks were present. For the polycrystalline Si phase, the Si primary {222} peak was not present. Instead, the Si {200} peak was found, which corresponded to the orientation of the Si substrate, implying an epitaxial relationship between the polycrystalline porous Si and the substrate. The relative shift between the porous, polycrystalline Si and the single-crystal Si substrate can be explained by differing stress states between the film and substrate. The expansion of the MgO/Si product film over the initial $SiO_2$ film should place that film in

a state of compression, which corresponds to the shift in the polycrystalline Si peak to a higher 2θ value in glancing angle mode. The underlying Si substrate must then be in a state of tension, which corresponds to a shift to a lower 2θ value in glancing angle mode. The MgO peak was found to disappear after treatment in 1 N HCl for 10 s. Scherrer analysis yielded a MgO crystallite size of 28 nm and a Si crystallite size of 12 nm.

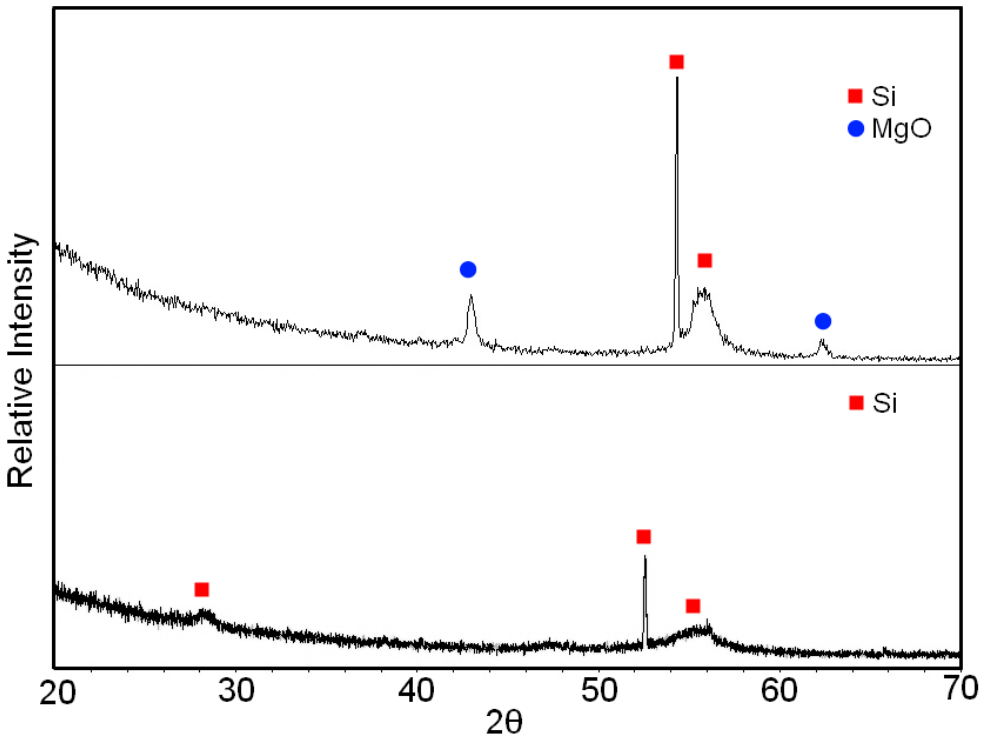


Figure 5.18: XRD analysis of magnesiothermically-reacted $SiO_2$-coated SOI: (Top) MgO/Si product film after reaction, and (Bottom) porous Si product film after treatment in 1N HCl for 10 mins.

Top-down SE images of porous Si blanket films on SOI are shown in Figure 5.19. A complex randomly-oriented porous network is seen. From top-down imaging, the average pore size is estimated to be ~30 nm, which corresponds to the average MgO

crystallite size found by Scherrer analysis for samples reacted at 750 °C for 1 hr (Figure 5.19a). Porous Si fabricated via $Mg(g)/SiO_2$ reduction at 850 °C for 1 hr is shown in Fig. 5.19b. At 850 °C, the pores were found to be slightly coarser (estimated to be ~50 nm), demonstrating a weak dependence of pore size on $Mg(g)/SiO_2$ reduction temperature.

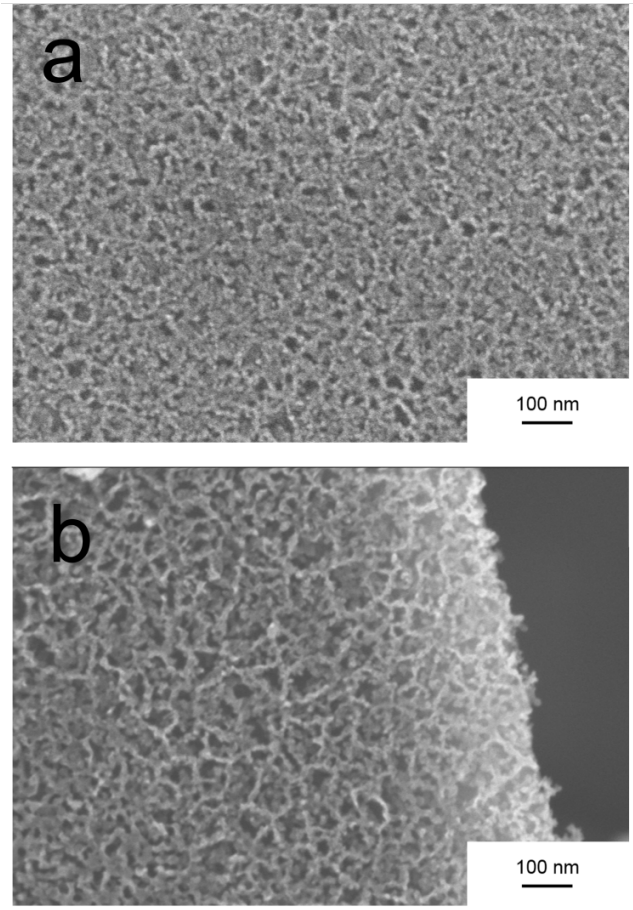


Figure 5.19: Top-down SE images of porous Si films on SOI fabricated at: a) 750 °C, and b) 850 °C. (Provided by Dr. Murtaza Askari)

Images of a fabricated porous Si-cladded racetrack microresonator device are shown in Figure 5.20. The surface layer of porous Si was clearly maintained during

device patterning. A thickening of the porous cladding is seen after device fabrication, expanding from 80 nm $SiO_2$ to 125.8 nm porous Si. Light transmission was achievable in the patterned waveguides with an estimated loss of 35 dB $cm^{-1}$.

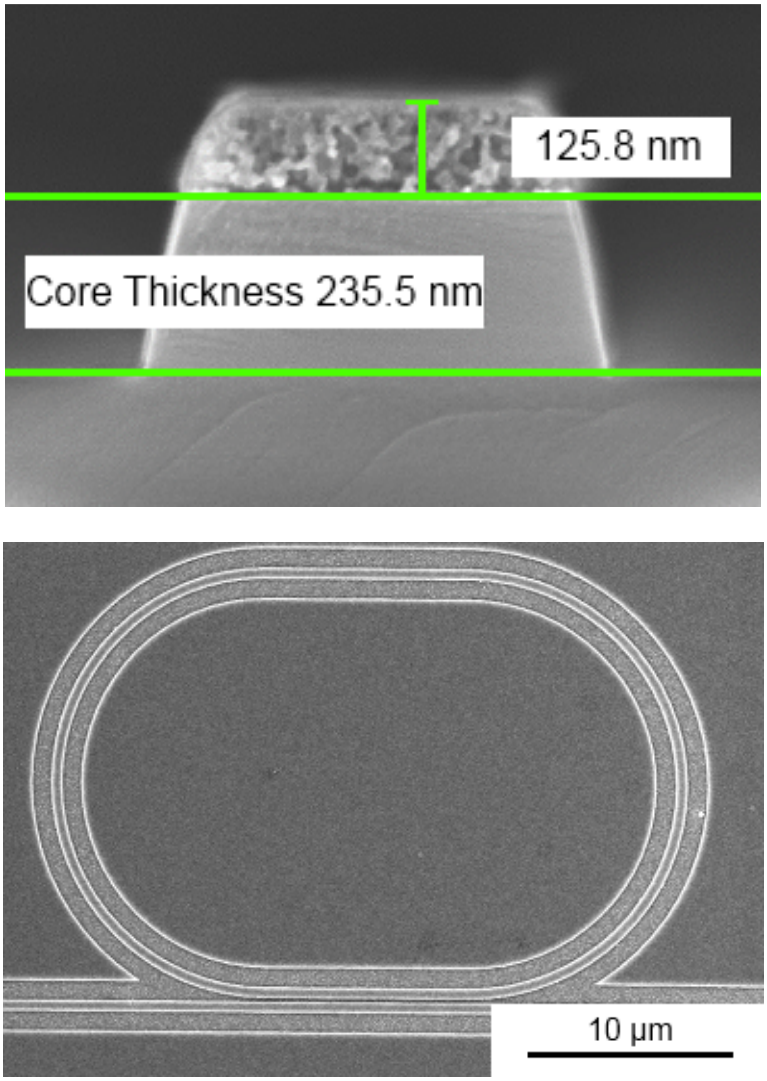


Figure 5.20: Porous Si-cladded microresonator device: (Top) cross-sectional image of porous Si-cladded waveguide, and (Bottom) top-down image of microresonator device. (Provided by Zhixuan Xia)

The surfaces of the patterned devices were treated with APTES, an amino-silanization agent. The terminal amine present on this molecule may be used to bind a number of biomolecule analytes possessing unprotected carboxylic acid groups via succinimide chemistry. A shift in the resonance frequency ($f_r$) of the microresonator occurred after APTES adsorption, providing proof of chemical sensing capabilities. When comparing porous Si-enhanced devices to devices with only planar Si surfaces, the porous Si-enhanced devices were measured to have a greater shift in $f_r$ by a factor of 5.81, demonstrating that the higher surface area offered by porous Si led to a significant increase in sensitivity (Figure 5.21).

APTES functionalization can be used as a means to generate selective adsorption of a number of carboxylic acid containing molecules. Here, the biomolecule biotin was used to demonstrate the sensing of a biomolecule analyte. Upon biotin adsorption, a significant advantage in sensing is found in the porous Si-cladded devices over planar Si devices (Figure 5.22). For the porous Si-cladded devices, $f_r$ shift is improved by a factor of 6.50. The more exaggerated shift present in the porous Si-cladded devices means these devices are more sensitive and would allow for the detection of smaller concentrations of analyte.

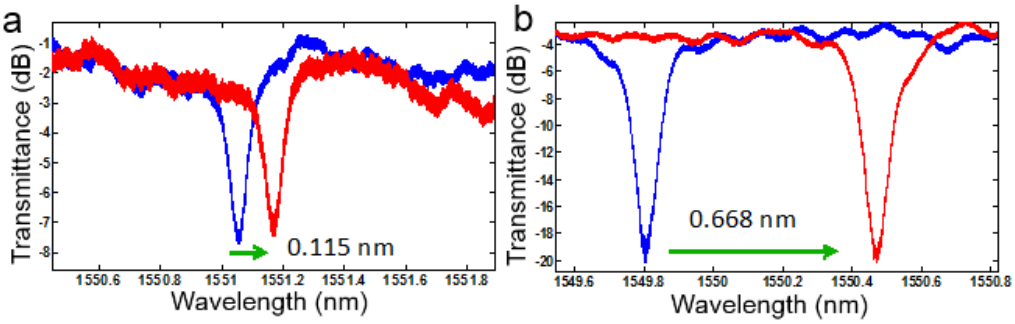


Figure 5.21: Microresonator absorption shift after APTES functionalization: a) planar Si surface device (control), and b) porous Si-cladded device. (Blue indicates initial absorption spectra, red indicates absorption spectra after APTES functionalization.)

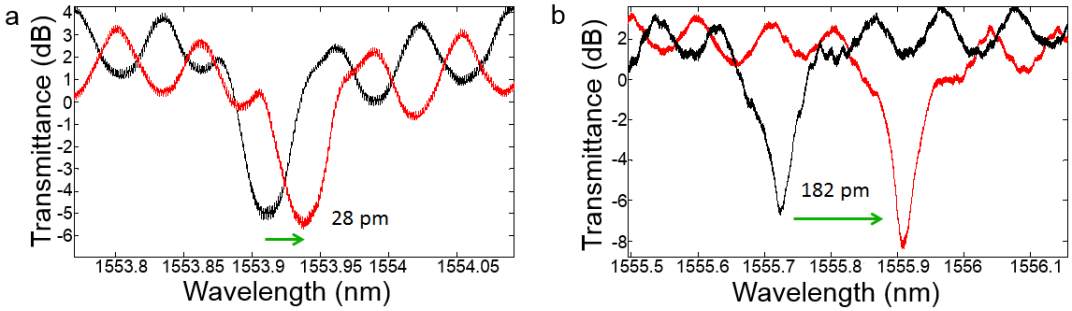


Figure 5.22: Microresonator absorption shift after biotin incubation with APTES functionalized devices: a) planar Si surface device (control), and b) porous Si-cladded device. (Black indicates initial absorption spectra, red indicates absorption spectra after biotin adsorption.)

## 5.4 Summary

Mg(g)/$SiO_2$ reduction was used to fabricate porous Si-enhanced optical and photonic devices from $SiO_2$ templates. The IR transparency and high refractive index of Si make this material attractive for such applications[82b]. The high surface area of porous Si makes it particularly attractive for optical chemical sensing applications. Gas-solid shape-preserving chemical conversions were used to convert $SiO_2$ inverse opal structures into replicas of anatase $TiO_2$, MgO/Si, and porous Si. The inverse opal structure was

well retained after these conversions. $TiO_2$ and MgO/Si replicas showed a significantly higher refractive index than the $SiO_2$ template material, while porous Si had a significantly higher surface area. Optical microresonator chemical sensors were enhanced with porous Si cladding using $Mg(g)/SiO_2$ reduction. Fabrication of these devices started by first converting blanket films of thermally-grown $SiO_2$ on SOI substrates to porous Si. The porous Si blanket films were then etched to cover only a small region of the substrate, and microcavity resonators were patterned into the dense Si device layer beneath these windows of porous Si. Porous Si enhanced microresonator sensors exhibited a ~6 times greater sensitivity to an adsorbed analyte species than sensors without the porous Si modification.

# CHAPTER 6:

# CONCLUSIONS AND OUTLOOK

This work has provided a further refinement to the foundation of $Mg(g)/SiO_2$ reduction. New observations and descriptions have been put forth regarding details central to the reaction progression relating to the development of a shape-retaining product morphology of MgO/Si that is sufficiently resilient to survive removal of the MgO product (which accounts for ~65 vol.% of the product). Both product morphology evolution and stress relaxation mechanisms have been elucidated here. A mechanism for the growth of an interwoven, highly robust two-phase composite of MgO/Si products from silica subjected to $Mg(g)/SiO_2$ reduction has been presented here. As magnesium gas is capable of reducing almost all metal oxides, magnesiothermic reduction may be applied to a wide range of other metal oxide templates to generate porous metal replicas. Criteria can be constructed based on the analysis of Chapter 2 to determine if a metal oxide template can be converted into a porous metal replica via a magnesiothermic reduction process:

1) An aggregate product morphology must be formed during reduction – Following the original analysis of solid-state reduction by Rapp, et al.[17], the diffusion of O across the reduced metal must be slower than $Mg^{2+}$ diffusion across the MgO product.

2a) The MgO-$Me_\upsilon$O-Me-Mg phases must possess mutual solid solubility– To support the formation of an interwoven composite, complex composition gradients must be present ahead of the reaction front, as described by Tangchitvittaya, et al.[21].

2b) A metastable intermediate phase which can support a range of chemical compositions must form between the final products and the solid reactant– As demonstrated in Chapter 2, an intermediate layer separating the solid products from the solid reactant can produce an interwoven product morphology if that intermediate layer can support complex composition gradients ahead of the growing MgO/reduced metal phases.

The first criteria must always be satisfied to generate a porous metal replica of the starting oxide template. However, only one of the second criteria must be satisfied to obtain the desired results. As an example, Ni is a widely used catalytic metal in organic chemistry[95]. Magnesiothermic reduction of NiO to generate porous Ni may be accomplished to the satisfaction of criteria 1 and 2a (NiO and MgO display a high degree of solid solubility[96]). On the other hand, for the case of Ge, criteria 2b is likely possible, opening up the possible creation of porous Ge for photonic and optical applications.

The exploration of applications of Mg(g)/$SiO_2$ reduction has been further expanded in the present work. A sequence of reactions to convert porous Si diatom frustule replicas generated from $SiO_2$ into replicas of high surface area C was presented. These reactions build upon the macroporosity of silica templates and the mesoporosity generated during Si conversion by introducing a large volume of micropores to the C replica structure. The end result is a porous C structure that is both high in surface area and hierarchically porous. The hierarchical porosity present in these C replicas has advantages in catalysis, as micro-/mesoporosity offers a high surface area for loading of catalytic sites, while the larger macropores offer a rapid diffusion pathway for reactant and product species.

It was shown that C replicas of diatomaceous earth could be loaded with catalysts relevant to a number of applications. C diatom replicas were loaded with Pt via a gas impregnation method, and the catalytic activity of oxygen reduction was tested. Pt-loaded C diatom replicas displayed a significantly greater catalytic activity than C controls that lacked the hierarchical porosity and hollow, thin-walled nature of these biogenic samples. Similarly, C diatom replicas were loaded with a model enzyme, glucose oxidase, and tested in a flow-through reactor. The glucose decomposition facilitated by this enzyme was found to occur at a significantly faster rate for diatom-derived samples than for other enzyme-loaded C controls. When the glucose decomposition rate was normalized to the mass of loaded enzyme, C diatom replicas displayed similar performance to enzyme-loaded $SiO_2$ diatoms, demonstrating the advantages of the hierarchically-porous, hollow, thin-walled diatom frustule structure. As Si diatom replicas served as a template for the fabrication of C diatom replicas, C diatom replicas can also be used as a template for replicas of alternative functional materials. In this work, a series of aqueous electroless reactions were demonstrated that converted C diatom replicas into replicas of an Au-bearing $SnO_2$ composite. Flow-through testing of glucose oxidase-loaded Au-bearing diatom replicas revealed a similar performance advantage over an Au control. Glucose decomposition rates normalized to enzyme loading were in-line with that measured for $SiO_2$ and C diatom samples, again reinforcing the utility of the diatom frustule structure in flow-through catalysis. This work creates motivation for further exploration of diatom supports for a number of technologically important enzyme systems.

Previously, porous Si fabrication by magnesiothermic reduction had been largely confined to complex $SiO_2$ particles. In this work, magnesiothermic reduction was extended to films of $SiO_2$ (inverse opals and surface-oxidized SOI) for use in optical and photonics applications. A porous Si cladding produced by magnesiothermic reduction was shown to provide sensing enhancement to integrated optical microcavity resonators. A large (factor of ~6) increase in resonance shift was found after the adsorption of a biomolecule analyte on resonators enhanced with porous Si cladding. The implication of such enhancement is that significantly smaller concentrations of analyte may be detected by such sensors.

The hope for this work is that a foundation has been provided for continued exploration of applications of magnesiothermic reduction. The applications studied here provide basic proofs of the utility of this method in both catalysis and chemical sensing. Going forward, further work should expand upon catalysts and analytes utilized in these porous Si and C structures, as there are many technologically significant opportunities awaiting investigation.

**APPENDIX A:**

**FURNACE TEMPERATURE PROFILE**

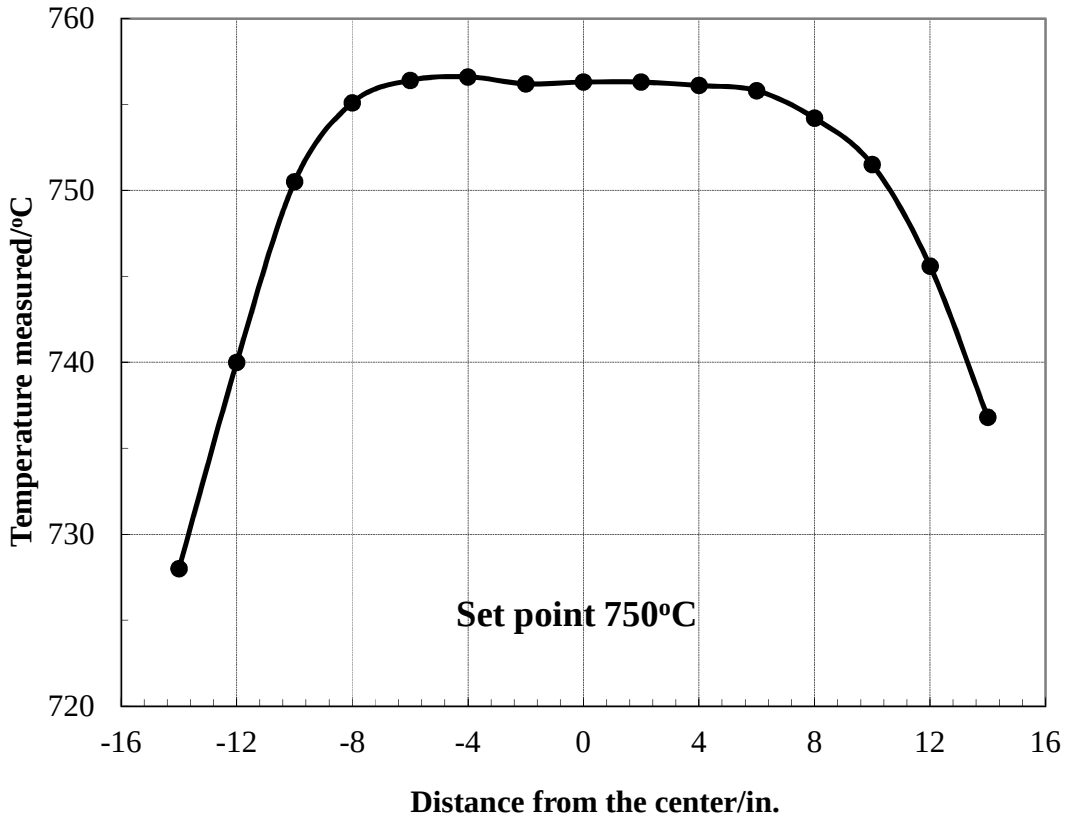


Figure A.1: Temperature profile of horizontal tube furnace used for silica magnesiothermic reduction at a set point of 750 °C. Samples were treated in the area extending 6 in. from either side of the center.

## APPENDIX B:

## THEORETICAL CORRELATION OF PRODUCT FILM RESIDUAL STRESS AND OVERLAYER GROWTH DURING ANNEALING OF MAGNESIOTHERMICALLY-REDUCED QUARTZ

To analyze the relationship between MgO overlayer thickness and residual stress in the MgO/Si product layer after annealing of magnesiothermically-reduced quartz (Chapter 3), the dimensions of the unconstrained MgO/Si product layer ($D_x$, $D_y$, and $D_z$ shown in Figure B.1) are determined from the measured residual stress state in the product film. The product layer is assumed to behave elastically according to Hooke's Law:

$$\sigma = E\epsilon \tag{B.1}$$

where σ is the stress in the product layer, E is the elastic modulus, and $\epsilon$ is the strain in the product film. Strain is given by:

$$\epsilon = \frac{l - l_0}{l_0} \tag{B.2}$$

where l is a dimension of the product film under stress and $l_0$ is the dimension unstressed. Combining B.1 and B.2 shows that:

$$l_0 = \frac{l}{1 + \frac{\sigma}{E}} \tag{B.3}$$

Equation B.3 may be used to determine the values $D_x$ and $D_z$ shown in Figure B.1 with knowledge of σ and E. (The value of $l$ is known from the dimensions of the quartz substrate.)

The volume of the MgO overlayer film is given by:

$$V_{ov} = d_x d_y d_z \tag{B.4}$$

where $d_x$, $d_y$, and $d_z$ are the dimensions shown in Figure B.1. Movement of this volume into the product layer, as shown in Figure B.2, will extend the unconstrained dimensions $D_x$ and $D_z$ by $D'_x$ and $D'_z$. As changes in the product layer thicknesses have not been observed after annealing, the volume is not assumed to extend $D_y$ (Table B.1). From this configuration, it can be seen that:

$$V_{ov} = \left(D_y D_x D'_z\right) + \left(D_y D_z D'_x\right) + \left(D_y D'_x D'_z\right) \tag{B.5}$$

Assuming biaxial symmetry in the product layer means that:

$$D_x = D_z \tag{B.6}$$

$$D'_x = D'_z$$

$$d_x = D_x$$

$$d_z = D_z$$

Combining equations B.4, B.5, and B.6 yields:

$$d_y = \left(\frac{D_y}{D_x^2}\right)\left[2\left(D_x D'_x\right) + \left(D'^2_x\right)\right] \tag{B.7}$$

From equation B.7, an overlayer thickness ($d_y$) can be predicted from $D_x$ values measured from the residual stress state (via XRD) in the product layer (using equation B.3) and the measured $D_y$ value (measured via SE cross-sectional images determined to be 800 nm).

$D_x$ of the product film before overlayer growth occurs ($D°_x$) can be used to calculate $D'_x$. Experimentally, this is difficult obtain, since the crystallization of the underlying amorphous Mg silicate layer, which occurs during annealing, appears to increase the residual stress in the MgO/Si product layer. However, as demonstrated in

Figure B.3, there is observed a linear relationship between $D_x$ and the MgO overlayer thickness. Extrapolating to the point of no overlayer growth gives a residual stress of -8.44 GPa and a $D°_x$ value of 1.030 cm. $D°_x$ and the measured $D_x$ value at each annealing point can be used to determine the value of $D'_x$ by:

$$D'_x = D°_x - D_x \tag{B.8}$$

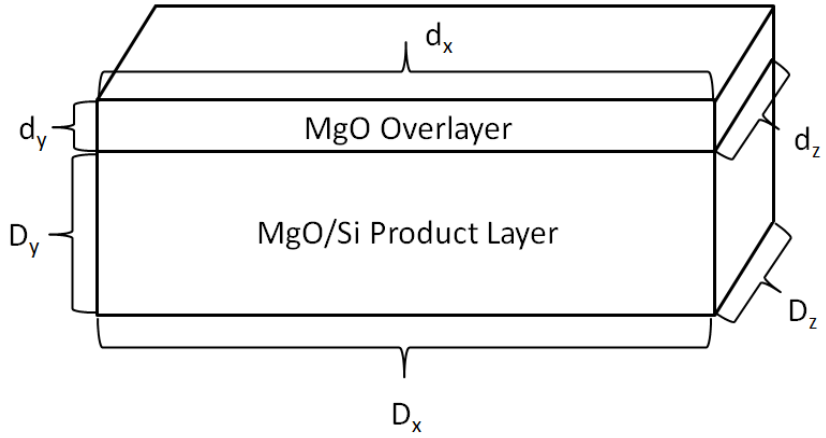


Figure B.1: Schematic of a MgO/Si product layer and a MgO overlayer unconstrained by a quartz substrate.

Table B.1: Measured MgO/Si layer thicknesses as a function of annealing time.

| Annealing Time (hrs) | MgO/Si Product Layer Thickness (nm) |
|---|---|
| 0 | 799 ± 198 |
| 2 | 560 ± 15 |
| 5 | 673 ± 18 |
| 10 | 500 ± 46 |
| 15 | 760 ± 24 |
| 24 | 846 ± 59 |

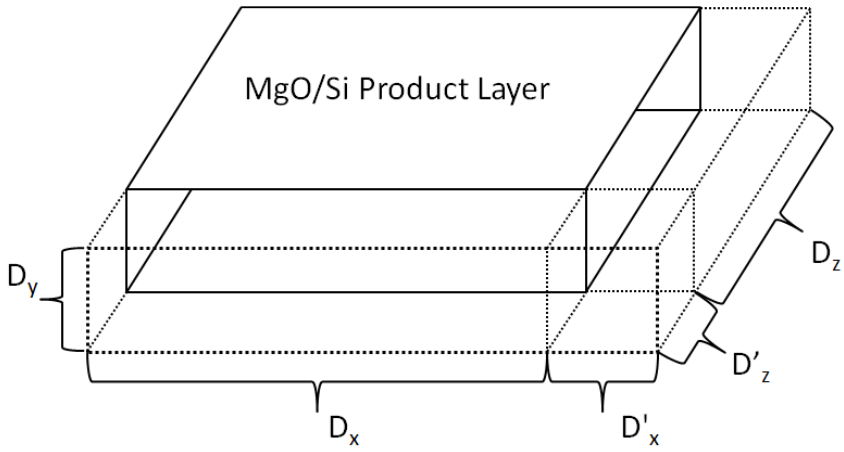


Figure B.2: Schematic of the volume expansion of a MgO/Si product layer when the MgO overlayer volume is incorporated into the product layer in-plane. Dashed lines indicate added volume.

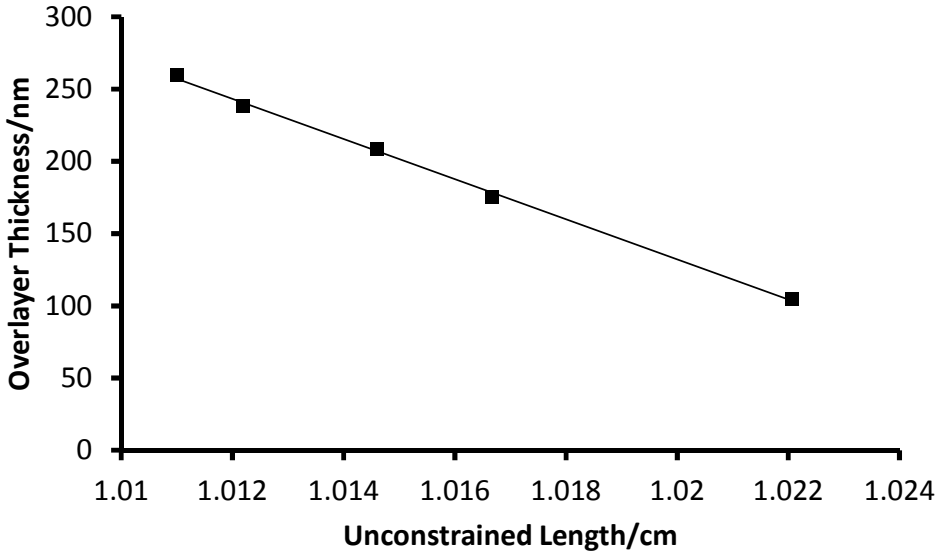


Figure B.3: Measured MgO overlayer thickness as a function of the unconstrained length of annealed MgO/Si product layers determined from XRD residual stress measurements. $R^2$ of trendline is 0.9978.

The predicted and measured MgO overlayer thicknesses after annealing of the MgO/Si product films are shown in Table B.2 and compared in Figure B.4. The calculated $d_y$ values obtained from equation B.7 are for an overlayer film on a product layer not constrained by a substrate. For comparison with measured $d_y$ values in Table B.1, the results of equation B.7 were adjusted by the following equation in Table B.2:

$$\epsilon_y = \left(\frac{1}{E}\right)[-\nu(\sigma_x + \sigma_z)] \tag{B.9}$$

The values of E, ν, and $\sigma_x$ (which is assumed to be equivalent to $\sigma_z$ under the biaxial assumption) for MgO are given in Chapter 3. The ratio of the predicted to measured values is ~8.7. Power law fittings of the predicted and measured overlayer thicknesses as a function of annealing time are shown in Table B.3, where it is seen that the predicted and measured values follow a similar trend.

Table B.2: Predicted and measured MgO overlayer thicknesses after annealing of MgO/Si product films on quartz.

| Annealing Time (hrs) | $D_x$ (cm) | $D'_x$ (cm) | Predicted $d_y$ (nm) | Measured $d_y$ (nm) | Ratio Measured:Predicted |
|---|---|---|---|---|---|
| 2 | 1.022 | 0.007485 | 11.86 | 105 | 8.9 |
| 5 | 1.017 | 0.01289 | 20.54 | 175 | 8.5 |
| 10 | 1.015 | 0.01496 | 23.90 | 209 | 8.7 |
| 15 | 1.012 | 0.01737 | 27.82 | 238 | 8.6 |
| 24 | 1.011 | 0.01856 | 29.76 | 260 | 8.7 |

Table B.3: Power law fittings of measured and predicted MgO overlayer thicknesses as a function of annealing time.

| | Power Law Fitting | $R^2$ |
|---|---|---|
| Predicted | $d_y = 10.1t^{0.366}$ | 0.943 |
| Measured | $d_y = 88.3t^{0.361}$ | 0.957 |

While the predicted and measured rates of overlayer growth agree, the large difference in magnitude (a factor of ~8.7) implies that MgO in the overlayer film is less dense than in the product layer. One possible source of this error comes from the porosity of the MgO overlayer. The MgO overlayer is not fully dense, as is assumed in the derivation of B.7. If the entire difference in magnitude between measured and predicted thicknesses is attributed to overlayer porosity, then the overlayer would need to be 88% porous. Another possible source of error may come from difference in purity between the MgO in the product layer and in the overlayer (e.g., differing Si doping concentrations).

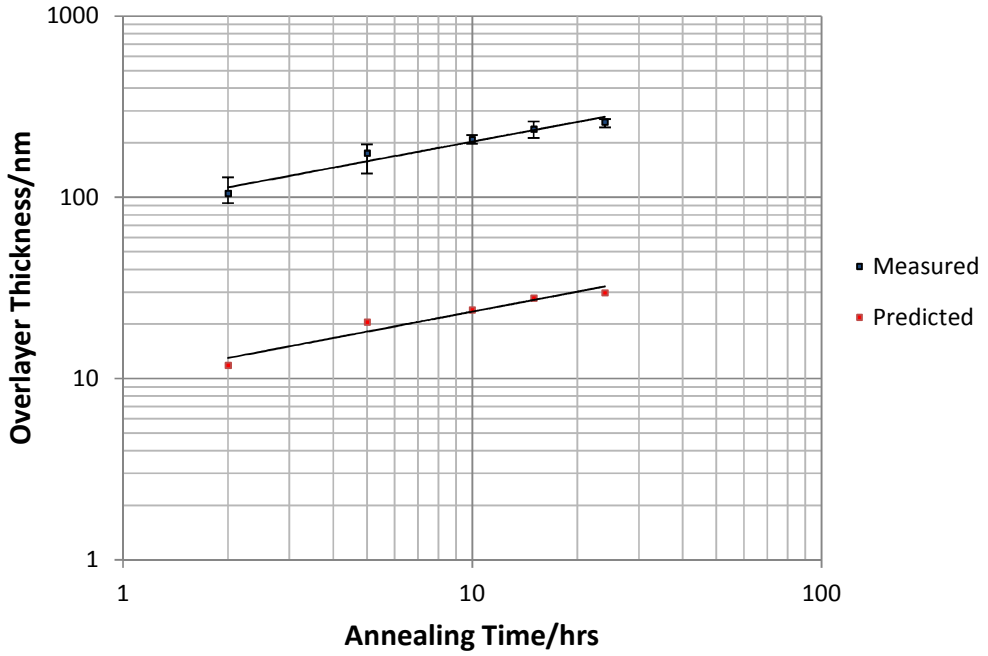


Figure B.4: Comparison of measured and predicted MgO overlayer thicknesses as a function of annealing time. Predicted values are based on measured product layer residual stresses. $R^2$ of the trendline for the measured data is 0.957, and 0.943 for the predicted data.

## REFERENCES


[1] a) R. R. Unocic, F. M. Zalar, P. M. Sarosi, Y. Cai, K. H. Sandhage, *Chem. Commun.* **2004**, 796; b) J. Zhao, C. S. Gaddis, Y. Cai, K. H. Sandhage, *Journal of Materials Research* **2005**, *20*, 282–287; c) S. Dudley, T. Kalem, M. Akinc, *Journal of the American Ceramic Society* **2006**, *89*, 2434–2439.

[2] L. T. Canham, *Applied Physics Letters* **1990**, *57*, 1046–1048.

[3] L. T. Canham, *Advanced Materials* **1995**, *7*, 1033–1037.

[4] J. Llorca, A. Casanovas, T. Trifonov, A. Rodríguez, R. Alcubilla, *Journal of Catalysis* **2008**, *255*, 228–233.

[5] U. Kasavajjula, C. Wang, A. J. Appleby, *Journal of Power Sources* **2007**, *163*, 1003–1039.

[6] a) A. Uhlir, *Bell Syst. Tech. J.* **1956**, *35*, 333; b) D. R. Turner, *J. Electrochem. Soc.* **1958**, *105*, 402–408.

[7] Z. Huang, N. Geyer, P. Werner, J. de Boor, U. Gösele, *Advanced Materials* **2011**, *23*, 285–308.

[8] a) Z. Bao, M. R. Weatherspoon, S. Shian, Y. Cai, P. D. Graham, S. M. Allan, G. Ahmad, M. B. Dickerson, B. C. Church, Z. Kang, H. W. A. Iii, C. J. Summers, M. Liu, K. H. Sandhage, *Nature* **2007**, *446*, 172–175; b) K. H. Sandhage, Z. Bao, Methods of fabricating nanoscale-to-microscale structures **2009**.

[9] E. K. Richman, C. B. Kang, T. Brezesinski, S. H. Tolbert, *Nano Lett.* **2008**, *8*, 3075–3079.

[10] Allan, S. M., Master's Thesis, Georgia Institute of Technology, **2005**.

[11] a) J. Moon, S. Yang, *Journal of Macromolecular Science: Polymer Reviews* **2005**, *45*, 351–373; b) G. Subramanian, V. N. Manoharan, J. D. Thorne, D. J. Pine, *Advanced Materials* **1999**, *11*, 1261–1265.

[12] a) W. Chen, Z. Fan, A. Dhanabalan, C. Chen, C. Wang, *J. Electrochem. Soc.* **2011**, *158*, A1055–A1059; b) M. Guo, X. Zou, H. Ren, F. Muhammad, C. Huang, S. Qiu, G. Zhu, *Microporous and Mesoporous Materials* **2011**, *142*, 194–201; c) D. P. Wong, H.-T. Lien, Y.-T. Chen, K.-H. Chen, L.-C. Chen, *Green Chemistry* **2012**, *14*, 896; d) K. Chen, Z. Bao, J. Shen, G. Wu, B. Zhou, K. H. Sandhage, *J. Mater. Chem.* **2012**, *22*, 16196–

16200; e) B. Zhao, H. Zhang, H. Tao, Z. Tan, Z. Jiao, M. Wu, *Materials Letters* **2011**, *65*, 1552–1555.

[13] a) Y. C. Chen, J. Xu, X. H. Fan, X. F. Zhang, L. Han, D. Y. Lin, Q. H. Li, C. Uher, *Intermetallics* **2009**, *17*, 920–926; b) I. Gutman, L. Klinger, I. Gotman, M. Shapiro, *Solid State Ionics* **2009**, *180*, 1350–1355.

[14] a) S. F. Hulbert, G. Lane, *Transactions of the British Ceramic Society* **1968**, *67*, 391–395; b) R. Abart, E. Petrishcheva, F. D. Fischer, J. Svoboda, *Am J Sci* **2009**, *309*, 114–131; c) E. Gardés, B. Wunder, K. Marquardt, W. Heinrich, *Contributions to Mineralogy and Petrology* **2012**, *164*, 1–16; d) R. A. Yund, *Contributions to Mineralogy and Petrology* **1997**, *126*, 224–236; e) G. W. Brindley, R. Hayami, *Philosophical Magazine* **1965**, *12*, 505–514; f) R. Milke, R. Dohmen, H.-W. Becker, R. Wirth, *Contributions to Mineralogy and Petrology* **2007**, *154*, 519–533; g) Milke, Wiedenbeck, Heinrich, *Contributions to Mineralogy and Petrology* **2001**, *142*, 15–26.

[15] I. R. Wynnyckyj, D. Rao, *High Temperature Science* **1976**, *8*, 203–217.

[16] a) I. Gutman, L. Klinger, I. Gotman, M. Shapiro, *Solid State Ionics* **2009**, *180*, 1350–1355; b) Y. C. Chen, J. Xu, X. H. Fan, X. F. Zhang, L. Han, D. Y. Lin, Q. H. Li, C. Uher, *Intermetallics* **2009**, *17*, 920–926.

[17] R. Rapp, A. Ezis, G. Yurek, *Metallurgical and Materials Transactions B* **1973**, *4*, 1283–1292.

[18] G. Yurek, R. Rapp, J. Hirth, *Metallurgical and Materials Transactions B* **1973**, *4*, 1293–1300.

[19] H. Yuan, R. S. Williams, *Chem. Mater.* **1990**, *2*, 695–700.

[20] Data compiled from Barin, I. *Thermochemical Data of Pure Substances*; 3rd ed.; Weinheim: New York, 1995 with modifications introduced by Gourishankar, K.; Karaminezhad, R.; Pierre, G. *Journal of Phase Equilibria* **1993**, *14*, 601-611.

[21] C. Tangchitvittaya, J. P. Hirth, R. A. Rapp, *Metallurgical Transactions A* **1982**, *13*, 585–594.

[22] C. Wagner, *Z. Phys. Chem.*, **1936**, *B32*, pp. 447-62.

[23] a) D. R. Sempolinski, W. D. Kingery, *Journal of the American Ceramic Society* **1980**, *63*, 664; b) D. R. Sempolinski, W. D. Kingery, H. L. Tuller, *Journal of the American Ceramic Society* **1980**, *63*, 669.

[24] a) Powder Diffraction File, Card No. 01-070-9183 for MgO; b) Card No. 01-070-5680 for Si (International Center on Diffraction Data, Newtown Square, PA).

[25] a) R. C. Newman, *Defect and Diffusion Forum* **1997**, *143-147*, 993; b) J. C. Mikkelsen, *MRS Online Proceedings Library* **1985**, *59*.

[26] a) White, G. *Journal of Physics C: Solid State Physics* **1972**, *5*, 2731-2745; b) G. Bayer *Proceedings of the British Ceramic Society*, **1973**, *22*, 39-53; c) Lyon, K.; Salinger, G.; Swenson, C.; White, G. *Journal of Applied Physics* **1977**, *48*, 865-868.

[27] E. Gardés, W. Heinrich, *Contrib Mineral Petrol* **2011**, *162*, 37.

[28] a) F. J. M. Rietmeijer, J. A. Nuth, I. D. R. Mackinnon, *Icarus* **1986**, *66*, 211–222; b) K. L. Day, B. Donn, *The Astrophysical Journal* **1978**, *222*, L45–L48.

[29] A. L. Greer, N. Karpe, J. Bøttiger, *Journal of Alloys and Compounds* **1993**, *194*, 199–211.

[30] R. B. Schwarz, W. L. Johnson, *Phys. Rev. Lett.* **1983**, *51*, 415.

[31] X. G. Li, A. Chiba, S. Takahashi, *Journal of Applied Physics* **1997**, *81*, 2895–2897.

[32] a) H. Shin, M. Agarwal, M. R. De Guire, A. H. Heuer, *Journal of the American Ceramic Society* **1996**, *79*, 1975–1978; b) J. D. DeLoach, J. J. Shibilski, C. R. Crape, C. R. Aita, *Journal of Vacuum Science & Technology A: Vacuum, Surfaces, and Films* **2000**, *18*, 2922–2927; c) F. Paumier, R. J. Gaboriaud, *Thin Solid Films* **2003**, *441*, 307–310; d) P. Ahmet, T. Koida, M. Takakura, K. Nakajima, M. Yoshimoto, H. Koinuma, M. Tanaka, M. Takeguchi, T. Chikyow, *Applied Surface Science* **2002**, *189*, 307–312.

[33] a) T. Takahashi, S. Fukatsu, K. M. Itoh, M. Uematsu, A. Fujiwara, H. Kageshima, Y. Takahashi, K. Shiraishi, *Journal of Applied Physics* **2003**, *93*, 3674–3676; b) B. J. Giletti, R. A. Yund, *J. Geophys. Res.* **1984**, *89*, 4039–4046; c) A. P. Mamontov, V. I. Balyuba, L. L. Shirokov, B. S. Azikov, *Arsenid Galliya* **1969**, *2*, 203–204.

[34] R. S. Bradley, A. K. Jamil, D. C. Munro, *Geochimica et Cosmochimica Acta* **1964**, *28*, 1669–1678.

[35] L. Švob, *Solid-State Electronics* **1967**, *10*, 991.

[36] R. K. Franks, J. B. Robertson, *Solid State Communications* **1967**, *5*, 479.

[37] G. J. Yurek, J. P. Hirth, R. A. Rapp, *Oxidation of Metals* **1974**, *8*, 265.

[38] a) S. Hallenbeck, J. Nuth, *Astrophysics and Space Science* **1997**, *255*, 427–433; b) S. L. Hallenbeck, J. A. Nuth III, R. N. Nelson, *The Astrophysical Journal* **2000**, *535*, 247–255; c) F. J. M. Rietmeijer, J. A. Nuth, I. D. R. Mackinnon, *Icarus* **1986**, *66*, 211–222.

[39] a) G. E. Walrafen, P. N. Krishnan, *The Journal of Chemical Physics* **1981**, *74*, 5328; b) Powder Diffraction File, Card No. 01-070-2516 for quartz (International Center on Diffraction Data, Newtown Square, PA); c) Powder Diffraction File, Card No. 01-071-3839 for cristobalite (International Center on Diffraction Data, Newtown Square, PA); d) C. D. Sandgren, *Growth And Reproductive Strategies of Freshwater Phytoplankton*; Cambridge University Press, 1988.

[40] Guruswamy, S.; Park, S. M.; Hirth, J. P.; Rapp, R. A. *Oxidation of Metals* **1986**, *26*, 77.

[41] Chaudhari, P. *Journal of Vacuum Science and Technology* **1972**, *9*, 520-522.

[42] Thompson, C. V.; Carel, R. *Journal of the Mechanics and Physics of Solids* **1996**, *57*, 657-673.

[43] R. Koch, *Journal of Physics: Condensed Matter* **1994**, *6*, 9519.

[44] a) S.-J. Hwangm W. D. Nix, Y.-C. Joo, *Acta Materialia* **2007**, *55*, 5297; b) F. Y. Génin, *Acta Metallurgica et Materialia* **1995**, *43*, 4289; c) P. Chaudhari, *Journal of Applied Physics* **1974**, *45*, 4339; d) W. B. Pennebaker, *Journal of Applied Physics* **1969**, *40*, 394; e) H. Galinski, T. Ryll, L. Schlagenhauf, L. J. Gauckler, P. Stender, G. Schmitz, *Phys. Rev. B* **2012**, *85*, 125408.

[45] C. Y. Chang, R. W. Vook, *Journal of Materials Research* **1989**, *4*, 1172.

[46] a) M. J. Cordill, D. F. Bahr, N. R. Moody, W. W. Gerberich, *Materials Science and Engineering: A* **2007**, *443*, 150; b) N. Sridhar, D. J. Srolovitz, B. N. Cox, *Acta Materialia* **2002**, *50*, 2547; c) K. M. Crosby, R. M. Bradley, *Phys. Rev. E* **1999**, *59*, R2542.

[47] a) I. Van der Molen, *Tectonophysics* **1981**, *73*, 323; b) G. Simmonsm H. W. Cooper, *International Journal of Rock Mechanics and Mining Sciences & Geomechanics Abstracts* **1978**, *15*, 145.

[48] a) G. Bayer *Proceedings of the British Ceramic Society*, 1973, *22*, 39-53; b) Lyon, K.; Salinger, G.; Swenson, C.; White, G. *Journal of Applied Physics* **1977**, *48*, 865-868.

[49] Kikuchi, Y.; Sudo, H.; Kuzuu, N. *Journal of Applied Physics* **1997**, *82*, 4121-4123.

[50] Touloukian, Y. S. *Thermophysical Properties of Matter: [the TPRC Data Series; a Comprehensive Compilation of Data*, New York: IFI/Plenum, **1970**, *13.*

[51] C.-H. Ma, J.-H. Huang, H. Chen, *Thin Solid Films* **2002**, *418*, 73.

[52] a) Lang, S. *Properties of High-Temperature Ceramics and Cermets, Elasticity and Density at Room Temperature*, Monograph 6 **1960**; b) Oh, C.; Lee, H.; Ko, S.; Kim, S.; Ahn, H. *Sensors and Actuators A* **2005**, *117*, 151-158; c) Maier-Schneider, D.; Maibach, J.; Obermeier, E.; Schneider, D. *Journal of Micromechanics and Microengineering* **1995**, 5, 121-124; d) F. Guyot, B. Reynard, *Chemical Geology* **1992**, *96*, 411.

[53] Ohring, M. *Materials Science of Thin Films* **2002**, 732.

[54] M. Kuntz, B. Meier, G. Grathwohl, *Journal of the American Ceramic Society* **1993**, *76*, 2607.

[55] a) J. Crampon, *Acta Metallurgica* **1980**, *28*, 123; b) J. H. Henslerm G. V. Cullen, *Journal of the American Ceramic Society* **1968**, *51*, 557–559; c) J. Cramponm B. Escaig, *Journal of Materials Science* **1978**, *13*, 2619; d) J. Cramponm B. Escaig, *Journal of the American Ceramic Society* **1980**, *63*, 680–686.

[56] a) Z. Bao, Conversion of 3-D nanostructured biosilica templates into non-oxide replicas **2008**; b) Z. Bao, M.-K. Song, S. C. Davis, Y. Cai, M. Liu, K. H. Sandhage, *Energy & Environmental Science* **2011**, *4*, 3980 –Reproduced by permission of The Royal Society of Chemistry (*Figures 4.4, 4.5, 4.6, 4.7, and Table 4.1, 4.2). Original work may be found at:
http://pubs.rsc.org/en/Content/ArticleLanding/2011/EE/c1ee02102h.

[57] a) B. F. Machado, H. T. Gomes, P. Serp, P. Kalck, J. L. Figueiredo, J. L. Faria, *Catalysis Today* **2010**, *149*, 358; b) M. Quirós, A. B. García, M. A. Montes-Morán, *Carbon* **2011**, *49*, 406; c) S. Bischoff, H.-E. Maneck,H. Preiss, K. Fujimoto, *Applied Catalysis* **1991**, *75*, 45; d) P. W. Albers, J. Pietsch, J. Krauter, S. F. Parker, *Physical Chemistry Chemical Physics* **2003**, *5*, 1941; e) Y. Shao, S. Zhang, R. Kou, X. Wang, C. Wang, S. Dai, V. Viswanathan, J. Liu, Y. Wang, Y. Lin, *Journal of Power Sources* **2010**, *195*, 1805; f) R. T. Mayes, P. F. Fulvio, Z. Ma, S. Dai, *Physical Chemistry Chemical Physics* **2011**, *13*, 2492; g) R. Arrigo, M. Hävecker, S. Wrabetz, R. Blume, M. Lerch, J. McGregor, E. P. J. Parrott, J. A. Zeitler, L. F. Gladden, A. Knop-Gericke, R. Schlögl, D. S. Su, *J. Am. Chem. Soc.* **2010**, *132*, 9616.

[58] a) K. Nakanishi, N. Tanaka, *Acc. Chem. Res.* **2007**, *40*, 863; b) Z. L. Hua, J. Zhou, J. L. Shi, *Chemical Communications* **2011**, *47*, 10536; c) A. H. Dessources, S. Hartmann, M. Baba, N. Huesing, J. M. Nedelec, *Journal of Materials Chemistry* **2012**, *22*, 2713; d) A. Sachse, A. Galarneau, F. Fajula, F. Di Renzo, P. Creux, B. Coq, *Microporous and Mesoporous Materials* **2011**, *140*, 58.

[59] a) Y. Shao, J. Liu, Y. Wang, Y. Lin, *J. Mater. Chem.* **2008**, *19*, 46–59; b) H. A. Gasteiger, S. S. Kocha, B. Sompalli, F. T. Wagner, *Applied Catalysis B: Environmental* **2005**, *56*, 9–35.

[60] a) B. Fıçıcılar, A. Bayrakçeken, İ. Eroğlu, *International Journal of Hydrogen Energy* **2010**, *35*, 9924–9933; b) S.-H. Choi, D.-W. Jung, S.-O. Yoon, S. Park, E.-S. Oh, J. Kim, *Metals and Materials International* **2011**, *17*, 811–816; c) H.-Y. Du, C.-H. Wang, H.-C. Hsu, S.-T. Chang, S.-C. Yen, L.-C. Chen, B. Viswanathan, K.-H. Chen, *Journal of Materials Chemistry* **2011**, *21*, 2512; d) H. Tang, S. P. Jiang, *J. Phys. Chem. C* **2008**, *112*, 19748–19755; e) E. P. Ambrosio, C. Francia, M. Manzoli, N. Penazzi, P. Spinelli, *International Journal of Hydrogen Energy* **2008**, *33*, 3142–3145; f) N. Job, F. Maillard, M. Chatenet, C. J. Gommes, S. Lambert, S. Hermans, J. R. Regalbuto, J.-P. Pirard, in *Scientific Bases for the Preparation of Heterogeneous Catalysts Proceedings of the 10th International Symposium, Louvain-la-Neuve, Belgium, July 11-15, 2010*, Elsevier, **2010**, pp. 169–176.

[61] a) P. N. Bartlett, R. G. Whitaker, *Journal of Electroanalytical Chemistry and Interfacial Electrochemistry* **1987**, *224*, 37; b) H. J. Bright, M. Appleby, *Journal of Biological Chemistry* **1969**, 244, 3625; c) M. K. Weibel, H. J. Bright, *Journal of Biological Chemistry* **1971**, 246, 2734.

[62] a) A. Ganesh Kumar, S. Swarnalatha, P. Kamatchi, R. Kirubagaran, K. Perinmbam, G. Sekaran, *Journal of Porous Materials* **2009**, *16*, 439–445; b) M. Quirós, A. B. García, M. A. Montes-Morán, *Carbon* **2011**, *49*, 406–415; c) J. A. Osborn, R. M. Ianniello, H. J. Wieck, T. F. Decker, S. L. Gordan, A. M. Yacynych, *Biotechnology and Bioengineering* **1982**, *24*, 1653–1669; d) A. B. Jarzębski, K. Szymańska, J. Bryjak, J. Mrowiec-Białoń, *Catalysis Today* **2007**, *124*, 2; e) C. Ispas, I. Sokolov, S. Andreescu, *Analytical and Bioanalytical Chemistry* **2009**, *393*, 543.

[63] a) Y. Yu, J. Addai-Mensah, D. Losic, *Langmuir* **2010**, *26*, 14068–14072; b) E. K. Payne, N. L. Rosi, C. Xue, C. A. Mirkin, *Angewandte Chemie International Edition* **2005**, *44*, 5064–5067; c) Y. Fang, V. W. Chen, Y. Cai, J. D. Berrigan, S. R. Marder, J. W. Perry, K. H. Sandhage, *Advanced Functional Materials* **2012**, *22*, 2550–2559.

[64] Z. Bao, E. M. Ernst, S. Yoo, K. H. Sandhage, *Advanced Materials* **2009**, *21*, 474–478.

[65] S. I. Woo, D. K. Kim, Y. K. Park, M. R. Kim, P. Decyk, *Catalysis Letters* **2003**, *85*, 69–72.

[66] T. J. Schmidt, H. A. Gasteiger, G. D. Stäb, P. M. Urban, D. M. Kolb, R. J. Behm, *J. Electrochem. Soc.* **1998**, *145*, 2354.

[67] G. W. Wang, Y. Fang, P. Kim, A. Hayek, M. R. Weatherspoon, J. W. Perry, K. H. Sandhage, S. R. Marder, S. C. Jones, *Adv. Funct. Mater.* **2009**, *19*, 2768.

[68] W. M. Haynes, *CRC Handbook of Chemistry and Physics (92 ed.)*, CRC Press, **2011**, 5-94-5-98.

[69] C. M. Wong, K. H. Wong, X. D. Chen, *Appl. Microbiol. Biotechnol.* **2008**, *78*, 927.

[70] N. R. Haase, S. Shian, K. H. Sandhage, N. Kröger, *Advanced Functional Materials* **2011**, *21*, 4243–4251.

[71] V. P. Menon, C. R. Martin, *Anal. Chem.* **1995**, *67*, 1920.

[72] a) Y. Sun, B. T. Mayers, Y. Xia, *Nano Lett.* **2002**, *5*, 481; b) Y. Sun, Y. Xia, *Science* **2002**, *298*, 2176.

[73] a) A. Ulman, *Chem. Rev*. **1996**, *96*, 1533; b) W. Shi, Y. Sahoo, M. T. Swihart, *Colloids Surfaces A*, **2004**, *246*, 109; c) J. C. Love, L. A. Estroff, J. K. Kriebel, R. G. Nuzzo, G. M. Whitesides, *Chem. Rev.* **2005**, *105*, 1103; d) S.-F. Liu, X-H. Li, Y-C. Li, Y-F. Li, J-R. Li, L. Jiang, *Electrochim. Acta* **2005**, *51*, 427; e) H. Hakkinen, *Nature Chem.* **2012**, *4*, 334.

[74] M. von Smoluchowski, *Bull. Int. Acad. Sci. Cracovie* **1903**, *1*, 184.

[75] a) Powder Diffraction File, Card No. 89-2955 for Si; b) Power Diffraction File, Card No. 73-1708 for β-SiC; c) Powder Diffraction File, Card No. 75-0444 for C (International Center on Diffraction Data, Newtown Square, PA).

[76] F. Barbir and S. Yazici, *Int. J. Energy Res.*, **2008**, *32*, 369

[77] a) P. B. Lukins, D. R. McKenzie, A. M. Vassallo, J. V. Hanna, *Carbon* **1993**, *31*, 569; b) J. R. Dyer, *Applications of Absorption Spectroscopy of Organic Compounds*, Chapter 3, Prentice-Hall of India Private Limited, New Delhi, **1984**.

[78] G. V. Franks, *Journal of Colloid and Interface Science* **2002**, *249*, 44.

[79] a) V. Somerset, P. Baker, E. Iwuoha, *Journal of Environmental Science and Health, Part B* **2009**, *44*, 164–178; b) M. Gamero, M. Sosna, F. Pariente, E. Lorenzo, P. N. Bartlett, C. Alonso, *Talanta* **2012**, *94*, 328–334; c) G. F. Paciotti, L. Myer, D. Weinreich, D. Goia, N. Pavel, R. E. McLaughlin, L. Tamarkin, *Drug Delivery* **2004**, *11*, 169–183; d) J. Kim, H. Jia, P. Wang, *Biotechnology Advances* **2006**, *24*, 296–308.

[80] a) Powder Diffraction File, Card No. 01-071-4615 for Au; b) Powder Diffraction File, Card No. 01-071-4612 for Ag (International Center on Diffraction Data, Newtown Square, PA).

[81] a) M. Lomello-Tafin, A. A. Chaou, F. Morfin, V. Caps, J.-L. Rousset, *Chemical Communications* **2005**, 388; b) K. Yu, Z. Wu, Q. Zhao, B. Li, Y. Xie, *J. Phys. Chem. C* **2008**, *112*, 2244–2247; c) P. Mohapatra, J. Moma, K. M. Parida, W. A. Jordaan, M. S. Scurrell, *Chemical Communications* **2007**, 1044; d) Q. H. Zeng, K. Wong, A. B. Yu, *Advanced Materials Research* **2011**, *418-420*, 870–875.

[82] a) E. D. Palik, Handbook of Optical Constants of Solids, Elsevier, 1998, *946*; b) E. D. Palik, Handbook of Optical Constants of Solids, Elsevier, 1998, *564*; c) E. D. Palik, Handbook of Optical Constants of Solids, Elsevier, 1998, *800*; d) Y. Li, F. Piret, T. Léonard, B.-L. Su, *Journal of Colloid and Interface Science* **2010**, *348*, 43–48; e) M. M. Hasan, A. S. M. A. Haseeb, R. Saidur, H. H. Masjuki, *International Journal of Chemical & Biomolecular Engineering* **2008**, *1*, 93–97.

[83] a) R. C. Schroden, M. Al-Daous, C. F. Blanford, A. Stein, *Chem. Mater.* **2002**, *14*, 3305–3315; b) W. Dong, H. J. Bongard, F. Marlow, *Chem. Mater.* **2003**, *15*, 568–574; c) K. Ren, Z.-Y. Li, X. Ren, S. Feng, B. Cheng, D. Zhang, *Phys. Rev. B* **2007**, *75*, 115108; d) S.-H. A. Lee, N. M. Abrams, P. G. Hoertz, G. D. Barber, L. I. Halaoui, T. E. Mallouk, *J. Phys. Chem. B* **2008**, *112*, 14415–14421; e) C. I. Aguirre, E. Reguera, A. Stein, *Advanced Functional Materials* **2010**, *20*, 2565–2578.

[84] K. M. Ho, C. T. Chan, C. M. Soukoulis, *Phys. Rev. Lett.* **1990**, *65*, 3152–3155.

[85] a) M. Deubel, G. von Freymann, M. Wegener, S. Pereira, K. Busch, C. M. Soukoulis, *Nature Materials* **2004**, *3*, 444–447; b) M. Jensen, M. Brett, *Opt. Express* **2005**, *13*, 3348–3354; c) S. Noda, M. Fujita, T. Asano, *Nature Photonics* **2007**, *1*, 449–458; d) N. Vats, T. Rudolph, *Journal of Modern Optics* **2001**, *48*, 1495–1502; e) R. W. J. Scott, S. M. Yang, G. Chabanis, N. Coombs, D. E. Williams, G. A. Ozin, *Advanced Materials* **2001**, *13*, 1468–1472; f) Y.-J. Lee, S. A. Pruzinsky, P. V. Braun, *Langmuir* **2004**, *20*, 3096–3106.

[86] J. W. Galusha, C.-K. Tsung, G. D. Stucky, M. H. Bartl, *Chem. Mater.* **2008**, *20*, 4925–4930.

[87] a) L. Brus, *Current Opinion in Colloid & Interface Science* **1996**, *1*, 197–201; b) K. Busch, S. John, *Phys. Rev. E* **1998**, *58*, 3896–3908.

[88] a) V. M. N. Passaro, F. Dell'Olio, F. De Leonardis, *Sensors* **2007**, *7*, 2741–2749; b) V. M. N. Passaro, F. Dell'Olio, B. Casamassima, F. De Leonardis, *Sensors* **2007**, *7*, 508–536.

[89] B. Hatton, L. Mishchenko, S. Davis, K. H. Sandhage, J. Aizenberg, *Proceedings of the National Academy of Sciences* **2010**, *107*, 10354 –10359.

[90] a) F. Sordello, V. Maurino, C. Minero, *Journal of Materials Chemistry* **2011**, *21*, 19144; b) J. S. King, E. Graugnard, C. J. Summers, *Advanced Materials* **2005**, *17*, 1010–1013; c) J. I. L. Chen, G. von Freymann, S. Y. Choi, V. Kitaev, G. A. Ozin, SPIE, **2007**, p. 66500W–66500W–7; d) J. E. G. J. Wijnhoven, W. L. Vos, *Science* **1998**, *281*, 802–804.

[91] a) R. R. Unocic, F. M. Zalar, P. M. Sarosi, Y. Cai, K. H. Sandhage, *Chem. Commun.* **2004**, 796; b) S.-J. Lee, C.-H. Huang, S. Shian, K. H. Sandhage, *Journal of the American Ceramic Society* **2007**, *90*, 1632–1636.

[92] a) J. Li, T. Zheng, *Sensors and Actuators B: Chemical* **2008**, *131*, 190–195; b) C.-Y. Kuo, S.-Y. Lu, S. Chen, M. Bernards, S. Jiang, *Sensors and Actuators B: Chemical* **2007**, *124*, 452–458; c) C. Liu, G. Gao, Y. Zhang, L. Wang, J. Wang, Y. Song, *Macromolecular Rapid Communications* **2012**, *33*, 380–385; d) C. F. Blanford, R. C. Schroden, M. Al-Daous, A. Stein, *Advanced Materials* **2001**, *13*, 26.

[93] S. H. Park, Y. Xia, *Langmuir* **1999**, *15*, 266–273.

[94] H. Föll, M. Christophersen, J. Carstensen, G. Hasse, *Materials Science and Engineering: R: Reports* **2002**, *39*, 93–141.

[95] P. Fouilloux, *Applied Catalysis* **1983**, *8*, 1.

[96] V. Prostakova, J. Chen, E. Jak, S. A. Decterov, *Calphad* **2012**, *37*, 1.